ASSEMBLY OF NATURAL PHOTOSYNTHETIC COMPONENTS ON GRAPHENE OXIDE AND GOLD SURFACES FOR LIGHT ENERGY TRANSDUCTION

By

JOHN W. HARROLD, JR.

A Dissertation submitted to the

Graduate School-New Brunswick

Rutgers, The State University of New Jersey

in partial fulfillment of the requirements

for the degree of

Doctor of Philosophy

Graduate Program in Chemistry and Chemical Biology

written under the direction of

Paul G. Falkowski

and Michele Vittadello (External Co-Advisor)

and approved by

_____

_____

_____

_____

_____

New Brunswick, New Jersey

October 2014

ABSTRACT OF THE DISSERTATION

Assembly of Natural Photosynthetic Components on Graphene Oxide and Gold Surfaces for Light Energy Transduction

By JOHN W. HARROLD, JR.

Dissertation Director:

Paul Falkowski

Photosynthetic reaction centers are integral membrane proteins of particular interest for their remarkable ability to catalyze photo-induced charge separation with high quantum efficiency. For this reason they have been targeted for integration in biohybrid systems for capture and conversion of solar energy. In this study isolated photosynthetic core complexes from phototrophic organisms are interfaced with conductive materials for the development of photoelectrochemical systems. Photosystem II core complexes (PSII CCs) bearing poly histidine tags isolated from genetically modified *Thermosynechococcus elongatus*, were tethered to a graphene oxide (GO) support through immobilized metal coordination sites. The PSII CCs tethered to GO-coated gold electrodes and GO nanosheets in suspension showed 59% retention of quantum yield of photochemistry. Fluorescence kinetic relaxation analyses indicates that a direct electron transfer occurs between embedded quinone (Q_A) of PSII and GO. Flash oxygen evolution activity shows a threefold improvement in comparison with isolate PSII in suspension. Photosystem I core complexes (PSI CCs) isolated from *Synnehcoccous* PCC 7002 were also

immobilized on GO. The co-immobilization of PSII and PSI on GO resulted in a biohybrid electron transport chain based on the photosynthetic Z-scheme. As a robust alternative to PSII, a very labile enzyme, chromatophores isolated from the bacterium *Rhodospirillum rubrum* were adsorbed on gold electrodes. These intracytoplasmic membrane vesicles containing bacterial type II reaction centers yielded a maximum photo-driven current of 1.5 $\mu A/cm^2$ that slowly declined in a week. This study demonstrates the utility of bottom-up reconstruction of biological nanostructure as a platform for fundamental experimental approaches and the pursuit of new paradigms toward renewable energy resources.

Acknowledgments

First, I would like to thank my advisor **Paul Falkowski**. After spending two years working on a completely different topic, I was looking for a new lab group to join as my old one had left the University. At that same time, in a class I was taking that discussed energy concerns, I saw Paul give a talk. I admired the passion, confidence, and, most importantly, the expertise that he expressed in that talk. I will never forget how Paul welcomed me into the group; he said to me: "You are done screwing around, now it is time to get working." These words set the course for the next few years of my life. Energy has been a concern of mine for my entire academic life thus far, and I was excited to be finally doing something about it.

Then, a few weeks later, Paul introduced me to **Michele Vittadello** of Medgar Evers College the City University of New York. Michele had this crazy idea – those are the best kind. After that first meeting, in which we discussed artificial photosynthesis, I was off and there was no looking back. Having Michele as my Co-Advisor was a great experience. I know I wasn't always the easiest to deal with, but the same idealism that first gave us the inspiration to wok together has been a constant companion in our lab group. I am lucky to have had such an ambitious and creative scientist to look up to.

Later, I had the opportunity to work on this really interesting project with **Robert Niederman** of Rutgers**.** While I initially thought that I was being given lab space to use, what in reality happened was that I found another mentor to work with. The next few years consisted of having these three very different scientists mentor me in such an amazing way. Bob introduced us to **Kamil Woronowicz** of Rutgers, and he shortly after joined our group, fueled by as much idealism as the rest of us. **Dominic Hull** of Medgar Evers College CUNY joined our group and really rounded out the discussions.

In Michele's distinct style, I was encouraged to seek out the best and the brightest people to work with. I am grateful for the opportunity to have worked with and learn from some amazing scientists. **Charles Dismukes** and **Gennady Ananyev** of Rutgers have been a resource and provided a challenge to push farther. **Bill Rutherford** of the Imperial College of London not only helped get the project underway, but also gave a high standard for which to work towards. **John Golbeck** and **Cara Lubner** of Penn State were welcoming colleagues. **Donald Hirsh** from the College of New Jersey shared his expertise and enthusiasm. **Max Gorbunov** of Rutgers lent me his expertise and support. **Eric Garfunkel** and **Martha Cotter** of Rutgers served on my committee and provided a constant resource.

I am grateful for the support and inspiration from many of my mentors in the past. **Tim Blanc, Gary Olson, and David Talaga** gave me new perspectives on research. **Mike Kost, Paul Schueler, Darryl Walke, Peter Kahn,** and **John Brennan** all have taught me so much about science and started me on this path. **Edward Castner** went beyond traditional academic and scientific support to truly be there for me. I am grateful to the **The Helyar House Foundation** for making my undergraduate education a reality.

I have had the opportunity to mentor several undergraduates and post baccalaureate students in the labs; so many of them have been a large part of my graduate career. **Katie Battles, Mike Kopka, Joeseph Kay,** and **Joana Lamptey** have been among the best and the brightest students that continued to deal with my unreasonable demands. Lastly, I want to thank **Joomi Kim, Ben Jelen, John Kim, Jeana Drake, Ananya Agarwal, Fedor Kouzminov, Marianna Venuleo, Heather Lee, Frank Natale,** and **Kenia Castellanos** for their continued support during graduate school.

Dedication

I would like to dedicate this to my parents **John W. Harrold, Sr. and Donna Harrold** for instilling in me the curiosity that has brought me here.

And to my wife **Kathryn Harrold** for the constant support and encouragement that has kept me here.

Table of Contents

Table of Figures

Table of Tables

Chapter I: Introduction

1. Solar Energy

The sun is a promising renewable energy resource. Estimates indicate that 4.3 x 10^{20} J of energy from sunlight strikes the earth each hour. If this energy could be harvested is would satisfy the global energy consumption per year.[1] To date an efficient and cost-effective solar energy conversion and storage solution has yet to be identified. Biomass, solar photovoltaic, and artificial photosynthesis (just to name a few) rely on the sun as primary energy source. Photosynthesis is a natural process capable of converting light energy into chemical energy by means of light-dependent reactions and so-called "dark reactions". [2] In particular, this thesis is focused on learning from natural photosynthesis by the step-wise self-assembly towards semi-artificial nanoscale systems.

> *"All human life is dependent, directly or indirectly, on photosynthesis. Its direct effects provide the source of all our food, either as plant material or as the plants that feed the animals, birds, and fish we eat. The plants that harness solar energy are also the source of the oxygen we breathe and an essential component of the water cycle. At a more abstract level, the plants around us also contribute to our cultural identity, as well as being a source of spiritual sustenance to many people." – Ian Lowe* [3]

Different kinds of biomass resources are grown to harvest their lipid-rich components. For instance, seeds like rapeseed, fibrous plant material such as that of switch grass, or unicellular organisms such as algae have been genetically modified for maximizing the lipid yield. The optimum choice of biomass culture depends on the climate conditions that are present, especially in terms of irrigation requirements. The growth of these plants is dependent on seasonal changes and local environment. The ideal plant must be genetically transformable and have growth characteristics that

would allow it to thrive with minimal energy input and low nutrient requirements. Woody, grassy, and herbaceous plants have been the target of more recent attention. [4, 5] The downside to this choice is the risk of disrupting effects on the human food supply chain. There is also an added risk to natural areas due to agricultural pollutants, and practices that may result in a net positive carbon emission into the atmosphere. While biomass solutions definitely show promise, some of these pressing concerns must be dealt with. Photovoltaic solutions have a prominent role in usage of solar energy. A common type is known as a dye sensitized solar cell (DSSC). These devices generally consist of a mesoporous layer of a semiconducting material, such as TiO_2, on a conducting surface. The semiconducting material is coated with a dye. These dyes are excited by the incident light and inject electrons into the conducting bands of the semiconducting material. This chemical architecture makes the system more efficient and capable of responding to a wider range of incident light. [6]

2. Water Splitting

Solar energy can be stored in the form of chemical bonds by means of catalytic structures resembling natural photosynthesis. Artificial photosynthesis is a broad area of research encompassing different approaches in which solar energy is trapped by inorganic or biohybrid components similar to those found in natural photosynthetic processes. The long-term goal of artificial photosynthesis research is to re-engineer the machinery of the natural photosynthetic apparatus in a way that is amenable to easier interfacial control and recovery of the active components.[3] In understanding the natural system more stable and efficent compnents can be subsituted for the natural ones. In this project we focus on systems that include parts of the biological photosynthetic process in conjunction with electroactive supports. These types of architectures can be referred to as a biohybrid or semi-artificial photosynthetic systems.

The enthalpy and Gibbs free energy values required to split one molecule of water ($H_20 \rightarrow H_2 + ½ O_2 + 2e^-$) are ΔH°= 285.9kJ/mol and a ΔG° = 237.3 kJ/mol. The electromotive force with respect to the standard hydrogen electrode is:

$$\Delta E^\circ = -\Delta G^\circ/2F = -1.23\ V \quad \text{(Eq. 1.1)}$$

Where F is the Faraday constant of 96,485 C/mol. That corresponds to a ΔE° = -1.23 V per pair of electrons transferred. [7 8]

The actual electromotive force for this reaction to occur electrochemically is about 1.50 V in a typical electrochemical set-up due to chemical overpotentials, or the additional voltage needed past the thermodynamic requirement in order to make the reaction happen. [9] The photocatalytic components of the photosynthetic apparatus minimize these solution resistances in the conversion of light to a chemical bond.[8] This energy is readily available by the sun for all wavelengths under about 1000 nm. However the photosynthetic apparatus is capable of absorbing efficiently wavelengths below 700 nm. The energy needs to be higher than the energy corresponding to the characteristic wavelength of the photosynthetic trap. [10]

$$E = hc/\lambda \quad \text{(Eq. 1.2)}$$

where λ = wavelength (nm), c = the speed of light (2.998 x10^8 $^m/_s$), E = energy in electron Volts (eV), and h = Plank's constant (6.626×10^{-34} m^2kg/s). . Learning from nature's benchmark apparatus suggests the possibility of assembling photosynthetic enzymes and redirecting them to the chemical synthesis of chosen target molecules. [11] This strategy would allow the control of electron transfer necessary for generating high reducing equivalents for driving dowstream chemical processes. The chemical energy of water can in principle be stored as the simplest chemical bond H-H. Molecular

hydrogen can then be stored and used as fuel when needed. Molecular hydrogen can be used directly, or in the presence of a catalyst to reduce CO_2 to methanol or methane. [12]

3. Photosynthesis

In this project, isolated natural photosynthetic components are included in biohybrid systems. Two types of photosynthetic molecules are considered for assembly onto electron transporting materials: oxygenic (generating oxygen as a byproduct) and anoxygenic (not generating oxygen a byproduct) reaction centers.

The oxygenic photosynthetic apparatus in green plants and cyanobacteria is based on two types of reaction centers called Photosystem I (PSI) and Photosystem II (PSII), embedded in the thylakoid membrane. These biomolecules can efficiently convert light into electrical potentials under a wide range of light and temperature conditions.[13] The quantum efficiencies of PSI and PSII are 45 ± 10% and 80 ± 15%, respectively.[14] Photoelectron generation is associated with the oxidation of water to oxygen and protons catalyzed by PSII. Electrons generated from water oxidation on the luminal side of the membrane are then transferred to the stromal side for the formation of reducing equivalents.[15, 16] The overall reaction can be re-engineered for converting light into chemical energy as O_2 and H_2 in a cell-free environment.

The architecture of a PSII CC from the thermophylic cyanobacterium, *T. elongatus,* has been determined by high-resolution X-ray crystallography.[14, 15] *In vitro,* the PSII CC exists in a dimeric form with physical dimensions of 20.5 nm (L) x 11.0 nm (W) x 10.5 nm (D). Each PSII CC monomer is characterized by 20 protein subunits, 35 Chlorophyll *a* (Chl a) molecules and 12 carotenoids molecules, 25 integral lipids, and 1 Cl^- ion. In each monomer the RC subunits D_1 and D_2, hosting all the cofactors necessary for electron transport, are protected by the CP_{43} and CP_{47} subunits binding Chl a of the core antenna. Upon illumination, the excited primary electron donor, P_{680}, ejects an electron that arrives on

the final electron acceptor, plastoquinone Q_B, through chlorophyll D_1 (Chl_{D1}), pheophytin D_1 ($Pheo_{D1}$) and plastoquinone (Q_A). While Q_A is fixed within the structure[17, 18] Q_B *in vivo* is released into the membrane matrix after accepting two electrons and undergoing protonation. Recent evidence for the existence of a third embedded quinone Q_C has been reported. [15] The cationic radical $P_{680}^{+\cdot}$ is reduced by a neutral tyrosine forming $Tyr_Z\bullet$[19, 20], which in turn oxidizes Mn and results in the withdraw of 4 electrons from a pair of H_2O molecules. [21, 22] The PSII CC dimers can be separated into monomers while preserving activity. [22, 23] The possibility of using isolated PSII CCs in photoelectrochemical devices is hindered by the instability of the D_1 protein that, *in vivo,* is replaced every half an hour. However, the catalytic efficiency of the Mn_4Ca water-oxidizing complex (WOC) represents the benchmark against which all potential inorganic catalysts for water oxidation are measured[24]

The trimeric structure of the PSI CC from *Synechococcus elongatus* has also been resolved at atomic detail by X-ray crystallography. [25] The cylindrical trimer has a diameter of about 22 nm and a height of 10 nm. Each monomer is characterized by 12 proteins and 127 cofactors including 96 Chl a, 2 phylloquinones, 3 Fe_4S_4 clusters, 22 carotenoids, 4 lipids and putative Ca^{2+} ion. The structure of PSI in cyanobacteria is essentially conserved across different species. [23, 26, 27]

Figure 1.1 – The Structure of PSII

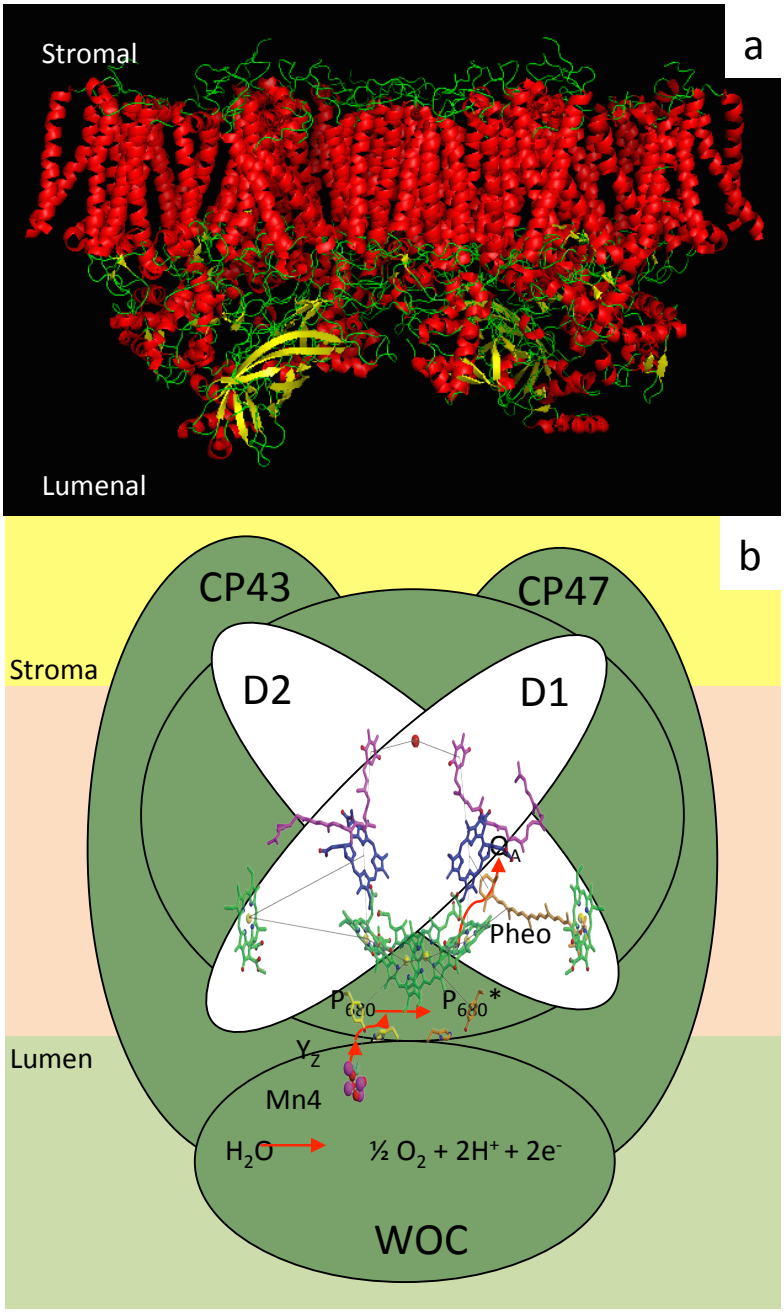

Figure 1.1: a) Crystal structure of PSII [1] complex found in its dimeric form. b) The drawing shows PSII with emphasis on the D_1 and D_2 subunits. The water oxidation complex is on the luminal side, whereas the Q_B pocket is on the stromal side.

Figure 1.2

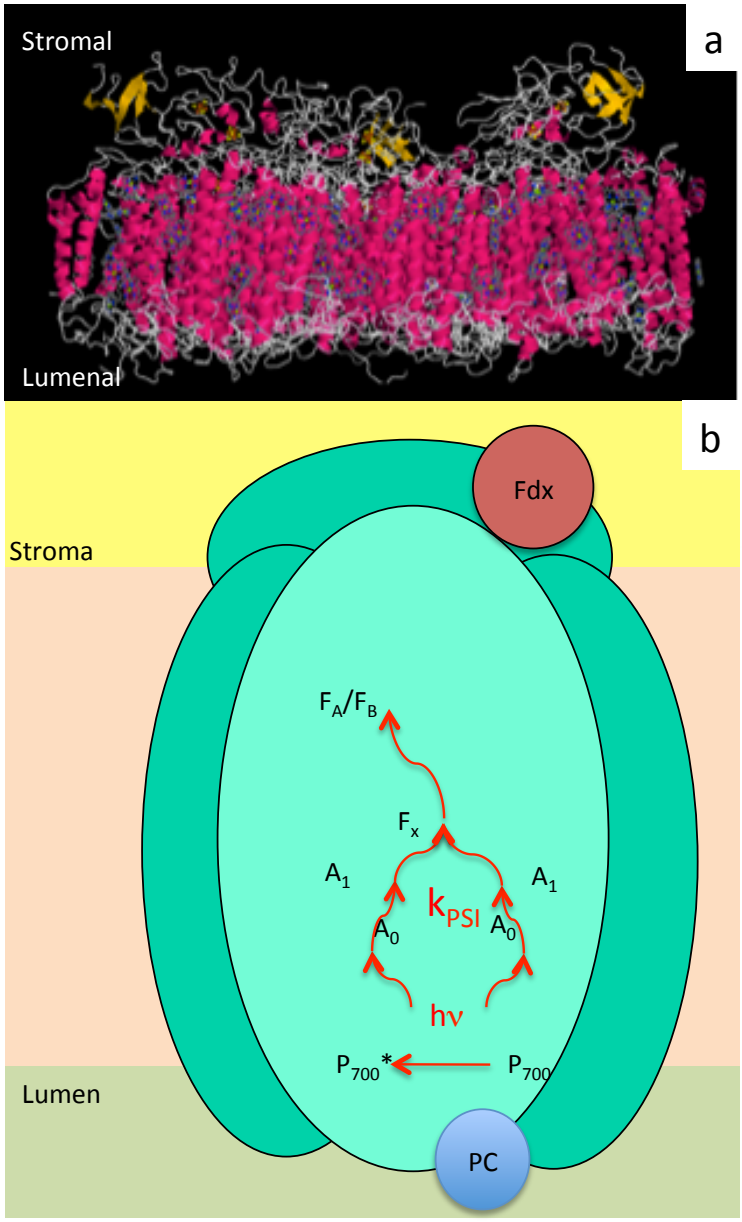

Figure 1.2 | The crystal structure of PSI in its trimetric form found in cyanobacteria. [12] Higher plants have PSI present in the monomeric form. b) The graphical representation of PSI. The plastocyanin (PC) is the redox mediator found in the luminal region of higher phototrophs. The ferredoxin (Fdx) is found on the stromal side of the membrane and will participate in the conversion of $NADP^+$ to NADPH.

Primary charge separation is initiated by the chlorophyll dimer P_{700}, and the electron is transferred through a chain of cofactors, Chl a ($A_{0)}$, phylloquinone (A_1), the Fe_4S_4 clusters, F_x, F_A and F_B. $P_{700}^{+\cdot}$ is reduced by cytochrome c_6 (or plastocyanin), while F_B^- transfers its electron to ferredoxin (or flavodoxin) and reduces $NADP^+$ to NADPH using Ferredoxin-NAPD reductase. Relevant to our purpose, the reductant NADPH is the biological equivalent of H_2 gas. The PSI CC trimers can be separated into monomers while preserving activity. [28] The structure of PSI CCs from *Synechococcus sp. PCC 7002* is not available, with the exception of the structure of the PsaE domain [29] (see figure 1.3). These structural and electronic characteristics, united with extraordinary resilience to cell-free conditions, have made PSI CCs a target for model devices, including solid-state nano-electronic systems[30-32] and "wet" photoelectrochemical cells.[33] Photocatalytic hydrogen production from non-covalent biohybrid PSI / Pt nanoparticle (NP) complexes has been demonstrated. [33, 34] PSI CCs have been wired to Pt NP and hydrogenase for direct hydrogen generation. [35-39] Suspensions of these bioconjugates were capable of high yield of hydrogen generation for extended periods of time.

Figure 1.3 - The Z-scheme

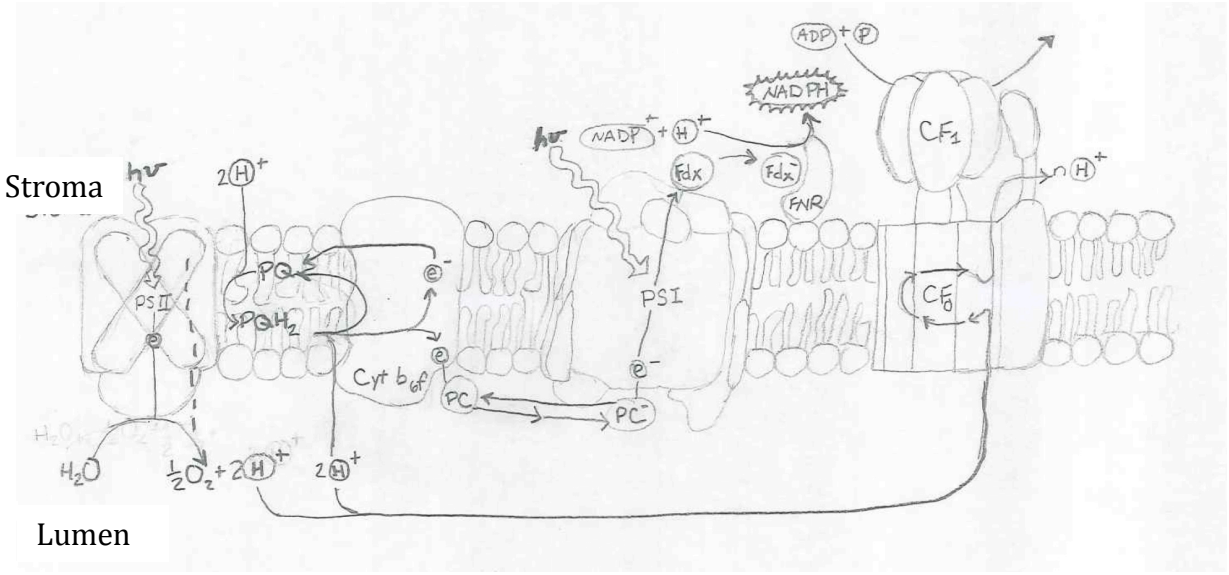

Figure 1.3 | The Z-scheme ("Z" as represented by the red dashed line) is the energy diagram for the electron transfer in this light dependent reaction. Briefly the light energy causes a primary charge separation in the P680 dimeric chlorophyll and is reduced with an electron from the water oxidation complex (WOC) of the PSII reaction center where water is oxidized into oxygen and hydrogen ions. The electron is transferred via immobile and mobile quinones to the plastiquinone pool and then to the cytochrom b_6f complex (Cyt b_6f) where the plastocyanin (PC) will be reduced by Cyt b_6f. The PSI RC will use light energy to cause a charge separation and the electron will be transferred to the ferredoxin (Fdx). The Fdx is used in the conversion of $NADP^+$ to NADPH, which provides reducing equivalent for other reactions. The proton gradient across the membrane is used by ATP synthase to convert ADP to ATP, which is used in cellular metabolism.

3. Biohybrid photosynthesis

A fundamental limitation in the assembly of biohybrid photosynthetic systems for hydrogen generation is the limited lifetime of isolated PSII CCs. The turnover number of ~1,000,000 of the D_1 protein will prove hard to bypass unless repair mechanisms can be set in place. [40-42] A robust alternative to PSII CCs is provided by chromatophores of purple non-sulfur bacteria. In particular, chromatophores from *Rsp. rubrum* afford a fully functional and robust photosynthetic apparatus ideal for biophysical investigations of electron transduction.[43] These chromatophores are vesicular organelles budding from the intracytoplasmic membrane, which include the bacterial reaction center (bRC), light harvesting complex, LH1, as well as the cytochrome bc_1 complex and ATP synthase.[44] The chromatophore works by first absorbing a photon of light. This can be absorbed directly by the reaction center or by the LH1 antenna, and the LH1 antenna is tuned to light in the near-IR. The VIS-near-IR absorbance spectrum shows that the most strongly absorbed light is centered around 875 nm as shown in figure 1.4. This light provides the energy to the RC. [45] When a photon of light is absorbed by the LH1 antenna exciton transfer will occur from the LH1 antenna to the RC. Consequently electron-hole charge separation will occur within the RC across the membrane. Proton-coupled double reduction of a quinone at the Q_B site will result in transfer of two electrons to the bc_1 complex. The bc_1 complex establishes a proton gradient across the membrane. ATP synthase driven by the proton gradient converts ADP to ATP. Each photoelectron generated across the membrane is recycled to the reaction center by cytochrome c_2.[46]

Figure 1.4 - Vis- nearIR Absorbance of Chromatophores

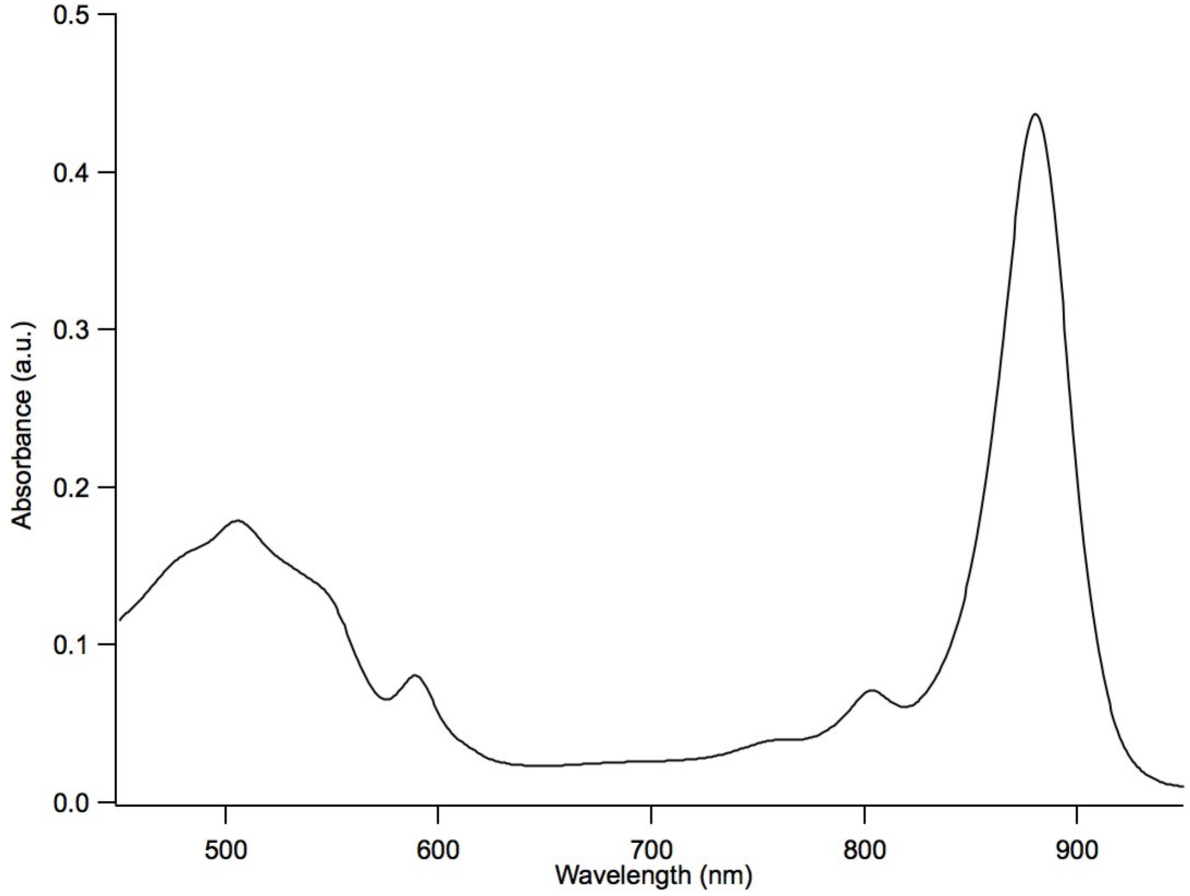

Figure 1.4 | The visible and near infrared absorbance of *Rsp. rubrum* chromatophores taken at room trmprature.

PSII CCs, PSI CCs and bRCs within chromatophores each have specific redox midpoint potentials. These biological molecules can be combined in a hybrid redox chain in conjunction with inorganic and organic photoactive materials for the direct catalytic generation of molecular hydrogen. Interest in this type of approach has recently been revived beyond a planar-junction photo-electrochemical system for hydrogen generation assembled in the past, based on coarse PSI and PSII particles.[11, 47] Recent progress

has been made toward the goal of producing components for a more heterogeneously integrated version of this system using isolated photosynthetic CCs[33, 48, 49]

In this thesis biohybrid systems are described containing biological molecules in contact with surfaces having macroscopic to nanoscale sizes. This work is configured in the context of biointerfacing, the study of controlled biomolecular interfaces. The science of biointerfacing allows biological processes normally occurring only *in vivo*, to be conducted under controlled and measureable *in vitro* conditions. This particular protein-surface interaction control is an important feature in many emerging biotechnological fields. [50] The biological molecules presented herein work better, and in some cases exclusively, in presence of water. For this reason the traditional surface measurements needed to be worked around, abandoned, or adapted to the conditions required to maintain functionality of the biosystems under investigation.

4. Graphene oxide

To fix the enzymes, a nanomaterial scaffold in suspension was used, thus breaking away from traditional electrode topologies. Such scaffold was based on GO. GO is derived from a form of elemental carbon that consists of a two-dimensional array of sp^2-hybridized carbon known as graphene.[51] This occurs when graphene is exfoliated under conditions that are strongly oxidizing. This will produce atomically thin and microscopically wide sheets of GO. The oxygen that is introduced during this process results in the formation of epoxide, ketone, alcohol, and carboxylic functional groups on the basal plane and at the edges of GO. GO has been the subject of a wide variety of studies due its electrical conductivity and optical transparency in both single layer or thin-film configurations. [52-55] GO is decorated with oxygen containing functional groups to yield a material that maintains some of the properties of graphene and allows access to known chemistry for generating new functionalities and control of electrical conductivity. [56, 57] Indeed, GO is an electron conductor at low oxygen content (8%

n_O/n_C%) and a hole conductor at high oxygen content (35%). The conductivity spans several order of magnitude from 10^3 to 10^{-9} S·cm^{-1}.[55] In this study GO is modified not only for tethering photosynthetic molecules, but also as an electroactive support.

Chapter II: Enhanced Oxygen Evolution from Photosystem II Coupled to Chemically Modified Graphene oxide

1. Introduction

This chapter describes a system in which, PSII dimers have been assembled onto single-layer GO nanosheets bearing Ni^{2+}-nitrilotriacetic acid coordination sites (GO-NiNTA), which is represented by Figure 2.1. A more detailed explanations and schematic can be found in the appendix B. The GO used in this study had an oxygen content of ~20 % (O/C molar ratio). PSII CCs His-tagged on the stromal side (on CP_{47}) were isolated by Ni affinity chromatography from the thermophylic bacterium *T. elongatus*. The functionalization of pristine GO resulted in GO-NiNTA, a material capable of coordinating His-tagged PSII CCs. Incubation with PSII CCs resulted in GO-NiNTA-PSII bioconjugates. We set out to investigate whether GO-NiNTA can provide an electron acceptor surface and is an appropriate material for self-assembly of photosynthetic proteins in a bio-hybrid electron transport chain. Electron transfer between PSII and GO are in principle thermodynamically favorable as indicated by the energy level diagram in Figure 2.2.[58]

Figure 2.1 - PSII on GO

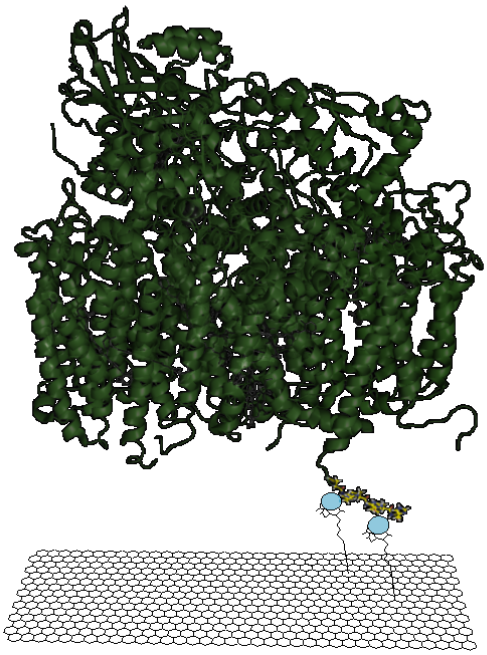

Figure 2.1 | Schematic of PSII linked to GO-NiNTA.

Figure 2.2 - Energy level diagram of PSII CC interfaced to GO.

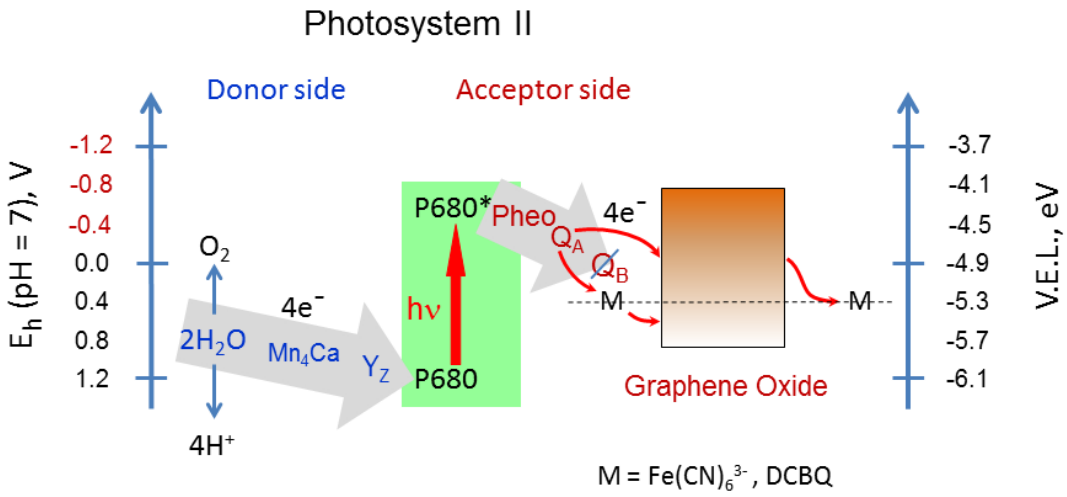

Figure 2.2 | Energy level diagram of PSII CC interfaced to GO. The main electron transfer intermediates are indicated within the schematic of PSII: P_{680} (P680), $P_{680}^{+\cdot}$ (P680*), Mn_4CaCl (Mn), tyrosine Tyr_Z, pheophytin D_1 (Pheo), fixed plastoquinone A (Q_A). The overall reaction proceeds from water oxidation to electron injection into the GO component of the GO-based resin GO-NiNTA, Direct electron transfer (indicate by an arrow) is possible from Q_A to GO. Indirect electron transfer (indicate by an arrow) is also possible via a redox mediator (M) ferricyanide [$Fe(CN)_6^{3-}$], and 2,6-dichloro-*p*-benzoquinone (DCBQ).

2. Methods

2.1 - Synthesis of GO-NiNTA resin.

A GO-based resin was synthesized by the chemical modification of GO that is discussed in more detail in the appendix. Briefly, the GO (20% oxygen-content) was modified in three steps:[11] 1) carboxylic-group activation by using N-hydroxysuccinimide (NHS) and N-ethyl-N'-(3-dimethylaminopropyl)carbodiimide; 2) Nitrilotriacetic acid binding by using N_{α},N_{α}-Bis(carboxymethyl)-L-lysine hydrate (pH=9.8); 3) nickel complexation using $NiSO_4$. Each step required one h incubation followed by centrifugation at 21,000xg, removal of the supernatant and repeated washing with deionized water.

2.2 - Directional Immobilization of PSII CCs onto GO-based resin.

PSII CCs were isolated from the thermophylic cyanobacterium *T. elongatus* mutant strain His-tagged on the C-terminus of CP_{47}. The immobilization of PSII CCs on the stromal side onto GO-NiNTA was carried out by incubation in the dark followed by repeated washing with buffer at pH 6.0. The buffer composition was 50 mM MES (pH = 6.0), 10 mM $MgCl_2$, 10 mM NaCl, 10 mM $CaCl_2$, 15% glycerol, and 0.05 % (w/v) β-dodecylmaltoside.

2.3 - Flow cytometry.

The PSII samples described above were analyzed by flow cytometry using a BD Influx Mariner 209s Flow Cytometer. The laser used for excitation was at 488 nm (200 mW) and the emission filter was at 692 ± 40 nm with a 70 µm nozzle tip. A GO-NiNTA particle suspension (solution A) was prepared by a 1-to-10 dilution of GO-Ni-NTA slurry having a GO-Ni-NTA volume fraction of 15-20% with detergent-containing buffer (Ax.2). The protein concentration of a PSII CC stock solution was determined by amino acid analysis. A PSII CC stock suspension (0.93 mg Chl a / mL or 2.56 mg of protein / mL) was diluted 1-to-10 using the same buffer mentioned above to form solution B. Then 5 µL of solution A was added to

increasing volumes from 0 to 32 µL of solution B. The above buffer was added in each case up to 450µL total volume. Each suspension was probed by flow cytometry using phosphate buffer as a sheath fluid.

2.4 - UV-Visible Spectroscopy.

The protein loading capacities of PSII CC on the GO-Ni-NTA resin was measured using a PSII CC protein following the procedures below: The protein loading capacities were obtained using a 10 µL aliquot of the GO-Ni-NTA resin. PSII CC protein loading capacities of the resins were determined indirectly by UV-Visible spectroscopy using a NanoDrop 1000 spectrophotometer at 680 nm (ϵ = 79.95). UV-Visible spectra were collected on the PSII CC protein solutions before and after treatment with the resins and after elution with imidazole. Protein samples were incubated in batch mode with each of the resins at 4°C for 1 hour on a rotisserie.

Incubation was carried out in a 40 mM MES pH 6.5 buffer supplemented with 15 mM MgCl2, 15 mM CaCl2, 20% glycerol and 1M Betaine. Protein-resin samples were spun at 4°C for 5 min at 21,000xg. The protein-loaded resins were then subjected to washing and elution steps. After each step protein samples were spun at 4°C for 5 minutes at 21,000xg. Resins were washed with 480 µL of the buffer described above prior to elution. Elution was performed on ice using 150 mM MES pH 6.5 buffer supplemented with 15 mM MgCl2, 15 mM CaCl2, 200 mM NaCl, 0.1% (w/v) Dodecyl Maltoside, 300 mM Imidazole, 10% (w/v) glycerol and 1M Betaine.

2.5 - Fluorescence Induction and Relaxation (FIRe) Measurements.

A Satlantic FIRe System[59] was used and samples were placed in a quartz cuvette. The excitation light source was a blue LED with a maximum emission at 455 nm with 60-nm bandwidth. The fluorescence emission was detected using a 680 nm filter with a 10 nm bandwidth. Each single turnover flash (STF) was set at 300 µs. The following relaxation was measured using 60 probing flashlets at 40 µs intervals. Stability measurements were conducted on samples of immobilized and free PSII (1 µg/mL of

Chl a), measured repeatedly at 120 s intervals, allowing each sample to dark adapt between measurements at 25˚C.

2.6 - Electron Paramagnetic Resonance Measurements.

PSII CC were stored in TP6 consisting of 40 mM MES, pH 6.5, 15 mM $MgCl_2$, 15 mM $CaCl_2$, 20% glycerol, and 1.0 M Betaine; more detail is available in the appendix. PSII was combined with GO-Ni-NTA and suspended in a solution of 50 mM MES, pH 6.0, 10 mM $CaCl_2$, 10 mM $MgCl_2$, 10 mM NaCl, and 15% glycerol. Final glycerol concentrations were 20 % v/v. All GO-Ni-NTA samples were made from a common stock and were made with the same volumes of addition. Samples with ascorbic acid were prepared with a final concentration of 2 mM. Samples containing PSII were prepared in dim green light and dark adapted for 1 hour on ice. All EPR samples (100 μL) were examined in precision 4 mm quartz tubes from Wilmad-LabGlass. Samples in EPR tubes were Illuminated via a dual fiber-optic cable from a single mercury arc lamp with IR (water) and UV (glass) filters. Illumination was both direct and indirect via light reflected/scattered from the silvered Dewar and ice/dry-ice. Illumination at -80 ˚C was for 2 min using both fiber-optic cables. Illumination at 0 ˚C was for 1 min using a single fiber-optic cable with a direct light intensity of ~250 μmole quanta m^{-2} s^{-1}.

Continuous-wave EPR spectra were collected at X-band (9.39 GHz) using 100 kHz field modulation with instrumentation previously described.[60] Liquid helium and a Janis ST-170 ESR Cryostat were used to maintain a sample temperature of 8 K. EPR spectra were collected under non-saturating conditions, 1 G field modulation amplitude and 648 nW microwave observed power.

2.8 - Oxygen Evolution Measurements.

The flash oxygen yield of free PSII CCs and PSII CCs immobilized onto GO-Ni-NTA was measured using a 5 μL ultrasensitive polarographic oxygen cell based on a home-built Clark-type electrode.[61] The cell was illuminated after a 120-second dark preincubation at room temperature. Each sample was

exposed to a 10 ms flash (from an ultra-bright 3W LED at a 50% duty cycle) followed by a 1.2-second long dark period to re-equilibrate PSII and the electron acceptors, repeating the sequence for a total of 200 flashes. The samples preparation proceeded as followed. His-tagged PSII CCs were incubated with GO-Ni-NTA in a buffer containing 50mM sodium phosphate pH 6.5, 10 mM NaCl, 10 mM CaCl2, 10 mM MgCl2, 100 mM MnCl, 15% Glycerol, and 0.05% (w/v) β-dodecylmaltoside for 1 hour on ice. GO-PSII was washed at least three times with the same buffer prior to oxygen evolution experiments. After resuspending to 1 mL, 2 µL of the suspension were diluted with 18 µL of buffer and the corresponding volume (1 or 2 µL) of stock solutions of 20 mM $K_4Fe(CN)_6$, 40 mM dichloro-benzoquinone (DCBQ), or both. Most samples contained 1 mM $K_4Fe(CN)_6$, while DCBQ was supplemented as noted, either at 80 or 160 µM final concentration. Upon mixing of PSII-GO with electron donors and acceptors, 7 µL of the mixture were pipetted into the electrode. The electrode was then sealed with a glass cover, and equilibrated for several minutes in the dark until dissolved oxygen was completely depleted by the electrode. The disappearance of oxygen required about 120 s, which was chosen as dark preincubation period, as described above.

The rates of steady-state oxygen evolution were determined by using a Hansatech Oxygraph System at 45 °C. The PSII and GO-NiNTA-PSII samples were diluted to 1.00 mL using a buffer containing 40 mM MES (pH 6.50), 400 mM sucrose, 15 mM $MgCl_2$, 15 mM $CaCl_2$, 10 mM NaCl, and 100 µM $MnCl_2$. A final concentration of 2 mM $K_3Fe(CN)_6$ was added to the solution prior to measurement. The samples were illuminated with a halogen lamp a 1250 µmol quanta m^{-2} s^{-1} and the rates of oxygen evolution were derived using the Hansatech software. The PSII concentration was determined from Chl content by previous sample extraction with a 1:1 methanol to acetone mixture, using a Beckman DU 640 spectrometer. The measured profiles were smoothed and background-corrected.

3. Results and Discussion

The results show that the presence of DCBQ in addition to ferricyanide has only a small effect on O_2 evolution in the PSII-GO system, while with free PSII, as expected, DCBQ enhances O_2 evolution significantly compared to ferricyanide alone. It is also clear from figure 2.3a that PSII-GO in the presence of mediators/acceptors shows a more rapid decrease in activity compared to free PSII under comparable conditions. Flow cytometry measurements in combination with amino acid analysis allowed us to investigate the linkage between GO-NiNTA and PSII. Results indicate that unmodified GO particles

Figure 2.3 - Oxygen Evolution and Molecular Interactions of GO-NiNTA-PSII.

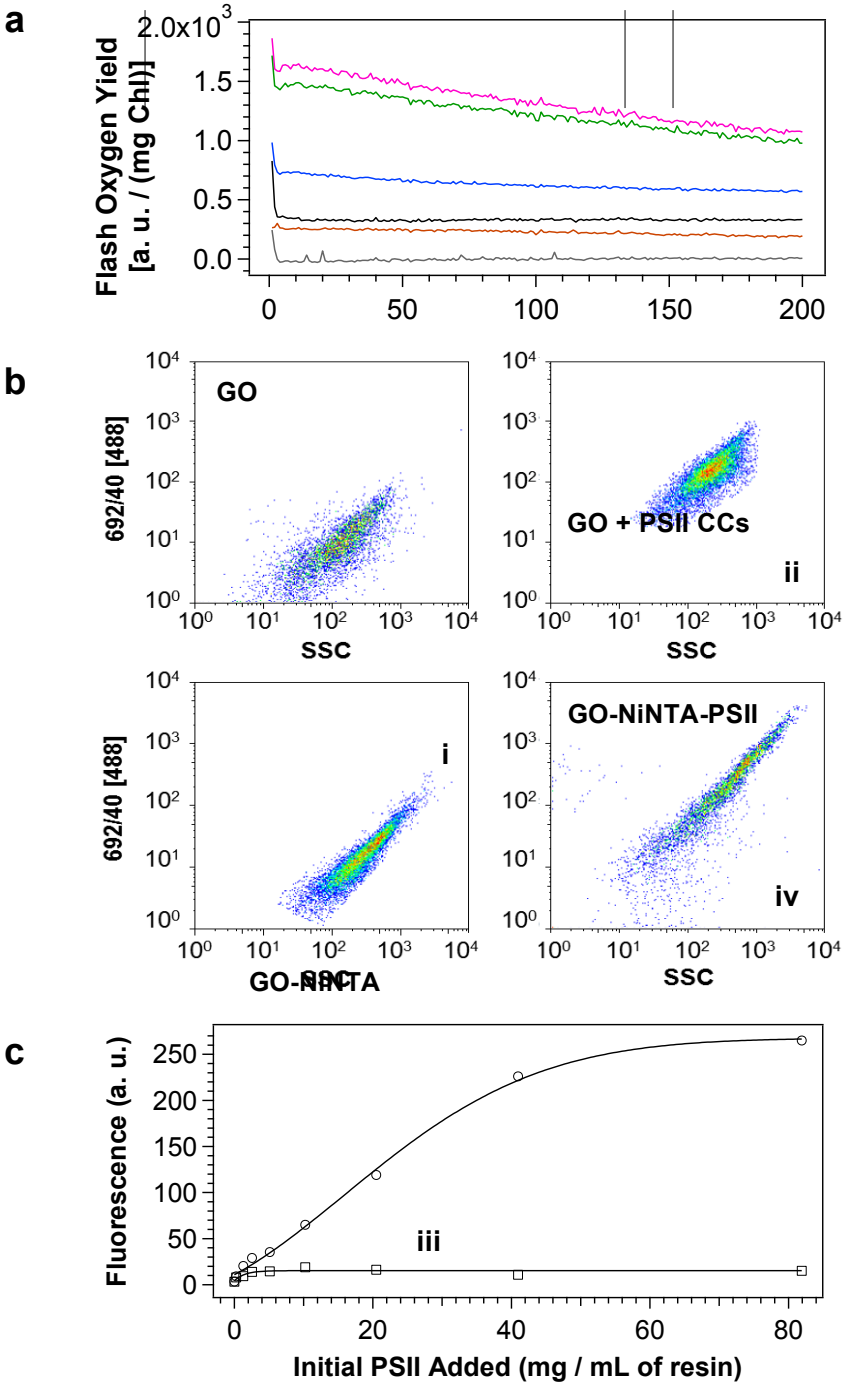

Figure 2.3 | Oxygen Evolution and Molecular Interactions in GO-NiNTA-PSII bio-conjugates based on PSII CCs and graphene oxide (GO). 2.3a) flash oxygen yield of PSII CCs and PSII CCs immobilized onto GO-NiNTA with or without added redox mediators. Each flash was 10 ms with a dark adaptation interval of 1.2 s. The redox mediators are ferricyanide [$Fe(CN)_6^{3-}$], and 2,6-dichloro-*p*-benzoquinone (DCBQ). The purple trace is GO-NiNTA-PSII (1mM $K_3Fe(CN)_6$, 80 μm DCBQ), the green trace is GO-NiNTA-PSII (1mM $K_3Fe(CN)_6$), the blue trace is PSII (1mM $K_3Fe(CN)_6$, 80 μm DCBQ), the black trace is PSII (1mM $K_3Fe(CN)_6$), the brown trace is GO-NiNTA-PSII, and the grey trace is pristine PSII. 2.3b) Flow cytometry maps showing fluorescence at 692 ± 40 nm excited by an interrogating laser at 488 nm versus side scattering (measured perpendicularly to the laser and proportional to size): b(i) pristine GO; b(ii) GO non-specifically bound to His-tagged PSII CCs; b(iii) GO-NiNTA resin; b(iv) GO-NiNTA coordinating His-tagged PSII CCs (GO-NiNTA-PSII). 2.3c) A titration curve of GO-NiNTA resin with His-tagged PSII CCs monitored by flow cytometry. Fluorescence values (at 692 nm) refer to the sample before (circles) and after (squares) washing with the competitive ligand imidazole. Excess PSII is not removed from the sample mixtures

maintain a preferential orientation with respect to the interrogating laser at 488 nm in the experimental time-scale (Figure 2.4). A ratio of the side-scattering to the forward scattering of ~100 confirms that the observed events are consistent with individual particles characterized by a high aspect ratio, as expected for nearly monoatomic layers of GO (1-5 μm in lateral size). A marked increase in fluorescence and a slight increment in side scattering are observed when comparing pristine GO with a mixture of GO and PSII (Figure 2.3b). These results suggest that PSII can interact non-specifically with each side of the individual GO flakes, slightly increasing the particle size. This is consistent with the observation that using our instrumental settings, the sidescattering of isolated PSII in suspension is nearly zero. When GO is chemically modified with NiNTA functional groups (GO-NiNTA), His-tagged PSII can link to the Ni^{2+} coordination sites. The side-scattering of GO-NiNTA alone is shifted to higher values than that of unmodified GO, as expected; however, the fluorescence signal of GO-NiNTA-PSII is distinctly different from PSII non-specifically bound to GO and appears to be related to the extent of specific protein coverage on the GO-NiNTA flakes. This can be inferred from the strong statistical correlation between the fluorescence emission and the side scattering. Flow cytometry measurements in combination with amino acid analysis allowed us to determine by titration that there is a maximum protein loading of PSII per volume of GO-NiNTA resin in suspension and a minimum initial concentration of PSII required for saturating the resin (Figure 2.3c). Elution with imidazole results in a clear decline of the fluorescence signal, indicating that bound PSII complexes are detached from the surface of the resin by a competing ligand. A more accurate value of the PSII loading after repeated washing was determined by absorption spectroscopy at 680 nm and was shown to be equal to 9.72 mg of PSII per mL of wet resin precipitate.

Figure 2.4 - Flow Cytometry of GO

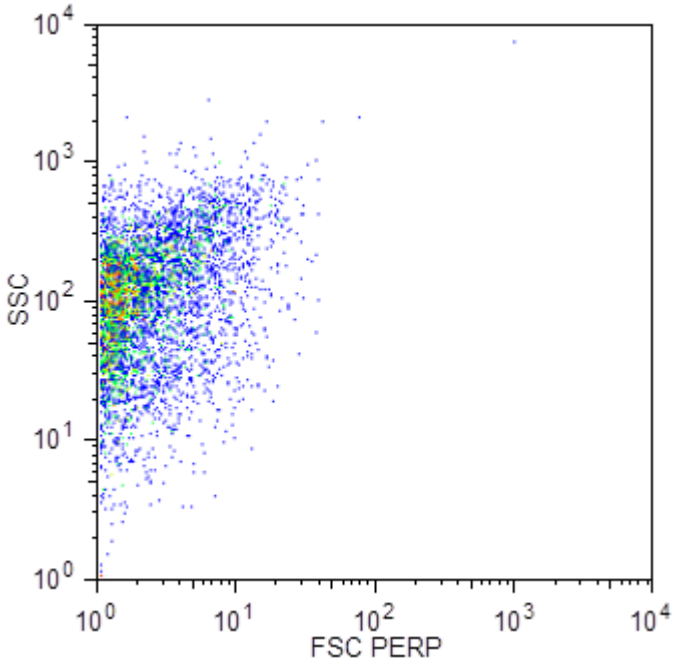

Figure 2.4 | Analysis of pristine GO by flow cytometry (SSC = side scattering, FSC PERP = forward scattering, perpendicular to SSC).

To obtain insight into the electron transfer characteristics, fluorescence kinetics measurements were conducted by a single turnover flash (STF) followed by relaxation comparing GO-NiNTA-PSII with isolated PSII, as shown in Figure 2.5a. Typical results indicate 59% residual quantum yield of photochemistry (F_v/F_m=0.41) compared to PSII in suspension (F_v/F_m=0.70). The fitting of the fluorescence relaxation profiles of PSII and GO-NiNTA-PSII (Figure 2.5b) requires three and two exponential terms, respectively. In the case of free PSII a τ_2 of 4 ms reflects the expected time-scale of a single electron transfer between Q_A and Q_B entering the acceptor-side pocket. For immobilized PSII a $\tau_1^{'}$ of less than a millisecond suggest the possibility of direct electron transfer from Q_A to GO and/or indirect electron transfer mediated by Q_B. These data suggest that GO-NiNTA provide alternative electron acceptor sinks

for PSII, and can effectively substitute for the plastoquinone pool *in vitro*. The ability of GO to accept electrons is indicated in Figure 2.5c where an additional stabilization effect on immobilized PSII for about 15 turnovers is shown.

The charge injection from PSII into GO substrates can be monitored using EPR. The EPR results shown in Figure 2.6a reveal the increment of intensity of a radical found in GO-NiNTA when immobilized PSII is present. The original radical signal in GO-NiNTA is attributed to electrons delocalized in the plane of GO. We hypothesize that ring opening and protonation of the epoxy groups on the plane of GO, as schematically shown in Figure 2.6b, capture the extra electrons that are injected from PSII.[62] The observed radical signal increment in EPR is similar to that caused by a mild reductant such as ascorbate and cannot be attributed to the overlapping Tyr_{D}· spectral features (indicated by the arrows in the Figure 3.6a).

The rate of oxygen evolution at 45 °C in GO-NiNTA-PSII under continuous light in the presence of ferricyanide increases above 7900 μmol O_2 / (mg Chl · h), more than twice the rate observed in the case of PSII (3500 μmol O_2 / (mg Chl · h)) (Figure 2.7). The measured rate indicates an oxygen turnover rate of 2 O_2 Chl^{-1} s^{-1} and an oxygen turnover time of 14 ms per PSII. This rate rapidly decays, most likely due to diffusion limitations of the redox mediator, re-reduction of PSII by electron-saturated GO and photodamage caused by reactive oxygen species. However, the initial volumetric photocurrent density in the GO-NiNTA-PSII suspensions can reach 5.5 mA/mL. This value is compatible with the theoretical maximum volumetric current density (15 mA/mL) calculated on the basis of the functional absorption cross section (29.7 $Å^2$/q) interpolated across the visible spectrum (365-750 nm) of PSII under the same illumination conditions.[63] A light-saturation factor of 10% is considered. The potential of using GO-NiNTA-PSII replicants in suspension is clear: the enormous surface advantage provided by the GO nanostructures can overcome trivial surface current densities generated by individual PSII monolayers.[63]

The observed rates may prove to be sustainable in the presence of efficient downstream electron-acceptors yielding functional bio-hybrid electron transport chains. A similar design strategy may be applicable to other types of bio-inspired electrochemical systems.

Table 2.1 - Electron Paramagnetic Resonance Parameters.

Sample description	Peak-to-peak High (mV)	Peak-to-peak Width (G)	Comments
GO-NiNTA-PSII, DCMU, Illuminated at 0 °C	585	2.5	Significant YD signal
GO-NiNTA-PSII, Illuminated at 0 °C	603	2.5	Significant YD signal
GO-NiNTA-PSII, Illuminated at -80 °C	610	2.7	Significant YD signal
GO-NiNTA-PSII, lower PSII loading, Illuminated at 0 °C	600	2.7	Modest YD signal
GO-NiNTA, $K_3Fe(CN)_6$, non-illuminated	367	2.7	Only GO radical observed
GO-NiNTA, ascorbic acid, non-illuminated	500	2.7	Only GO radical observed
GO-NiNTA, control, non-illuminated	335	3.0	Only GO radical observed
GO-NiNTA, illuminated @ 0 °C	400	2.9	Only GO radical observed
GO-NiNTA, illuminated @ -80 °C	385	2.6	Only GO radical observed

4. Conclusion

The investigation of GO-NiNTA-PSII biohybrid photosynthetic systems shows that it is possible to transfer electrons directly and indirectly from PSII CCs to the GO support. This bioconjugate systems result in an increased water oxidation rate by the water oxidation complex. Two types of different oxygen evolution experiments were conducted under steady-state and transient conditions. In both cases a factor of 2-3 enhancement of oxygen evolution activity was observed. The stationary rate of oxygen evolution at 45 °C in GO-NiNTA-PSII under continuous light in the presence of ferricyanide increases above 7900 mol O_2 / (mg Chl · h), more than twice the rate observed in the case of PSII (3500 mol O_2 / (mg Chl · h)).

.

Figure 2.5 - Fluorescence kinetics and relaxation studies of GO-NiNTA-PSII and free PSII

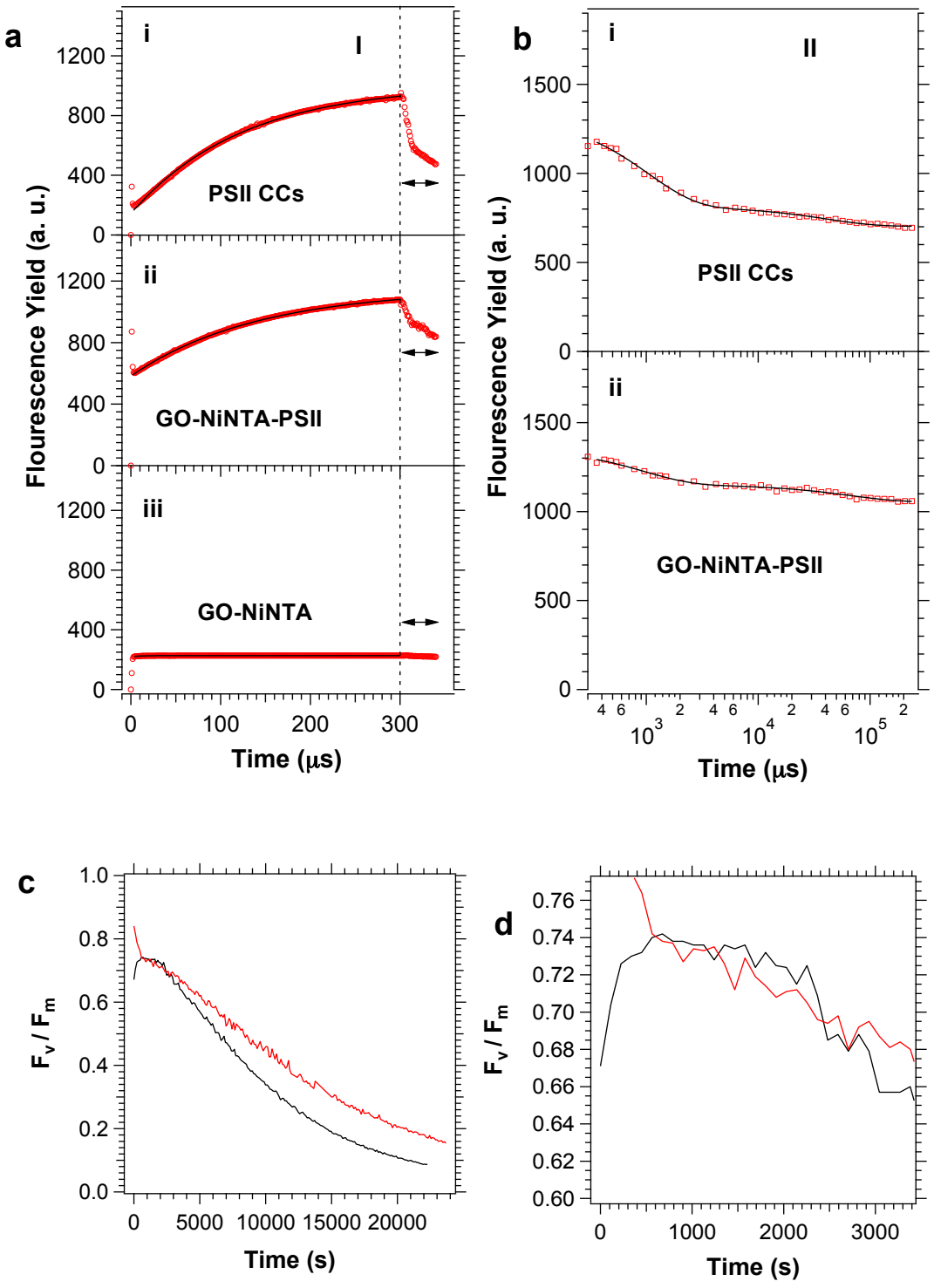

Figure 2.5 | Fluorescence kinetics studies of GO-NiNTA-PSII as opposed to free PSII CCs. a, fluorescence induction and relaxation measurements. The effects of STF-τ experiments (STF: single turnover flash, τ: fluorescence relaxation) on isolate PSII CCs and PSII CCs coordinated to GO-NiNTA resin, and the resin without PSII CCs are shown in Figures 3.5a(i), 3.5a(ii) and 3.5a(iii). 3.5a(i), fluorescence yield *versus* time of PSII CCs from *T. elongatus in vitro*, STF(300μs)-τ(236 ms),), the width of the relaxation region is 236 ms (indicated by the double arrow); 3.5a(ii), PSII CCS tethered to GO-NiNTA resin, STF(300μs)-τ(236 ms); 3.5a(iii), GO-NiNTA resin without PSII CCs. Proteins STF(300μs)-τ(236 ms). All measurements are the average of 10 iterations. 3.5b, expansion of Region II in Figures 3.5a(i) and 3.5a(ii) with fitting. 3.5b(i), the fitting requires three exponential terms corresponding to the time constants τ_1, τ_2, and τ_3; 3.5b(ii), the fitting requires two exponential terms corresponding to the time constants $\tau_1^{'}$ and $\tau_2^{'}$. 3.5c, deactivation study of isolated PSII CCs (red profile) and PSII CCs attached to GO-NiNTA (black profile) in terms of the decline in quantum yield of photochemistry (F_V/F_m) *versus* time. 3.5d, expansion of the initial values of the curves in Figure 3.5c. PSII CCs in both samples were treated under the same incubation and buffer conditions at 4 °C before each measurement conducted at room temperature.

Figure 2.6 - Charge-Transfer Characteristics of PSII CCs immobilized on GO-NiNTA in comparison to free PSII CCs.

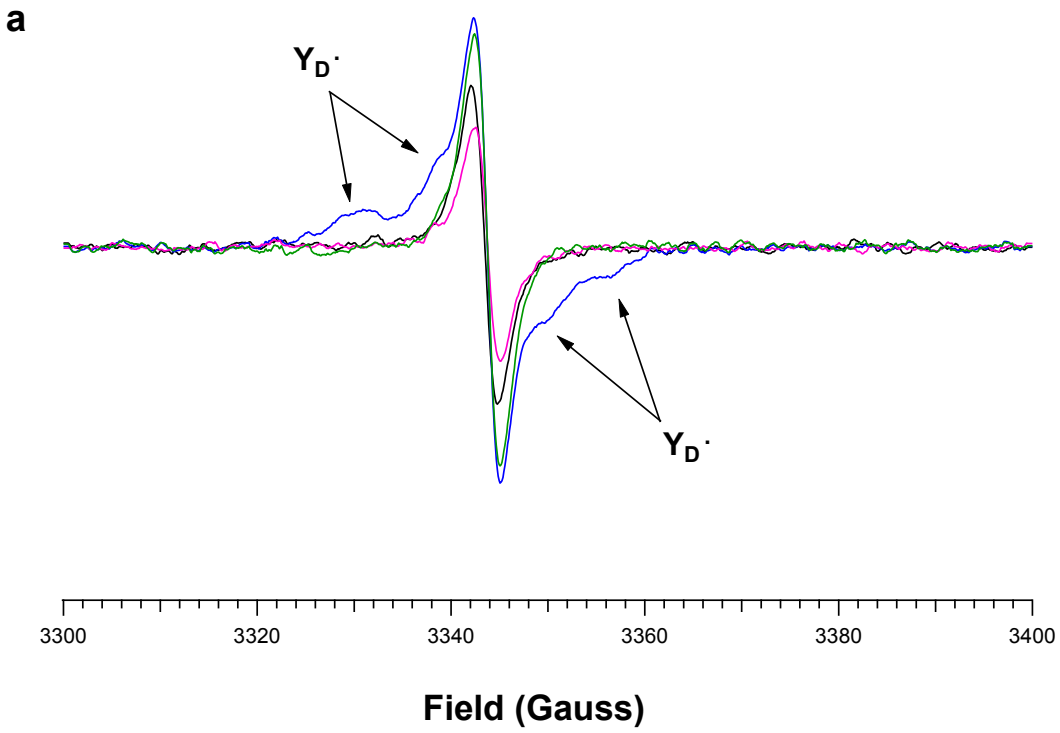

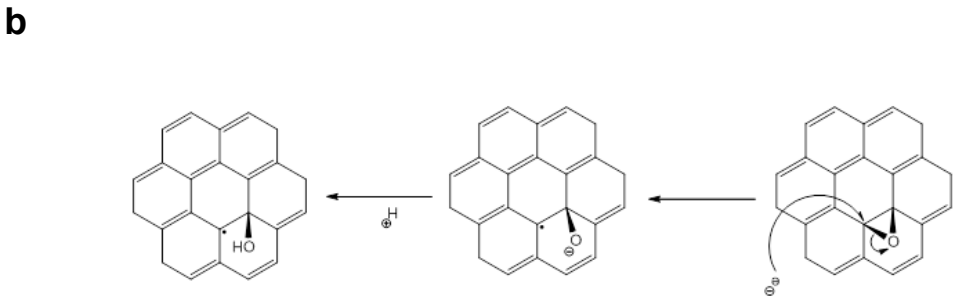

Figure 2.6 | Charge-Transfer Characteristics of PSII CCs immobilized on GO-NiNTA in comparison to free PSII CCs.

3.6a, electron paramagnetic resonance (EPR) spectra of the pristine GO-NiNTA resin and in the presence of a mild reductant (ascorbate) in solution or PSII CCs coordinated on the surface of the resin. The tyrosine D $Tyr_{D^{\cdot}}$ ($Y_{D^{\cdot}}$) radical signal is subtracted to show only the radical signal from GO. The blue trace refers to GO-NiNTA-PSII bio-conjugates, the green trace refers to GO-NiNTA-PSII bio-conjugates minus the EPR signal from free PSII CCs, the black trace refers to GO-NiNTA in the presence of ascorbate, and the purple trace refers to GO-NiNTA. 3.6b, a mechanistic hypothesis concerning the nature of the radical signal on GO in terms of ring opening and protonation of epoxy groups on the surface of GO.

Figure 2.7 – Steady State Oxygen Evolution

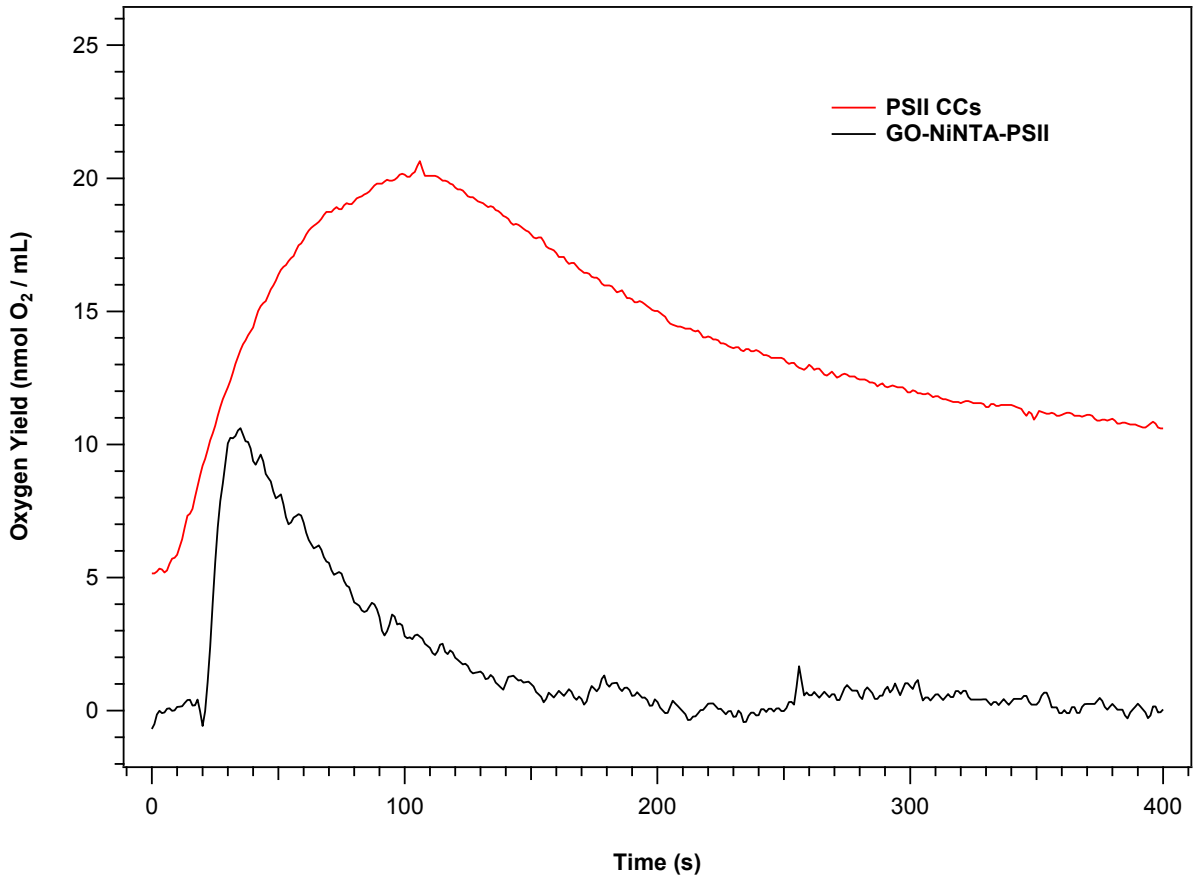

Figure 2.7 | Oxygen yield under continuous illumination at 1250 µmol quanta m^{-2} s^{-1} of PSII CCs and PSII immobilized on the GO-NiNTA resin at 45 °C. Illumination was started at 0 sec. The original GO-NiNTA-PSII profile was multiplied by a factor of 3 to account for the difference in Chl a content in the samples, for the purpose of a direct comparison with the PSII profile.

Chapter III. Kinetic Study of a Biohybrid Electron-Transport Chain Based on Photosystems II and I Coupled to Graphene Oxide

1. Introduction

In all oxygenic photosynthetic organisms, photosystems I and II reaction centres (PSI and PSII RCs) convert photon energy to electrical potentials with extraordinary efficiency, 45±10% and 80±15%, respectively,[14] under a wide range of light and temperature conditions.[64] PSII RCs oxidize water to generate oxygen and protons on the luminal side of the thylakoid membrane while translocating electrons toward the stromal side.[65, 66] In principle, this reaction can be re-engineered with isolated CCs on solid interfaces to convert light into chemical energy in the form of hydrogen and oxygen gases.[67] Although progress in the fields of genomics, molecular genetics, biochemistry, biophysics, materials science, and engineering makes such a device tantalizingly close, a functional system has remained elusive. Membranes with oriented photosynthetic CCs have been assembled,[68-71] and attempts have been made to integrate photosynthetic protein complexes in solid-state devices such as photodetectors, photovoltaic cells, and photoelectronic devices.[31, 32, 72-90] PSII CCs have been immobilized onto electrodes for assembling biosensors.[91-96] PSII and PSI CCs have been immobilized as components of a future biohydrogen production device.[11, 97, 98] Hydrogen generation *via* solid-state integration of isolated PSII and PSI CCs with hydrogenases has been suggested, although a full device has yet to be assembled.

Several approaches for biological and biomimetic energy conversion systems have been proposed.[99, 100] In particular, the possibility of using photosynthesis to produce hydrogen from biological resources is summarized in Esper et. al. [67] Both natural microorganisms or semi-artificial devices are being investigated within various national and international programs. Most approaches being followed on the front of semi-artificial devices strive toward a photoelectrochemical system based on PSII, PSI, and hydrogenase. The original model, proposed since 1979, [101] entailed the use of particles floating in

solution in the presence of redox mediators. Agostiano et al.[47] succeeded in the remarkable task of making a galvanic device for H_2-generation based on PSII- and PSI-enriched particles immobilized onto Pt electrodes. The PSII and PSI particles were not as refined as those available today. So far, no one has ever published a full working device using isolated CCs.[67] New strategies involve the immobilization of PSII, PSI CCs and hydrogenases onto electrodic surfaces. A critical evaluation of direct biophotolysis of water using hydrogenases points out that the maximal energetic efficiency of hydrogen production at a wavelength of 680 nm is about 41%, but a negative issue is represented by oxygen sensitivity of hydrogenases.[102] This estimate in principle applies to both systems based on natural microorganism and semi-artificial devices. In practice, a more realistic estimate is set at 10%.[12]

Graphene oxide (GO) was recently discovered as an alternative path to graphene.[103-108] GO is an extremely interesting material in its own right.[109] GO can be synthesized by exfoliating graphite under strong oxidation conditions followed by subsequent reduction. The residual oxygen-containing chemical species include hydroxyl, carboxyl, epoxy, and ketonic functional groups concentrated at the edges of graphene quantum islands. The presence of oxygen functional groups disrupt the graphene sp^2 network transforming 40% of the carbon bonds into sp^3 bonds above a C/O ratio of 5:1 (20%-oxygen content). Above this ratio, GO is an undulated surface with 0.6 nm roughness.[109] The degree of oxidation can be used to control electron/hole transport properties. GO nanosheets provide an ideal chemical "canvas" for the self-assembly and investigation of photosynthetic proteins for several reasons. GO is a solution-processable material. The presence of polar oxygen-containing functional groups on the surface allows one to obtain high-concentration suspensions in aqueous solutions. The higher the oxygen content, the easier it is to suspend GO in water. Suspensions are possible at oxygen-content between 8% and 35%.[110] Concentrations up to 2.5 mg/mL and 5 mg/mL are possible at 8% to 35% oxygen-content, respectively. Slurries with a concentration up to 50 mg/mL can be prepared.[111] GO is amenable to click-chemistry surface modification.[112] GO is a single layer surface electron conductor at low oxygen-content (8%) and a

surface hole-conductor at high oxygen content (35%). The surface electronic conductivity varies between 10^{3} to 10^{-9} $S \cdot cm^{-1}$ in going from the lowest to the highest oxygen content. However, electronic transfer by tunneling is possible normally to the layer at all oxygen contents. GO is characterized by hydrophobic carbon regions and by the polar oxygen functional groups. The amphiphilic character of GO makes it highly biocompatible as a protein support, in spite of observed evidence for cytotoxicity.[113-122] GO in suspension at low concentrations and as thin film, is transparent, thus making it an ideal substrate for optical spectroscopy studies and potentially for vibrational spectroscopy investigations of photosynthetic proteins tethered to its surface.[111] GO can be readily deposited to give large area films at low cost. GO thin films can be formed virtually on any given substrate including glass, metals, and plastics.[111] GO obviates the need for Indium Tin Oxide (ITO), which uses a rare element. GO can be used as an interface for assembling proteins,[123, 124] and in particular, photosynthetic molecules. The self-assembly of photosynthetic proteins can occur onto thin-films on solid substrates. Both sides of a GO nanosheet are accessible for self-assembly in the case of nanosheets suspended in aqueous solution. Contrary to carbon nanotubes, useful tethering groups on the surface are widely distributed and not mainly concentrated at the ends.[74, 87, 88]

To analyze the connectivity of the system, the PSI was probed using the Joliot-type Spectrophotometer (JTS), which provides high-resolution and is specifically designed for electron-transfer studies in photosynthetic organisms via fluorescence and absorbance changes. JTS utilizes two sample locations with their own monochromatic illumination sources, tandem photodetectors, and the ability to compare these signals.[125, 126] The samples are at right angles of each other with a light source split by a diffraction grating. The JTS has been used to study PSI and PSII, and is capable of distinguishing between cyclic versus linear electron flow. This technique is often used to investigate non-photochemical quenching, carotenoid bandshifts, transthylakoid pH variations, and for probing cytochrome b, *f*, b_6f. Measurements of the activity of PSI entail the induction of an absorption change in

P_{700} with suitable light flashes.[127, 128] The absorption changes at 700 nm signal the changes occurring within the P_{700} chlorophyll a pair.[129-131] JTS has been used to measure the PSI/PSII ratio in cells/systems. This is done by observing the fast phase change in amplitude of the saturating light conditions of the laser excited electrochromic shift signal.[130] The electrochromic shift change shows a linear correlation with the number of light induced charge separations in the photosynthetic complexes.[131] PSI/PSII ratios can be determined by comparing the spectral evidence of the charge separation of the intact system as compared to the change when an inhibitor (such as DCMU) is introduced deactivating the PSII reaction center.[130]

This chapter presents a JTS study of PSII-(GO-NiNTA)-PSI, a system comprised of PSII His-tagged on the stromal side, PSI His-tagged on the luminal side, and graphene oxide functionalized with Nickel nitriloacetic groups.[132] The central focus of this chapter is to gather evidence in support of electron-transfer between PSII and PSI through GO.

2. Methods

2.1 - Synthesis of GO-NiNTA

The starting material was a suspension containing graphene oxide (GO) with 20% oxygen content provided by the Nano-materials and Devices Group at Rutgers University.[132] The entire preparation process was conducted at room temperature. The GO was modified by a room temperature reaction with 10 mM N-hydroxysuccinimide (NHS) and 10 mM N-ethyl-N'-(3-dimethylaminopropyl)-carbodiimide, both of which were in excess to the carboxyl groups on the GO. Afterwards, the suspension was then washed with ultra-pure water to form a graphene derivative containing activated carboxyl groups. The washed precipitate was then treated with a 150 mM N_a,N_a-bis(carboxymethyl)-L-lysine hydrate (pH=9.8) solution. The washed precipitate was subsequently treated with a 100 mM solution of $NiSO_4$ to provide a graphene derivative containing nickel ions (i.e., GO-Ni-NTA). The resultant resin was stored as a wet precipitate at 4˚C for further use. A more detailed discussion of the synthesis can be found in the appendix.

2.2 - Synthesis of GO-NiNTA-PSI and PSII-(GO-NiNTA)-PSI

PSII CC that were His-tagged on the protein domain CP_{47} were isolated from a thermophilic cyanobacterium *T. elongatus* using a previously reported protocol.[63] PSII CC is a dimeric protein with a physical dimension of 20.5 nm (L) x 11.0 nm (W) x 10.5 nm (D) and a molecular weight of 680 kDa. PSI CCs that were His-tagged on the luminal side were isolated from *Synechococcus sp. 7002* by John Golbecks's lab at Pennsylvania State University using an *ad hoc* procedure. [37, 133] The structure of the PSI CCs protein from *Synechococcus sp. 7002* is similar to that of the PSI CC protein form *Synechococcus elongatus*, whose structure has been resolved at atomic level by x-ray crystallography. The PSI CC protein thus obtained had a trimeric structure. The cylindrical trimer had a diameter of 22 nm and a height of 10 nm. His-tagged PSI CC (3.5 μL of a suspension 3.0 mg Chl a / mL) and PSII CCs (20 μL of a

suspension 0.5 mg Chl a / mL) were incubated in a suspension containing the GO-Ni-NTA resin (10 μL of 25% v/v suspension of resin) for 60 minutes at 4 °C. The suspension were centrifuged (21,000g) and washed three times with a buffer comprised of 50 mM MES (4-morpholineethanesulfonic acid), 10 mM $MgCl_2$, 10 mM NaCl, 10 mM $CaCl_2$, 15% glycerol, 0.05% β-DM (n-dodecyl-β-D-maltoside), pH 6.5. This allowed the preparation of GO-NiNTA-PSI and PSII-(GO-NiNTA)-PSI in suspension. On the basis of amino acid analysis it is calculated that the PSII/PSI ratio for PSII-(GO-NiNTA)-PSI in suspension is equal to 1.9.

2.3 - Joliot-type Spectroscopy of PSII-(GO-NiNTA)-PSI

The PSII-(GO-NiNTA)-PSI suspension was further prepared for JTS measurements. Ficoll at a final concentration of 20% v/v was used as a stabilizer. Dichlorophenol indophenol (DCPIP, 25μM), ascorbic acid (500 μM), and methyl viologen (MV, 500 μM) were utilized as PSI mediators. Potassium ferricyanide ($K_3Fe(CN)_6$, 1mM) and dichlorobenzoquinone (DCBQ, 80 μM) served as electron acceptors for PSII. Joliot-type Spectroscopy (JTS) was used in absorbance change mode to probe PSI and in fluorescence change mode to interrogate PSII. The state of oxidation of PSI was measured using LED probing light in the interval 700-740 nm filtered with three band-pass filters (705 ± 3 nm): one before beam splitter, and two before sample and reference detectors. Steady state oxidation level of PSI was achieved by continuous green actinic LED light at 532 nm (50 μmol / (m^2s)). Light saturation of PSI was obtained using a single 200 ms pulse of orange actinic LED light at 639 nm (3000 μmol / (m^2s)). PSII's fluorescence was monitored using white light filtered using a fluorescence filter (420 ± 90 nm) before the beam splitter, with a similar filter on the reference detector (480 ± 150 nm). A high-pass filter allowing only wavelengths higher than 660 nm to pass detected emission. Steady state oxidation of PSII was achieved using continuous 639 nm orange actinic LED light (150 μE/ (m^2s)) for 20 s. The same experiments were repeated on the same PSII-(GO-NiNTA)-PSI suspension before and after addition of imidazole as decoupling agent (200 mM). Figure 3.1 represents a typical JTS measurement profile in absorbance change mode of PSI CCs. At time zero it is assumed that the PSI CCs are completely reduced,

and this is asserted by the excess of ascorbate and DCPIP in the sample. This dark adapted sample is illuminated with the green light to bring to a steady state. After that is achieved an orange flash of about 200 milliseconds (ms) completely oxidizes the P_{700}. From this absorbance change we can find the rate of P_{700} oxidation, the P_{700}^{+} saturation ($[P_{700}^{+}]_{sat}$) and the P_{700} steady state contribution. ($[P_{700}^{+}]_{S.S.}$) During the "dark phase" we can find the rate of re-reduction of the P_{700}.

Figure 3.1 - Typical Joliot-type spectroscopy measurements profile

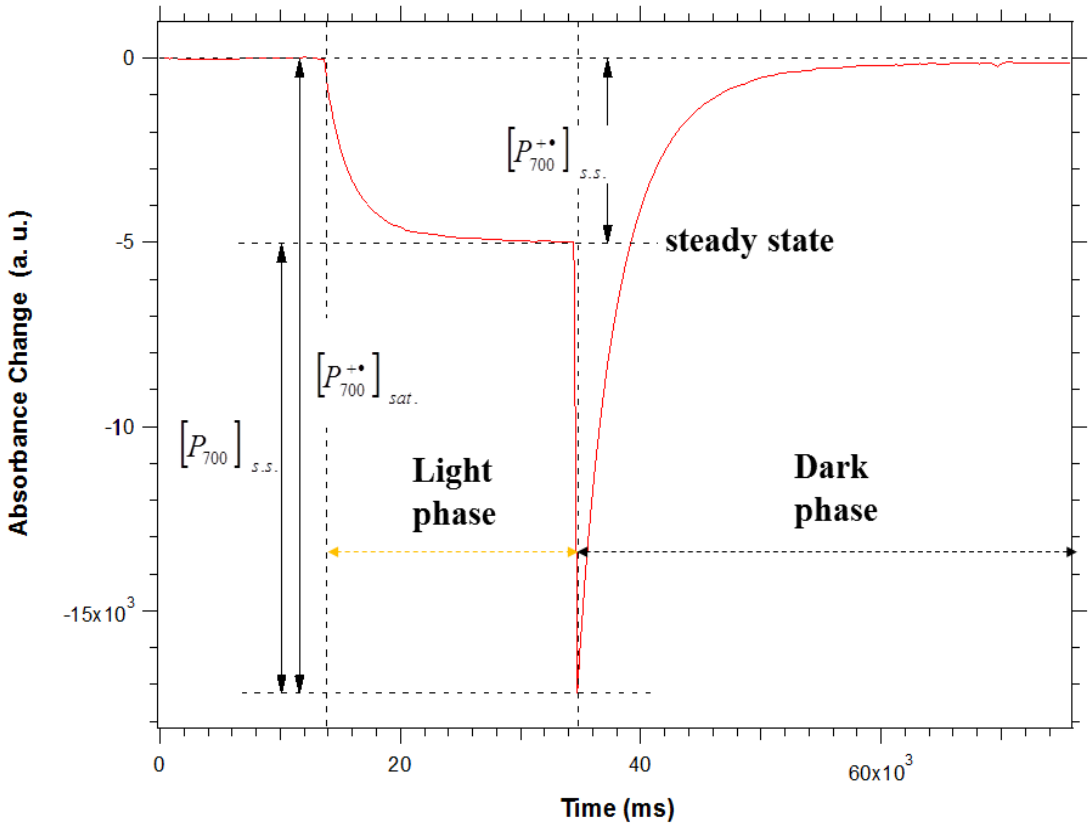

Figure 3.1 | Typical Joliot-type spectroscopy measurements profile in absorbance change mode of PSI CCs. The dark-adapted sample is illuminated with green light at 532 nm and then saturated with a 100 μs orange flash at 639 nm. In the dark phase re-reduction occurs thanks to suitable redox mediators. Dichlorophenol indophenol (DCPIP) is the primary donor, ascorbate is the auxiliary donor, and methyl viologen (MV) is the terminal electron acceptor.

3. - Results and Discussion

3.1 - Kinetic Model: PSI CC System

JTS spectroscopy can probe the light-induced and chemically induced oxidation state changes of PSI by following the primary electron donor in reduced form (P_{700}) and oxidized form ($P_{700}^{+\bullet}$). A typical JTS measurement in absorbance change mode of PSI CCs is shown in Fig. 4.1. P_{700} can be oxidized to $P_{700}^{+\bullet}$ by light with wavelength below 700 nm in a forward half-reaction characterized by the irradiance-dependent kinetic constant k_{PSI} , $k_{PSI} = k_{PSI}[light]$ (see Scheme 4.1, I).

Scheme 3.1 - Kinetic semi-reactioins

(I) $$P_{700} \underset{k_D[DCPIP]}{\overset{k_{PSI}}{\rightleftarrows}} P_{700}^{+\bullet} + e^-$$

(II) $$P_{700} \underset{k_D[DCPIP]\ \varphi}{\overset{k_{PSI}}{\rightleftarrows}} P_{700}^{+\bullet} + e^- \qquad k_{GO}[GO_{red}] \leftarrow GO_{red}$$

(III) $$P_{700} \underset{k_D[DCPIP]\ \varphi}{\overset{k_{PSI}}{\rightleftarrows}} P_{700}^{+\bullet} + e^- \qquad k_{GO}[GO_{red}] \leftarrow GO_{red} \leftarrow k_{PSII}[P_{680}]$$

Scheme 3.1 | Kinetic semi-reactions relevant to PSI CC (I), PSI CC on GO-NiNTA (II), and the PSII-(GO-NiNTA)-PSI biohybryd electron transport chain (III).

The probability of the corresponding spontaneous dark back-reaction is assumed to be small under the adopted experimental conditions. The re-reduction of $P_{700}^{+\bullet}$ to P_{700} in the dark occurs only by virtue of the chemical donor as characterized by the kinetic constant k_D. This re-reduction occurs in the light, as well. The term 'donor' indicates the primary donor DCPIP in the presence of an excess of ascorbate as auxiliary donor. The excess auxiliary donor ensures that DCPIP is for the most part in a reduced state, unless it is utilized by the acceptor side of PSI. The following two differential equations need to be considered:

$$-\frac{d[P_{700}]}{dt} = k_{PSI}[P_{700}] \qquad \text{(Eq 3.1)}$$

$$-\frac{d[P_{700}^{+\bullet}]}{dt} = k_D[P_{700}^{+\bullet}]\cdot[donor] \qquad \text{(Eq. 3.2)}$$

The steady state (s.s.) condition is reached when the electronic flows represented by equations (Eq. 3.1) and (Eq. 3.2) are equal and therefore the following relationship is satisfied:

$$k_{PSI}[P_{700}]_{s.s.} = k_D[P_{700}^{+\bullet}]_{s.s.}\cdot[donor] \qquad \text{(Eq. 3.3a)}$$

A simple rearrangement will give:

$$\frac{[P_{700}^{+\bullet}]_{s.s}}{[P_{700}]_{s.s}} = \frac{k_{PSI}}{k_D[donor]} \qquad \text{(Eq. 3.3b)}$$

The mass balance requires that:

$$[P_{700}]_{tot} = [P_{700}^{+\bullet}] + [P_{700}] \approx [P_{700}^{+\bullet}]_{s.s.} + [P_{700}]_{s.s.} = [P_{700}^{+\bullet}]_{sat} \approx [PSI] \qquad \text{(Eq. 3.4)}$$

The meaning of most of these terms is elucidated in Fig. 3.1. The mass balance is valid at all times t, not only at the steady state $[PSI]_{tot}$ indicates the total amount of PSI in the system. It is assumed that $\left[P_{700}^{+\bullet}\right]_0 = 0$ at time t = 0. It is convenient to consider an origin shift in such a way that t = 0 when the green light at 532 nm is turned on. The requirement that all PSI is in a reduced form is compatible with the experimental requirement that ascorbate is present in excess. The solution of equation (Eq. 3.2) provides an expression for the concentration of $P_{700}^{+\bullet}$ at time t in the dark phase:

$$\left[P_{700}^{+\bullet}\right]_t = \left[P_{700}^{+\bullet}\right]_{sat} \cdot e^{-k_D[donor]t} \qquad \text{(Eq. 3.5)}$$

The combination of equations (Eq. 3.1) and (Eq. 3.2), considering the boundary condition expressed by (Eq. 3.4) gives the following equation:

$$-\frac{d\left[P_{700}^{+\bullet}\right]}{dt} = k_D\left[P_{700}^{+\bullet}\right]\cdot[donor] - k_{PSI}\left(\left[P_{700}\right]_{tot} - \left[P_{700}^{+\bullet}\right]\right) \qquad \text{(Eq. 3.6)}$$

The solution of equation 3.6 provides an expression for the concentration of $P_{700}^{+\bullet}$ at time t in the light phase, where light-induced oxidation of P_{700} is contrasted by its concomitant chemical re-reduction:

$$\left[P_{700}^{+\bullet}\right]_t = \frac{k_{PSI}[PSI]}{k_{PSI} + k_D\cdot[donor]}\left(1 - e^{-\{k_{PSI}+k_D\cdot[donor]\}t}\right) \qquad \text{(Eq. 3.7)}$$

This equation holds true provided that the condition $\left[P_{700}^{+\bullet}\right]_0 = 0$ is satisfied. The presence of DCPIP with excess ascorbate, assures just that.

Figure 3.2 – EPR of GO-NiNTA and Conjugates

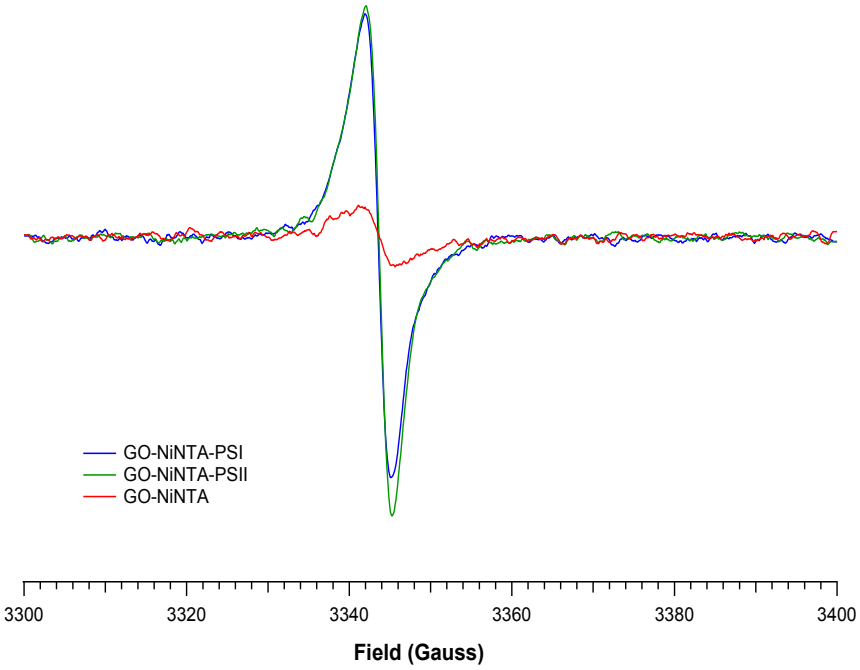

Figure 3.2 | The native radical signal present in GO-NiNTA can be enhanced by both PSI and PSII, indicating that GO acts like a sink of electrons for both photosystems.

3.2 - Kinetic Model: GO-NiNTA-PSI System

When PSI CCs are immobilized onto GO nanosheets in addition to the forward light-driven semi-reaction from P_{700} to $P_{700}^{+\bullet}$ and the re-reduction from $P_{700}^{+\bullet}$ to P_{700} due to the chemical donor, there is the possibility of a new dark semi-reaction involving re-reduction of $P_{700}^{+\bullet}$ to P_{700} by GO (see Scheme 3.1, II). GO is expected to act as an electron sink for the electrons. As shown by electron paramagnetic measurements (EPR) in Fig. 3.2, GO is characterized by a native radical signal, which is attributed to electronic radicals of the same kind trapped in the extended conjugated system of the basal plane of GO. The native radical can be enhanced by reduction of GO by electrons emerging at the acceptor side of PSI that trickle back down to GO. Reduced MV is also likely to reduce GO. Therefore, reduced GO is capable of re-reducing $P_{700}^{+\bullet}$ to P_{700}.

The ability of DCPIP to re-reduce $P_{700}^{+\bullet}$ to P_{700} is partially impaired by the fact that PSI CCs are immobilized on the lumen side onto GO. The His-tags assure the vectorial orientation of PSI. The oxygen functional groups (-OH and epoxy groups) on the surface of GO are likely to promote secondary interactions between the acceptor side of PSI and GO. These interactions are expected to be mainly hydrogen-bonding between PSI and –OH groups. Therefore, the coordinative interactions of the His-tags of PSI with GO-Ni-NTA, and hydrogen-bonding restrict the access of DCPIP to the acceptor side of PSI bound to GO. For this reason the factor φ, accouning for the sterical accessibility of the chemical donor to the acceptor side of PSI when GO is present, was introduced ($0 \leq \varphi \leq 1$).

The two differential equations necessary to describe GO-NiNTA-PSI are (Eq. 3.1) and (Eq. 3.8):

$$-\frac{d\left[P_{700}^{+\bullet}\right]}{dt} = \left\{k_D\left[donor\right]\varphi + k_{GO}\left[GO\right]\right\}\cdot\left[P_{700}^{+\bullet}\right] \qquad \text{(Eq. 3.8)}$$

The steady state condition is achieved when the electronic flows of (Eq. 3.1) and (Eq. 3.8) are equal. This condition is satisfied when equation (3.9a) holds true:

$$k_{PSI}\left[P_{700}\right]_{s.s.} = \left\{k_D\left[donor\right]\varphi + k_{GO}\left[GO\right]\right\}\cdot\left[P_{700}^{+\bullet}\right]_{s.s.} \quad \text{(Eq. 3.9a)}$$

The same equation can be rearranged to give equation (Eq. 3.9b):

$$\frac{\left[P_{700}^{+\bullet}\right]_{s.s.}}{\left[P_{700}\right]_{s.s.}} = \frac{k_{PSI}}{k_D\left[donor\right]\varphi + k_{GO}\left[GO\right]} \quad \text{(Eq. 3.9b)}$$

The solution of equation (Eq. 3.8) provides an expression for the concentration of $P_{700}^{+\bullet}$ at time t in the dark phase:

$$\left[P_{700}^{+\bullet}\right]_t = \left[P_{700}^{+\bullet}\right]_{sat} \cdot e^{-\left\{k_D\left[donor\right]\varphi + k_{GO}\left[GO\right]\right\}\cdot t} \quad \text{(Eq. 3.10)}$$

Using equations (Eq. 3.1) and (Eq. 3.8), considering the boundary condition expressed by (Eq. 3.4) gives the following equation:

$$-\frac{d\left[P_{700}^{+\bullet}\right]}{dt} = \left\{k_D\left[donor\right]\varphi + k_{GO}\left[GO\right]\right\}\cdot\left[P_{700}^{+\bullet}\right] - k_{PSI}\left(\left[P_{700}\right]_{t\alpha} - \left[P_{700}^{+\bullet}\right]\right) \quad \text{(Eq. 3.11)}$$

The solution of equation (3.11) provides the description of the concentration of $P_{700}^{+\bullet}$ at time t in the light phase, where light-induced oxidation of P_{700} is opposed by simultaneous re-reduction by the chemical donor and GO:

$$\left[P_{700}^{+\bullet}\right]_t = \frac{k_{PSI}\left[PSI\right]}{k_{PSI} + k_D\cdot\left[donor\right]\varphi + k_{GO}\left[GO\right]}\left(1 - e^{-\left\{k_{PSI} + k_D\cdot\left[donor\right]\varphi + k_{GO}\left[GO\right]\right\}t}\right) \quad \text{(Eq. 3.12)}$$

This equation holds true if $\left[P_{700}^{+\bullet}\right]_0 = 0$.

3.3 - Kinetic Model: PSII-GO-NiNTA-PSI System

When PSII CCs His-tagged on the stromal side and PSI CCs His-tagged on the luminal side are co-immobilized on the surface of GO the construct PSII-(GO-NiNTA)-PSI is assembled. This system represents the first example of a biohybrid electron transport chain based on GO. As most electron transport chains *in vivo* it requires the assistance of suitable redox mediators. Ferricyanide $Fe(CN)^{3-}$ and DCBQ are the mediators for PSII and represent a substitute for the natural plastoquinone pool. DCPIP and acsorbate are the mediators targeting the donor side of PSI (the plastocyanine side), while MV is the mediator deputed to accept electrons from the acceptor side of PSI. It is expected that there could be up to 10^{10} of PSII-(GO-NiNTA)-PSI constructs per mL of suspension. A more precise formula would be $(PSII)_n$-(GO-NiNTA)-$(PSI)_m$, because tens of thousands of PSII and PSI CCs can assemble on both sides of a GO-NiNTA fragment with about 5 μm in diameter, where n:m would be the molar ratio of PSII to PSI.

The kinetic description of PSII-(GO-NiNTA)-PSI requires the semi-reactions shown in scheme 3.1, III. The forward light-driven semi-reaction is the oxidation of P_{700} to $P_{700}^{+\bullet}$. The re-reduction from $P_{700}^{+\bullet}$ to P_{700} can occur via chemical donor (DCPIP and acsorbate) or by electron-transfer from GO. GO in turn can receive electrons form the light-driven semi-reaction from P_{680} to $P_{680}^{+\bullet}$. The differential equations that are needed to describe this system are (Eq. 3.1) and (Eq. 3.13):

$$-\frac{d\left[P_{700}^{+\bullet}\right]}{dt} = \left\{k_D\left[donor\right]\varphi + k_{PSII}\left[P_{680}\right] + k_{GO}\left[GO\right]\right\}\cdot\left[P_{700}^{+\bullet}\right] \qquad \text{(Eq. 3.13)}$$

The s.s. condition is realized when (Eq. 3.1) and (Eq. 3.13) are equal:

$$k_{PSI}\left[P_{700}\right]_{s.s.} = \left\{k_D\left[donor\right]\varphi + k_{PSII}\left[P_{680}\right] + k_{GO}\left[GO\right]\right\}\cdot\left[P_{700}^{+\bullet}\right]_{s.s.} \qquad \text{(Eq. 3.14a)}$$

Rearrangement of equation (Eq. 3.14a) leads to equation (Eq. 3.14b):

$$\frac{\left[P_{700}^{+\bullet}\right]_{s.s.}}{\left[P_{700}\right]_{s.s.}} = \frac{k_{PSI}}{k_D\left[donor\right]\varphi + k_{PSII}\left[P_{680}\right] + k_{GO}\left[GO\right]} \qquad \text{(Eq. 3.14b)}$$

The solution of equation (Eq. 3.13), deprived of the term $k_{PSII}\left[P_{680}\right]$ which is not active without light, provides an expression for the concentration of $P_{700}^{+\bullet}$ at time t in the dark phase:

$$\left[P_{700}^{+\bullet}\right]_t = \left[P_{700}^{+\bullet}\right]_{sat} \cdot e^{-\left\{k_D\left[donor\right]\varphi + k_{GO}\left[GO\right]\right\}\cdot t} \qquad \text{(Eq. 3.15)}$$

Equation (Eq. 3.15) is exactly the same as equation (Eq. 3.10).

Combining equations (Eq. 3.1) and (Eq. 3.13), considering the boundary condition (Eq. 3.4) leads to:

$$-\frac{d\left[P_{700}^{+\bullet}\right]}{dt} = \left\{k_D\left[donor\right]\varphi + k_{PSII}\left[P_{680}\right] + k_{GO}\left[GO\right]\right\}\cdot\left[P_{700}^{+\bullet}\right] - k_{PSI}\left(\left[P_{700}\right]_{tot} - \left[P_{700}^{+\bullet}\right]\right) \qquad \text{(Eq. 3.16)}$$

Solving equation (Eq. 3.16) generates equation (Eq. 3.17) describing the time evolution of the concentration of $P_{700}^{+\bullet}$ in the light phase, where light-induced oxidation of P_{700} is contrasted by simultaneous re-reduction by the chemical donor and GO. In turn, PSII immobilized onto GO, reduces GO in the presence of light. Therefore:

$$\left[P_{700}^{+\bullet}\right]_t = \frac{k_{PSI}\left[PSI\right]}{k_{PSI} + k_D\cdot\left[donor\right]\varphi + k_{PSII}\left[P_{680}\right] + k_{GO}\left[GO\right]}\left(1 - e^{-\left\{k_{PSI} + k_D\cdot\left[donor\right]\varphi + k_{PSII}\left[P_{680}\right] + k_{GO}\left[GO\right]\right\}t}\right) \qquad \text{(Eq. 3.17)}$$

This equation holds true if $\left[P_{700}^{+\bullet}\right]_0 = 0$.

3.4 – Kinetic Model: Summary of Equations and Measurable Parameters Derived from the Kinetic Model

The kinetic model elucidated above for PSI, GO-NiNTA-PSI, and PSII-(GO-NiNTA)-PSI can be summarized in the equations included in Scheme 3.2. These equations can be used to fit JTS data in order to measure the rates in the light and dark phases, as summarized in Table 3.1. The inspection of Table 3.1 indicates that the oxidation rates in the light phase become increasingly more complex through the addition of new terms accounting for the presence of GO and PSII in a predictable and intuitive fashion. The re-reduction rates in the dark are determined by the chemical donor and by GO, when present. As expected, PSII does not affect the re-reduction rate in the dark phase.

Scheme 3.2 - Kinetic equations

$$\left[P_{700}^{+\bullet}\right]_t = \left[P_{700}^{+\bullet}\right]_{sat} \cdot e^{-k_D[donor]t} \quad \textbf{Dark phase}$$

$$\left[P_{700}^{+\bullet}\right]_t = \frac{k_{PSI}[PSI]}{k_{PSI} + k_D \cdot [DCPIP]}\left(1 - e^{-\{k_{PSI} + k_D \cdot [DCPIP]\}t}\right) \quad \textbf{Light phase} \qquad \textbf{(I)}$$

$$\left[P_{700}^{+\bullet}\right]_t = \left[P_{700}^{+\bullet}\right]_{sat} \cdot e^{-\{k_D[DCPIP]\varphi + k_{GO}[GO_{red}]\}\cdot t} \quad \textbf{Dark phase}$$

$$\left[P_{700}^{+\bullet}\right]_t = \frac{k_{PSI}[PSI]}{k_{PSI} + k_D \cdot [DCPIP]\varphi + k_{GO}[GO_{red}]}\left(1 - e^{-\{k_{PSI} + k_D \cdot [DCPIP]\varphi + k_{GO}[GO_{red}]\}t}\right) \quad \textbf{Light phase} \qquad \textbf{(II)}$$

$$\left[P_{700}^{+\bullet}\right]_t = \left[P_{700}^{+\bullet}\right]_{sat} \cdot e^{-\{k_D[DCPIP]\varphi + k_{GO}[GO_{red}]\}\cdot t} \quad \textbf{Dark phase (no PSII)}$$

$$\left[P_{700}^{+\bullet}\right]_t = \frac{k_{PSI}[PSI]}{k_{PSI} + k_D \cdot [DCPIP]\varphi + k_{PSII}[P_{680}] + k_{GO}[GO_{red}]}\left(1 - e^{-\{k_{PSI} + k_D \cdot [DCPIP]\varphi + k_{PSII}[P_{680}] + k_{GO}[GO_{red}]\}\cdot t}\right) \quad \textbf{Light phase} \qquad \textbf{(III)}$$

Scheme 3.2. | Kinetic equations relevant to PSI alone (I), PSI on GO-NiNTA (II), and the PSII-(GO-NiNTA)-PSI biohybryd electron

Table 3.1. Measurable rates in the light and dark phases for free PSI in suspension as opposed to PSI on GO, with or without PSII.

Sample	**Light Phase**	**Dark Phase**
	Oxidation	Re-reduction
PSI CCs	$k_{PSI} + k_D \cdot [donor]$	$k_D^{'} \cdot [donor]$
GO-NiNTA-PSI	$k_{PSI} + k_D \cdot [donor]\ \varphi + k_{GO}[GO]$	$k_D^{'} \cdot [donor]\ \varphi + k_{GO}^{'}[GO]$
PSII-(GO-NiNTA)-PSI	$k_{PSI} + k_D \cdot [donor]\ \varphi + k_{PSII}[P_{680}] + k_{GO}[GO]$	$k_D^{'} \cdot [donor]\ \varphi + k_{GO}^{'}[GO]$

The prime (') indicates the constants measured in the dark phase.

The steady state parameters that can be extracted from JTS data in the light phase are summarized in Table 3.1. Both the steady state ratio and the steady state concentration of oxidized PSI are described by expressions whose complexity increases incrementally by addition of new terms. These new terms reflect the additive contribution of GO and PSII. The factor φ accounts for the sterical accessibility of the chemical donor to the acceptor side of PSI when GO is present.

Figure 3.3 - A biohybrid electron transport chain

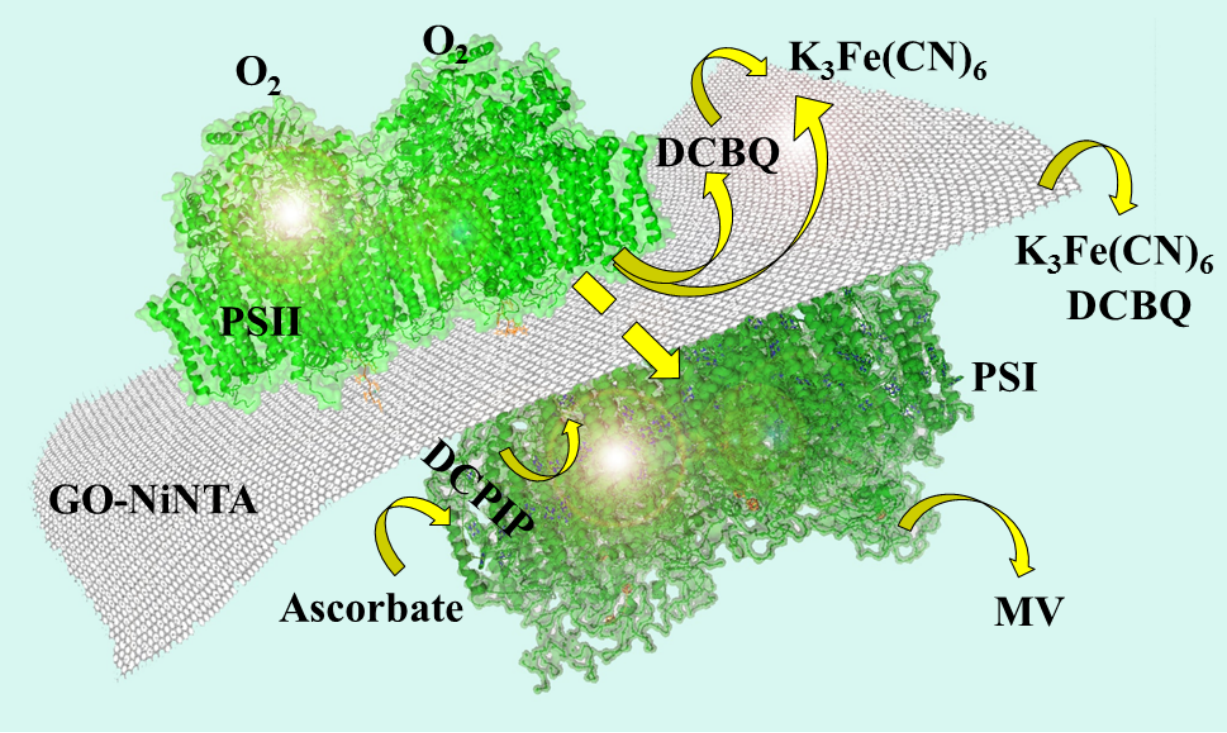

Figure 3.3 | A biohybrid electron transport chain based on PSII, PSI, and GO-NiNTA: PSII-(GO-NiNTA)-PSI. The yellow arrows indicate possible pathways of electronic flow. The redox mediators are also indicated.

Table 3.2 Measurable steady state parameters in the light phase for free PSI in suspension as opposed to PSI on GO, with or without PSII.

Sample	**Steady State Ratio** $\left[P_{700}^{+\bullet}\right]_{s.s} \Big/ \left[P_{700}\right]_{s.s}$	**Steady State Concentration** $\left[P_{700}^{+\bullet}\right]_{s.s}$
PSI CCs	$\frac{\left[P_{700}^{+\bullet}\right]_{s.s}}{\left[P_{700}\right]_{s.s}} = \frac{k_{PSI}}{k_D[donor]}$	$\left[P_{700}^{+\bullet}\right]_{s.s.} = \frac{k_{PSI}[PSI]}{k_{PSI} + k_D \cdot [donor]}$
GO-NiNTA-PSI	$\frac{\left[P_{700}^{+\bullet}\right]_{s.s.}}{\left[P_{700}\right]_{s.s.}} = \frac{k_{PSI}}{k_D[donor]\ \varphi + k_{GO}[GO]}$	$\left[P_{700}^{+\bullet}\right]_{s.s.} = \frac{k_{PSI}[PSI]}{k_{PSI} + k_D \cdot [donor]\ \varphi + k_{GO}[GO]}$
PSII-(GO-NiNTA)-PSI	$\frac{\left[P_{700}^{+\bullet}\right]_{s.s.}}{\left[P_{700}\right]_{s.s.}} = \frac{k_{PSI}}{k_D[donor]\ \varphi + k_{PSII}[P_{680}] + k_{GO}[GO]}$	$\left[P_{700}^{+\bullet}\right]_{s.s.} = \frac{k_{PSI}[PSI]}{k_{PSI} + k_D \cdot [donor]\ \varphi + k_{PSII}[P_{680}] + k_{GO}[GO]}$

3.4 - Decoupling Experiment Analysis

The PSII-(GO-NiNTA)-PSI system in suspension is illustrated in Fig. 3.3. In this system DCBQ and $K_3Fe(CN)_6$ are the redox mediators intended to accept electrons from the acceptor side of PSII. On the donor side of PSII water oxidation occurs with oxygen evolution catalyzed by the water oxidizing complex. Effectively these two mediators substitute for the natural plastoquinone pool. The same mediators can accept electrons directly from GO-NiNTA. GO-NiNTA represents an equipotential surface at the same potential as the acceptor side of PSII. DCPIP and ascorbate are the redox mediators, which assure that PSI is readily reduced as soon as it is oxidized by light ($P_{700} >> P_{700}^{+\bullet}$). MV is the terminal electron acceptor and is intended to receive electrons from the acceptor side of PSI.

PSII and PSI can be disassembled from PSII-(GO-NiNTA)-PSI giving back PSII, PSI, and GO-NiNTA (Fig. 3.4). Imidazole in relatively high concentration can detach the His-tagged CCs from the NiNTA groups. The basic assumption of this experiment is that decoupled PSII and PSI will behave like free PSII and PSI in suspension.

The JTS spectra of such an experiment are shown in Fig. 3.5. The quality of the experiment is excellent as indicated by the fitting with exponential functions with the following general form:

$$y(t) = y_0 + A \cdot e^{-invtau \cdot t} \qquad \text{(Eq. 3.18)}$$

The summary of the fitting parameters is given in Table 3.3.

Figure 3.4 - Decoupling of PSII-(GO-NiNTA)-PSI

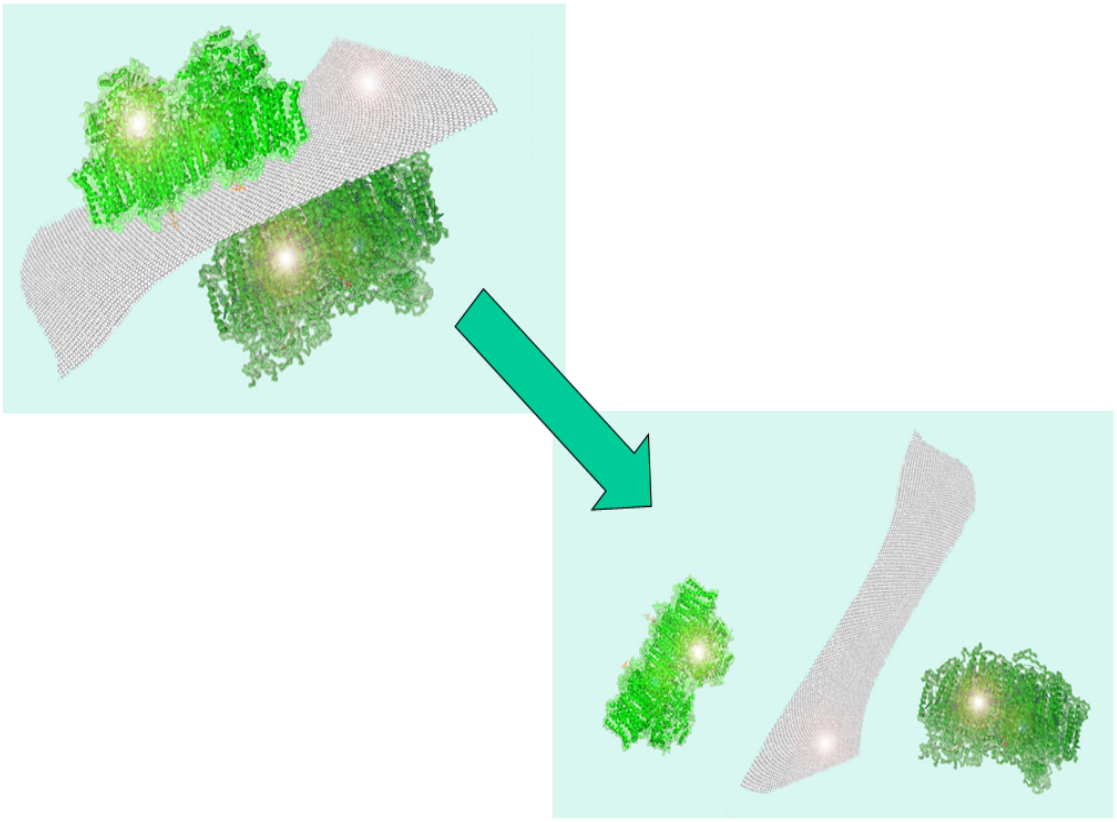

Figure 3.4 | Decoupling of PSII-(GO-NiNTA)-PSI into PSII, PSI, and GO-NiNTA. This result is achieved by adding to the suspension imidazole as a competitive ligand with respect to the NiNTA functional groups.

Figure 3.5 – JTS Measurements

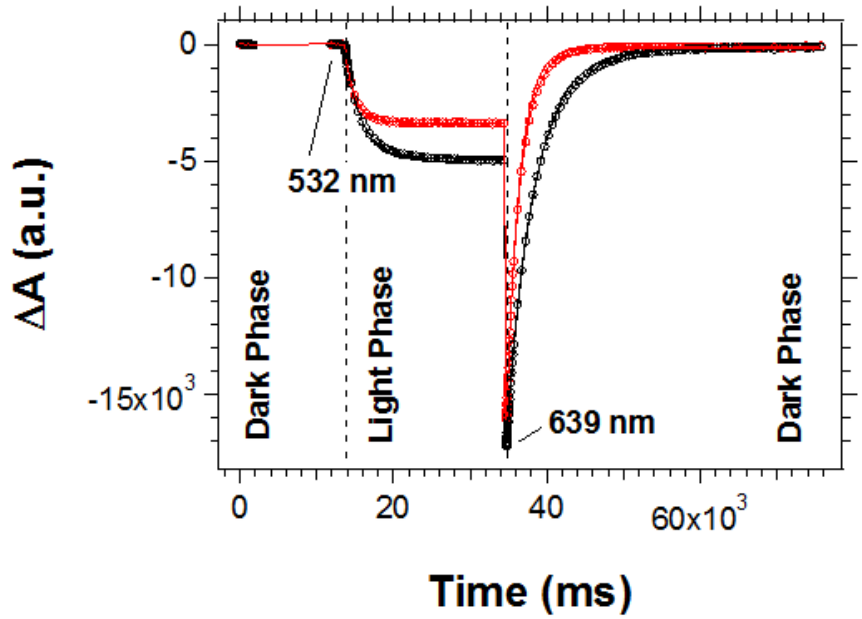

Figure 3.5 | JTS measurements of PSII-(GO-NiNTA)-PSI (20%-oxygen GO) in the same sample before (black profile) and after (red profile) treatment with imidazole. Measurements are conducted in absorbance change mode to specifically probe PSI.

On the basis of these fitting results it was possible to confirm the parameters shown in Table 3.3. The fittings of the data are expected to be more accurate in the light than in the dark, and given the sensitivity of PSII even to the probing light in the dark phase. For this reason instead of using equations 3.3 and 3.6, it is preferred to use equation 3.7, which is derived taking the ratio of equations 3.6 and 3.3. Therefore, equations 3.1, 3.2, 3.4, 3.5, and 3.7 constitute a system of equations that can be solved.

Table 3.3. Parameters used in the fitting of the light and dark phases

Sample	**Light Phase**	**Dark Phase**
	Oxidation	Re-reduction
Coupled **PSII-(GO-NiNTA)-PSI**	$y_0 = -4903.3 \pm 12.9$	$y_0 = -217.06 \pm 14.8$
	$A = 3.4823 \cdot 10^6 \pm 3.73 \cdot 10^5$	$A = -16839 \pm 26.3$
	$invtau = 0.00048193 \pm 7.82 \cdot 10^{-6}$	$invtau = 0.00028311 \pm 1.66 \cdot 10^{-6}$
Uncoupled **PSII, GO-NiNTA, PSI**	$y_0 = -3349.4 \pm 6.89$	$y_0 = -147.19 \pm 8.51$
	$A = 3.4725 \cdot 10^8 \pm 6.18 \cdot 10^7$	$A = -15860 \pm 18.2$
	$invtau = 0.00084556 \pm 1.29 \cdot 10^{-5}$	$invtau = 0.00056559 \pm 2.68 \cdot 10^{-6}$

Table 3.3 | Parameters used in the fitting of the light and dark phases of PSII-(GO-NiNTA)-PSI before and after decoupling with imidazole. A single exponential function was considered (see equation 3.18).

Table 3.4. The rate values determined from the exponential fitting of the light and dark profiles in Fig 3.5

Sample		Equations	Phase
Coupled: PSII-(GO-NiNTA)-PSI	**3.1**	$k_{PSI} + k_D \cdot [donor]\ \varphi + k_{PSII}[P_{680}] + k_{GO}[GO] = 0.00048193$	light, oxidation
	3.2	$\frac{k_{PSI}}{k_D[donor]\ \varphi + k_{PSII}[P_{680}] + k_{GO}[GO]} = 0.39810$	light, steady state ratio
	3.3	$k_D^{'} \cdot [donor]\ \varphi + k_{GO}^{'}[GO] = 0.00028311$	dark, re-reduction
Uncoupled: PSII, GO-NiNTA, PSI	**3.4**	$k_{PSI} + k_D \cdot [donor] = 0.00084556$	light, oxidation
	3.5	$\frac{k_{PSI}}{k_D[donor]} = 0.26225$	light, steady state ratio
	3.6	$k_D^{'} \cdot [donor] = 0.00056559$	dark, re-reduction
Both	**3.7**	$\frac{k_D^{'} \cdot [donor]}{k_D^{'} \cdot [donor]\ \varphi + k_{GO}^{'}[GO]} = 1.9978$	dark, re-reduction

Table 3.4 | Equation 3.7 is obtained by taking the ratio of equations 3.6 and 3.3, which were obtained in the dark phase.

The solution of the system of these equations is shown in Table 3.5. It can be seen that the tern $k_D[donor]$ is the dominant term. The most important result is represented by the fact that the term $k_{PSII}[P_{680}]$ represents 16% of the dominant term. This contribution clearly indicates that PSII CCs participate in the direct or rapidly mediated re-reduction of P_{700} to $P_{700}^{+\bullet}$. This information helps us to deduce the map of the electronic flows through the biohybrid electron chain represented by PSII-(GO-NiNTA)-PSI and its redox mediators. A schematic representation of these electronic pathways is given in Fig. 3.6. As it can be inferred from this diagram the contribution of 16% is even more relevant if we consider the effect of φ which diminishes the impact of the term $k_D[donor]$. Therefore it can be deduced that $k_{PSII}[P_{680}]$ is very close in size to the corrected term $k_D[donor]\cdot\varphi$ when φ = 0.1. If φ = 0.5 we can expect the maximum impact of the term $k_D[donor]\cdot\varphi$ (see Fig. 3.7). In this case it is expected that all of the re-reduction of PSI is caused by the chemical donor and this should annihilate the contribution of reduced GO. Reduced GO is rapidly discharged to the DCBQ and ferricyanide pool. Except this unique extreme case, in all other cases (0≤φ<0.5) PSII is expected to contribute to the re-reduction of PSI.

There is further JTS evidence in support of these results. This spectroscopic technique allowed us to probe not only PSI but also PSII. The variable fluorescence of PSII increases after decoupling, indicating that PSII rapidly transfers electrons to GO when attached to it (Fig. 3.8). The quantum yield of photochemistry F_V/F_m is higher after decoupling. These values are relatively low due to the use of Ficoll as suspension stabilizer in the sample, but consistent with the proposed interpretation. The lower F_V/F_m before decoupling indicates that GO provides a fast pathway for releasing electrons from PSII. It should be noted also that the same PSII in aqueous solution had an F_v/F_m of 0.60.

Table 3.5. Solution of the system of equations 3.1, 3.2, 3.4, 3.5, and 3.7, selected from those in Table 3.4.

Term	Percentage of $k_D[donor]$
$k_D[donor] = 0.00066988 \quad 1/s$	100%
$k_{PSI} = 0.00017568 \quad 1/s$	26%
$k_{PSII}[P_{680}] = 0.00010599 \quad 1/s$	16%
$k_{GO}[GO] = 0.00033531 - 0.00066988 \cdot \varphi \quad 1/s$	if φ = 0.00, 50%
	if φ = 0.10, 40%
	if φ = 0.50, 0%

The results are expressed as percentage of the dominant term $k_D[donor]$, not hindered by the steric factor φ.

Figure 3.6 - Semi-quantitative estimate

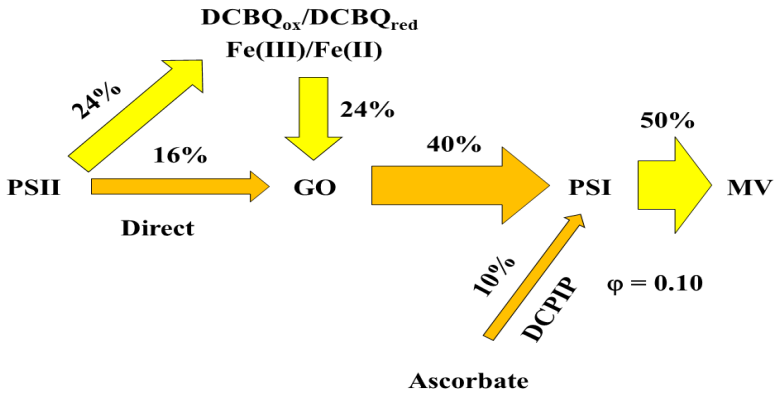

Figure 3.6 | Semi-quantitative estimate of the electronic pathways across the PSII-(GO-NiNTA)-PSI biohybrid electron transport chain determined from JTS data for φ = 0.10. In orange are the flows calculated from the data using the kinetic model, in yellow, deduced by inspection of the overall scheme.

Figure 3.7 - Semi-quantitative estimate

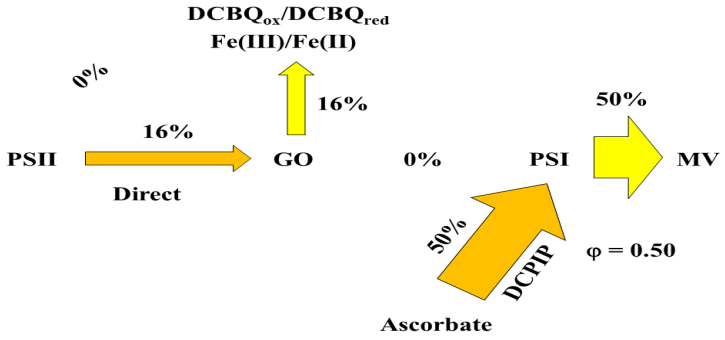

Figure 3.7 | Semi-quantitative estimate of the electronic pathways across the PSII-(GO-NiNTA)-PSI biohybrid electron transport chain determined from JTS data for φ = 0.50. In orange are the flows calculated from the data using the kinetic model, in yellow flows deduced by inspection of the overall scheme.

Figure 3.8 - Variable fluorescence measurements of PSII-(GO-NiNTA)-PSI

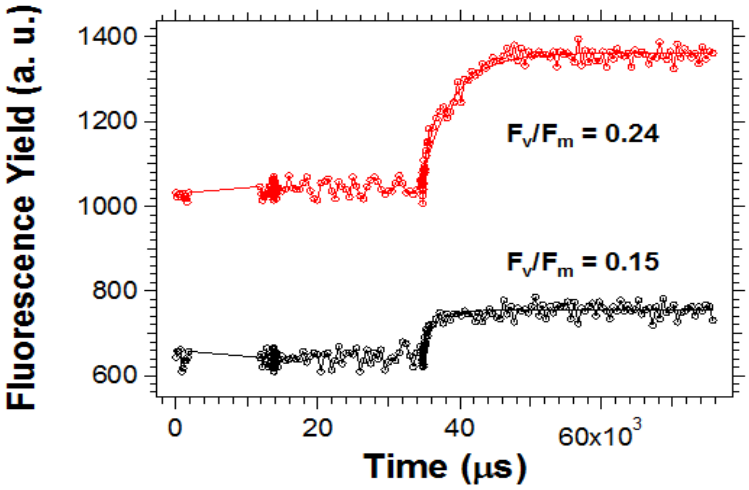

Fig. 3.8 | Variable fluorescence measurements of PSII-(GO-NiNTA)-PSI (20%-oxygen GO) in the same sample before (black profile) and after (red profile) treatment with imidazole.

4. Conclusions

These results demonstrate that PSII-(GO-NiNTA)-PSI system functions like a biohybryd electron transport chain. Using Joliot-type Spectroscopy (JTS), we were able to demonstrate that PSII participates in the re-reduction when both PSI and PSII are coupled to GO. We were able to probe independently the redox activity of PSI and the fluorescence kinetics of PSII. A kinetic model of the system that proved crucial for interpretation of the data is presented. This model allowed us to quantify the percentage contribution of PSII to the electronic flow to PSI *via* GO, for a specific PSII/PSI ratio (1.9). The steric parameter φ is important to assess the accessibility of the acceptor side of PSI by the chemical donor and the impact of PSII on the overall system.

Chapter IV. Functional Interfacing of *Rhodospirillum rubrum* Chromatophores to a Conducting Support for Capture and Conversion of Solar Energy

This chapter was previously published in The Journal of Physical Chemistry B Volume **117** Issue 38 , pages 11249-11259, 2013.

1. Introduction

The light reactions of oxygenic photosynthesis are initiated by a photon-driven charge separation process catalyzed by photochemical reaction centers (RCs), resulting in the generation of chemical bonds in the form of reduced pyridine nucleotides and ATP. [134] In the anoxygenic chlorophototrophic purple nonsulfur bacteria, such as *Rsp. rubrum*, light energy is converted to chemical potential by way of a type-II RC, organized within the intracytoplasmic membrane (ICM) as a core structure completely surrounded by the light harvesting 1 (LH1) antenna complex. [135, 136] In addition to absorbing blue–green light via the carotenoid spirilloxanthin, the LH1 protein is capable of collecting near-IR photons (maximally at 880 nm) and funneling their excitation energy to the RC bacteriochlorophyll (BChl) special pair for transduction into a transmembrane charge separation with a quantum yield near unity.[137] Figure 4.1 shows how this initiates a cycle of electron-transfer reactions between the primary iron–quinone acceptor (Q_A), the ubiquinol–cytochrome c_2 oxidoreductase (cytochrome bc_1 complex), cytochrome c_2, and the photooxidized RC–BChl special pair, resulting in the formation of an electrochemical proton gradient, coupled to the synthesis of ATP by an F_1F_O-ATP synthase. Together with reduced organic compounds as an electron-donor source, this cyclic electron flow process allows the RC to move electrons and undergo rereduction without the necessity of an oxygen-evolving complex oxidizing water, as in the PSII complex, which houses the type-II RC of oxygenic phototrophs. [134]

The biologically mediated electron-transfer events in purple bacteria were demonstrated to be capable of generating a current in a biohybrid photovoltaic device by Jantzen and Seibert, [138] who attached *Rhodobacter sphaeroides* RCs directly to a SnO_2 electrode. In the studies of Katz and associates, [139, 140] a photoinduced charge separation was demonstrated with UQ-depleted *Rha. sphaeroides* RCs immobilized on a PtO electrode surface modified with covalently bound quinonoid in the presence of reduced cytochrome *c* as the electron donor. [140] Current generation was enhanced when UQ_{10} was added as a diffusionally mobile mediator of electron flow between the RC surface and the electrode, driven by 860 nm illumination absorbed by the RC–BChl special pair. In addition, RC monolayers were covalently immobilized on a carbon electrode surface via the activation of a thiol-binding bifunctional reagent, resulting in oriented RC attachment. [139] The limited separation between RC quinone sites and the electrode surface provided efficient nondiffusional electron flow, eliminating the need for soluble electron-transfer mediators, thereby demonstrating the importance of spatial and diffusional considerations in the design of efficient biohybrid photoelectrochemical devices.

Subsequent work has further established the bacterial RC as an ideal model system for improvements in the design of biohybrid photoelectrochemical devices, and a number of RC immobilization strategies for enhanced photocurrent generation have been developed.[141] These have included the orientated binding of His-tagged RCs on gold using Ni-nitrilotriacetic (Ni-NTA) self-assembled monolayers. [69, 70, 142] With the primary donor oriented toward the substrate, a unidirectional, light-induced cathodic photocurrent was generated in the presence of UQ_{10}, with electron transfer between the gold electrode and the RC occurring by an apparent tunneling mechanism. [70] Photocurrent generation was improved in the presence of cytochrome *c* through formation of a RC–cytochrome *c* complex. [69] The efficiency of such biohybrid photoelectrochemical devices was improved by encapsulating stabilized RCs inside of electrodes

consisting of single-walled carbon nanotube arrays. [143, 144] As an additional strategy for increasing the adsorptive surface area of such biohybrid photoelectrochemical devices,[145] RCs from a thermophilic purple bacterium were adsorbed to folded surface of mesoporous silica. The associated RCs were shown to be stable, specifically bound within the silica pores, and capable of generating a photocurrent on an ITO electrode.

While RCs have provided a highly useful energy conversion system when serving as the biologically based component of biohybid photoelectrochemical devices, increased solar conversion efficiencies are obtained with RC–LH1 core particle, in which the LH1 antenna complex functions at the interface of light harvesting and electron cycling together with providing a markedly increased functional absorption cross section (σ). Nango and collaborators[146, 147] showed that RC–LH1 CCs from purple bacteria could be stably self-assembled as monolayers on appropriately modified electrodes surfaces, which, upon illumination at the LH1 absorption maximum (880 nm), gave rise to efficient energy transfer and photocurrent responses. More recently, His-tagged RC–LH1 CCs, engineered in *Rba. sphaeroides* with defined orientations, were immobilized onto a solid Ni-NTA substrate and shown to give rise to orientation-dependent photocurrents. [148] Such orientation-specific photocurrents were also demonstrated with *Rba. sphaeroides* LH proteins in which Cys residues were inserted by site-directed mutagenesis on each membrane face and attached covalently to conducting gold surfaces. [149] LH functions were improved in comparison to self-assembled monolayers adsorbed onto gold, and superior LH1 photostability was also confirmed.

As a means of enhancing photocurrent generation, RCs were interfaced directly to a bare gold electrode, [150] and the effects played by molecular relays and the inclusion of LH complexes were investigated. Sizeable photocurrents were obtained in comparison with

monolayers that were self-assembled with RCs specifically modified to contain orienting linkers. This was apparently a consequence of the lack of a layer insulating the metal surface from the RC pigments and the minimization of electron tunneling distances. Higher photocurrents were also generated with RC–LH1 CCs, but this was not attributed to the improved photoabsorption rather to an enhanced surface coverage of CCs that were uniformly oriented and contained a tetraheme cytochrome, thought to serve as a connecting wire. Added cytochrome *c* functioned as a molecular relay by intercalating between the adhered RC pigments and the electrode to improve current production. Alterations in the order in which the photocell components were introduced resulted in a dynamic rearrangement of the cytochrome and RCs at the electrode surface.

Magis et al. [43] have described the fabrication of a chromatophore-based biohybid photoelectrochemical device in which ICM vesicles (chromatophores) from *Rba. sphaeroides* were immobilized onto a bare gold electrode surface in the absence of surface functionalization. Confocal fluorescence spectroscopy and light-induced electrochemistry measurements demonstrated that the adsorbed membranes maintain their energy and electron-transferring capabilities. By applying an external potential within the range of the open-circuit potential of the RC and appropriate charge carriers (cytochrome *c* and the quinone Q_0, which lacks an isoprenoid tail), light-induced currents of 10 $\mu A/cm^2$ were generated for several minutes under aerobic conditions and maintained for nearly 3 days under continuous illumination. These electrochemical measurements showed that a current of 300 nA was generated at peak output, dropping off to a minimum of 50 nA over the further duration of the measurements. The LH1 complex showed substantial durability, overcoming the main obstacle for using biological-membrane materials based in biohybrid photoelectrochemical cells or in other technological applications.

In contrast to the robustness demonstrated for the LH1 complex, the *Rba. sphaeroides* LH2 peripheral antenna protein showed a light-intensity-dependent decoupling from photoconversion, with extensive photobleaching under high illumination. [43] Because of this lack of long-term LH2 stability, we have initiated further photoelectrochemical studies with chromatophores from *Rsp. rubrum*, which forms a robust LH1–RC core structure while lacking LH2. Further impetus for the choice of the *Rsp. rubrum* chromatophore preparations was provided by the differences in the functional absorption cross section, obtained from fluorescence induction/ relaxation measurements between these two organisms. [151] Values of 16 $Å^2$ were obtained for *Rsp. rubrum* cells, [151] as compared to ~50 and ~120 $Å^2$, respectively, for *Rba. sphaeroides* cells grown at high light intensity and those acclimating to 48 h of weak illumination in which the LH2/LH1 molar ratio increased by ~1.8-fold. [152] Although a smaller antenna size results in decreases in the amount of light harvested by individual cells, they have an enhanced activity for the charge separation process on a photon basis, owing to decreases in nonproductive light acquisition and an attendant loss of captured excitations as heat or fluorescence. As noted above for *Rba. sphaeroides* chromatophores adsorbed to gold, [43] little advantage was encountered when the functional absorption cross section was expanded by the presence of the LH2 complex.

Consequently, we have adsorbed *Rsp. rubrum* chromatophores to gold electrode surfaces lacking functionalization and obtained views of the surface coverage of the immobilized structures by atomic force microscopy while assessing the retention of functional activities through fluorescence induction/relaxation and chronoamperometric measurements. These functional biohybrid photoelectrochemical cells were compared to devices assembled using *Rba. sphaeroides* chromatophores with increasing LH2 levels. The adsorbed structures showed a continuous surface coverage comprised of flattened *Rsp. rubrum* chromatophore

vesicle patches that had a significant residual quantum yield of photochemistry and the capability of generating sustained photocurrents under both white light and intense 850 nm illumination for a 1 week period.

Figure 4.1 - Schematic depiction of radiant energy conservation in the ICM of *Rsp. Rubrum*

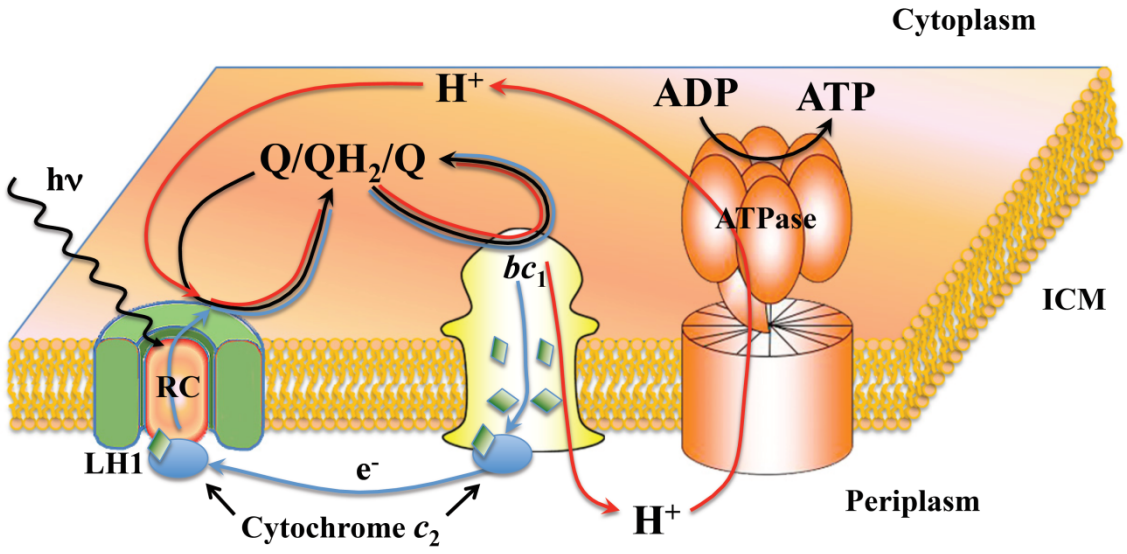

Figure 4.1 | Photon absorption and excitation energy transfer by the LH1 antenna complex (black undulating arrow) drives RC charge separation across the ICM and subsequent electron transport (blue arrows), coupled to proton movement (red arrows), which results in formation of an electrochemical proton gradient providing the energy for the synthesis of ATP by an F_1F_O-ATPase.

2. Experimental Section

2.1 - Bacterial Growth and Chromatophore Isolation

Rba. sphaeroides was grown at a 30 °C in Cohen-Bazire medium [153] under high light conditions (1100 W/m^2) to a maximum OD_{680} of 0.2 to limit cellular self-shading. The cells were switched to a lower light level (100 W/m^2) and incubated for another 24 h, reaching an OD_{680} of 0.7. Because the illumination level is related inversely to the levels of the peripheral LH2 antenna, [154] the cells harvested at 4 and 24 h yielded increased LH2/LH1 molar ratios when compared to the 0 h cells (Table 4.1). *Rsp. rubrum* was grown at 30 °C in Ormerod medium, [194] modified as described in Inamine and Niederman,[155, 156] at low light conditions (100 W/m^2) to an OD_{680} of ~1.0.

Bacterial cells were harvested by centrifugation at 14 000*g* for 10 min at 4 °C, washed at 18 000*g*in 1 mM Tris buffer (pH 7.5), and resuspended to 1.5 mg of wet weight in buffer by homogenization. The *Rba. sphaeroides* chromatophores were isolated as described previously. [157] For isolation of chromatophores from *Rsp. rubrum*, harvested cells were treated for 30 min at 37 °C with lysozyme (1.0 mg/mL), a few crystals of DNAase I and protease inhibitors (Roche) were added, and the cells were disrupted by three passages through a French pressure cell, chilled to 4 °C, at 16 000 lb/in.; [136] all subsequent procedures were also performed at 4 °C. Unbroken cells and cellular debris were removed by centrifugation at 18 000x*g* for 10 min, and the supernatant was layered onto a 5–40% (w/w) sucrose gradient prepared in Tris buffer over a 60% sucrose cushion. After centrifugation for 3 h at 141,000x*g* in an SW 28 rotor, the chromatophore band in the bottom third of the gradient was removed with a Pasteur pipet and placed in an Amicon 100 kDa filter concentrator. During the concentration process, the buffer was exchanged to 20 mM sodium phosphate (pH 7.5).

2.2 - Chromatophore Immobilization

For surface characterization, chromatophores were immobilized on a gold substrates consisting of 10 × 10 mm silicon chips with a 30 nm chromium adhesion layer covered by a 100 nm layer of gold (supplied by Structure Probes, Inc.). The substrate was prepared by hydrogen flaming to form a uniform and nearly atomically flat surface. The chromatophores (0.1 mg of bacteriochlorophyll *a* (BChl)/ml) were incubated on the substrate surface for 1 h in the dark at 0–4 °C.

For chronoampereometric measurements, chromatophores were immobilized by incubation on a polished and rinsed 3 mm round gold electrode (Bio-Logic) at the BChl concentration specified above for 1 h in the dark at 0–4 °C.

2.3 - Visible and Near-IR Absorption Spectroscopy

Absorbance was measured between 450 and 950 nm at a resolution of 1 nm using a Beckman DU-640 spectrophotometer. For *Rba. sphaeroides* chromatophores, LH1/LH2 molar ratios and BChl concentrations were determined by decomposition of near-IR absorption spectra. [44]

2.4 - Atomic Force Microscopy

Electrode surfaces with adsorbed chromatophores were visualized using a MFP-3D-Bio AFM with a Nikon microscope (Asylum Research, Santa Barbara, CA 93117). The measurements were made using the tapping mode in the liquid after the surfaces were dried with a gentle stream of argon. BL-AC40TS cantilevers (Bio Lever Mini), 0.25 N/m, were used in the liquid measurements.

Figure 4.2 - Efficiency of excitation energy transfer from carotenoid to BChl in the *Rsp. rubrum* LH1 complex

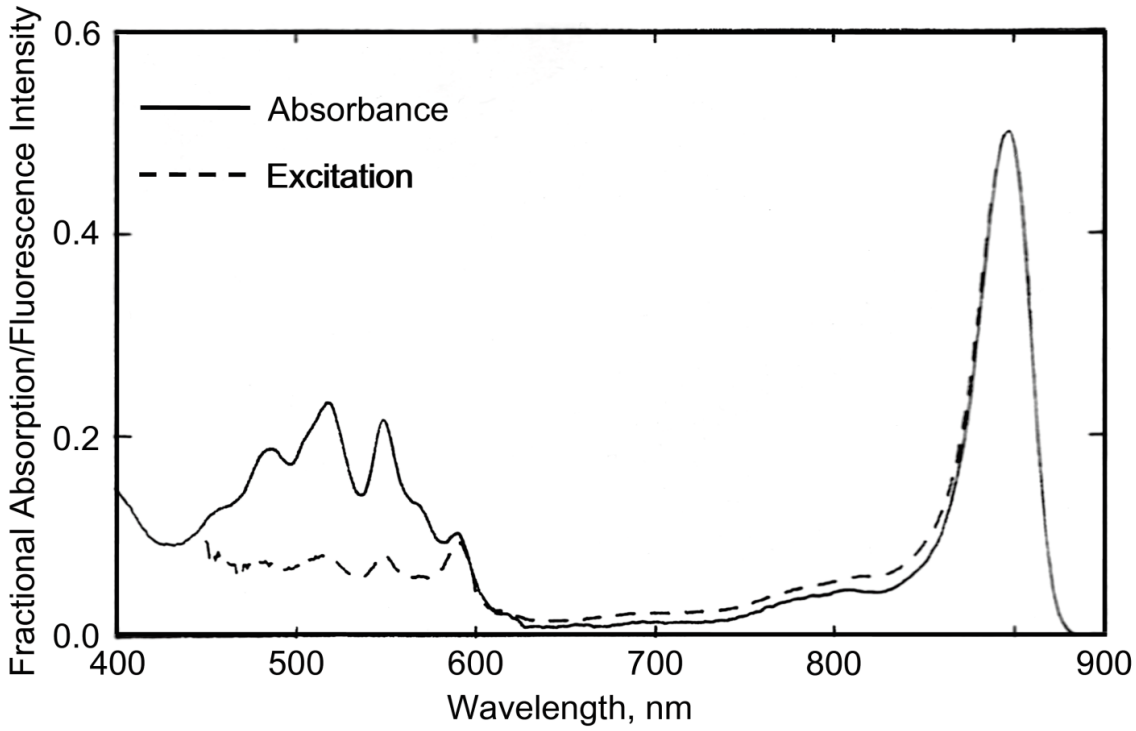

Figure 4.2 | Fractional absorption (1-T) spectra and fluorescence excitation spectra obtained at 77 K were normalized at the Q_Y absorption maximum (897 nm). Efficiencies for excitation energy transfer from spirilloxanthin to both the Q_X and Q_Y bands were ~35-40% as compared to ~36% in chromatophores. Spectra were obtained as described previously [158] using a modified a Johnson Research Foundation DBS-3 spectrophotometer and a DN1704 liquid nitrogen cryostat (Oxford Instruments, Osney Mead, UK).

2.5 - Fluorescence Induction/Relaxation (FIRe) Measurements

A Satlantic FIRe system was used for fluorescence induction/relaxation measurements in which a quartz cuvette and an 880 nm emission filter were used for bulk measurements on appropriately diluted chromatophore samples. Surface measurements were performed by immobilizing a gold substrate bearing the chromatophores on a custom made Delrin insert secured to the cuvette holder. The substrate was oriented at a 45° angle with respect to the vertical axis of the cuvette holder in order to directly face the excitation source. A single turnover flash (STF) of 300 μs was used to saturate the RCs of the *Rba. sphaeroides* and *Rsp. rubrum* preparations. The excitation source consisted of a blue LED (450 nm, 30 nm bandwidth), which in *Rba. sphaeroides* excites LH1- and LH2-bound spheroidene and spheroidenone to the $S_2(1Bu^+)$ state, from which excitation energy is transferred to both the Q_X and Q_Y absorption bands of the LH1 and LH2 BChls. [157] As shown by the excitation spectrum in Figure 4.2, for *Rsp. rubrum*, the 450 nm excitation results in an $S_2(1Bu^+)$ excited state in spirilloxanthin for transfer to LH1 BChl with an efficiency of ~36%. The excitation source is controlled by an LED circuit driver capable of generating pulses of 1 μs to 50 ms duration. The fluorescence emission is detected by a sensitive avalanche photodiode module, and the digitized fluorescence kinetic transients obtained at 880 nm are processed by computer-assisted analysis, which translates the measured signal into several physiological parameters, following the charge separation elicited between the RC–BChl special pair and the primary Q_A. These parameters include the functional absorption cross section (σ), the quantum yield of the primary charge separation (F_v/F_m), and the electron-transfer turnover rates of the RC (τ_1, τ_2, and τ_3), extracted from the multiphasic decay during the fluorescence relaxation. F_v/F_m and σ_{RC} are obtained from the initial rapid induction phase, which is related to the rate of increase in the fluorescence yield.

2.6 - Electrochemical Measurements

Chronoamperometry was performed with a Bio-Logic SP-50 and VSP potentiostat-galvanostats, with EC-Lab version 10 software supplied by the manufacturer. Chromatophores were immobilized on a 3 mm working electrode that was placed into a commercially available cell, with a 23 cm coiled platinum counter electrode (see Figure 4.3 for a schematic representation). The cell was filled with 15 mL of a 20 mM sodium phosphate buffer at pH 7.0 containing 100 mM Q_0 and 20 mM equine heart cytochrome *c*. The system was set to a potential of −0.100 V versus the saturated calomel electrode (SCE). [43] The electrochemical cell temperature was maintained at 25 °C and allowed to come to equilibrium in the dark for 45 min followed by long-term illumination of the immobilized chromatophore samples either under white light or with an 850 nm LED light source at the light intensities indicted in the text.

Figure 4.3 - Schematic depiction of the chronoamperometry measurements.

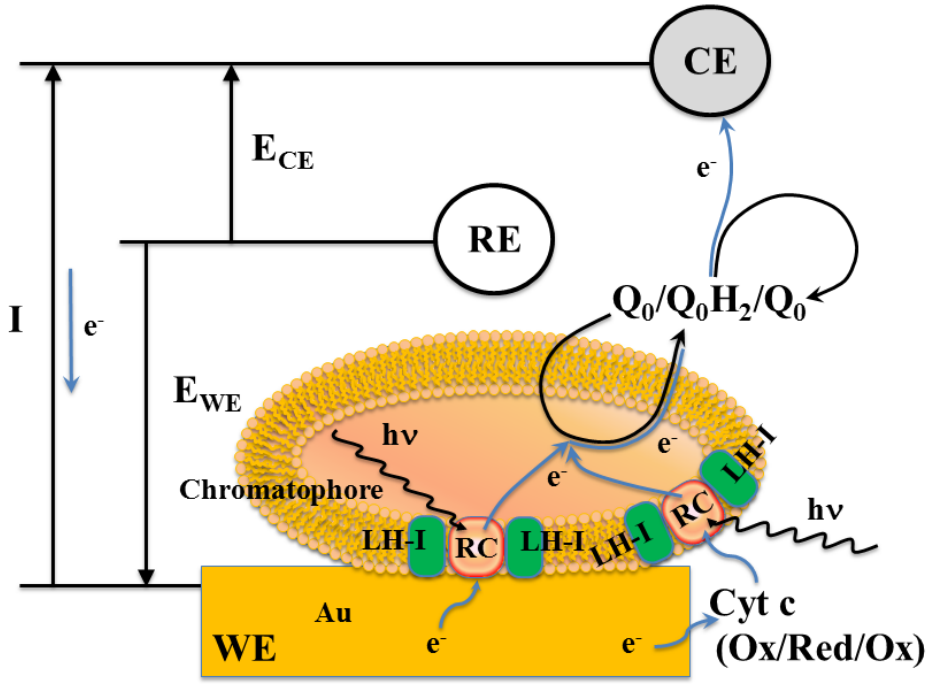

Figure 4.3 | A gold working electrode (WE) with adsorbed chromatophores on the surface was polarized at -0.1 V *vs.* Ag/AgCl, 3 M NaCl as reference electrode (RE), at 25.00 ± 0.01 °C. Illumination occurred under white light conditions or at 850 nm. The electron transfer from WE to the RC in immediate contact with the surface occurs directly. Indirect electron transfer is possible for RCs further away from the surface via horse heart cytochrome *c* (Cyt c). Quinone Q_0 serves as a redox mediator toward the platinum counter electrode (CE). E_{CE} indicates the potential difference between the CE and the RE, while E_{WE} is the potential difference between the WE and RE. *I* indicates the electrical current between the WE and the CE. The measurements were conducted in aqueous buffer.

3. Results and Discussion

3.1 - Absorbance Spectra of Chromatophore Preparations

The electronic absorbance spectra of the *Rba. sphaeroides* chromatophore preparations isolated at various stages after a transfer from high (1100 W/m^2) to low (100 W/m^2) light intensity (Figure 4.4) showed a marked increase in LH2 levels relative to those of the RC–LH1 core structures, confirming the inverse relation between ambient light intensity and LH2 formation in the ICM. [155]. By 4 h after the switch to low light intensity, the dimeric LH2–B850 BChl Q_Y absorption band at 850 nm overtook the 875 nm LH1 Q_Y band, which was the major band under the high-light conditions (LH2/LH1 molar ratios of 0.31 and 0.37 at 0 and 4 h, respectively), ultimately reaching a ratio of 1.00 at 24 h. This overall 3.2-fold increase in LH2 levels resulted in the expansion of the functional absorption cross section to accommodate growth at the reduced light levels. The resulting supramoleclar arrangement [159] assured that excitation energy captured by LH2 was transferred with high efficiency to LH1, ultimately reaching open RC phototraps. Figure 4.4 also shows that *Rsp. rubrum* contains a LH1 complex (absorption maximum at 880 nm) while lacking the LH2 antenna. The RC, identified by the absorbance peak at ~804 nm arising from the monomeric RC–BChl, exists in association with the LH1 antenna to form the photosynthetic unit core, [160] shown below to be capable of remaining viable and robust when exposed to high light intensities.

Figure 4.4 - Visible and near-IR absorbance spectra of the isolated chromatophores

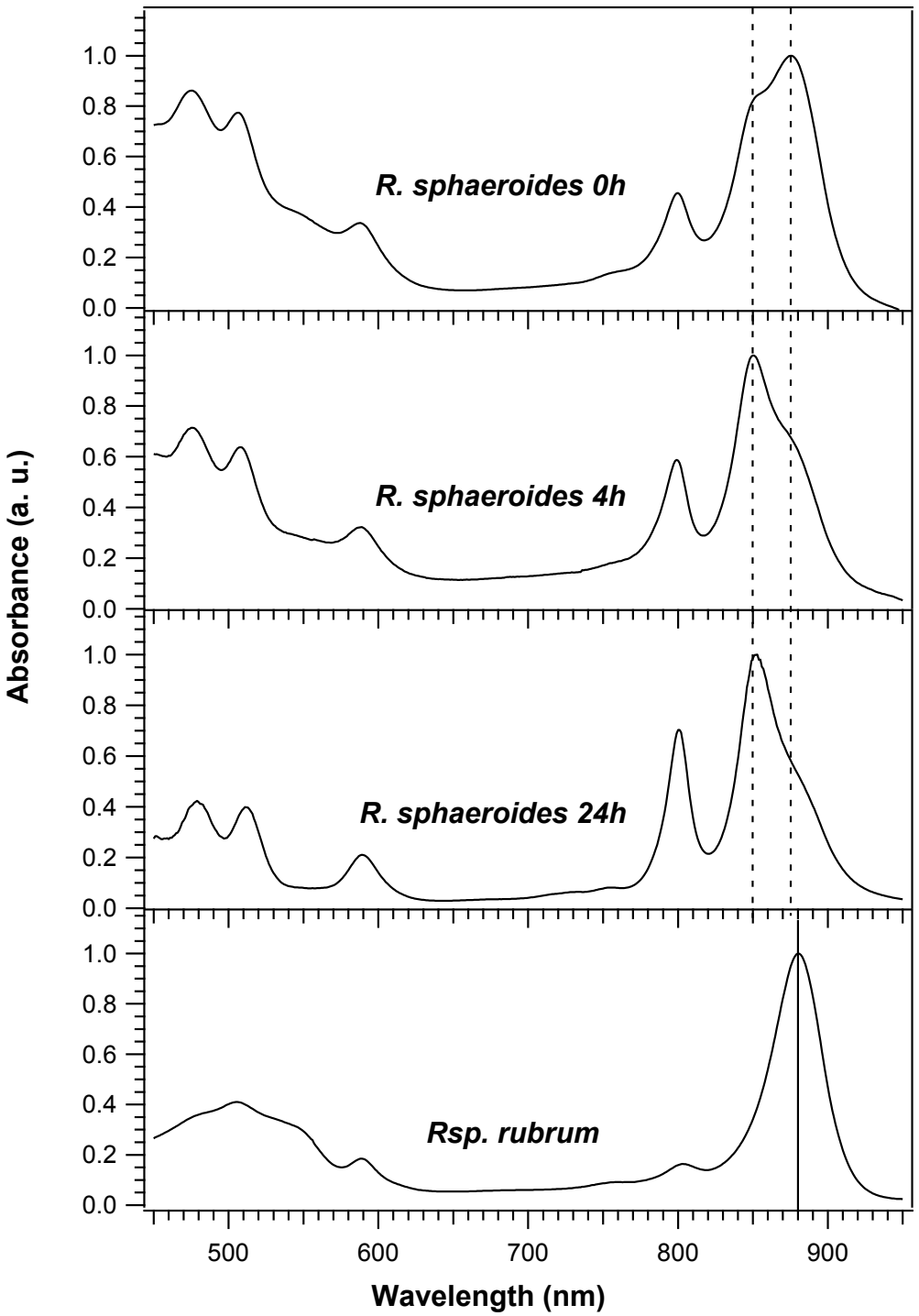

Figure 4.4 | Visible and near-IR absorbance spectra of the isolated chromatophores obtained at room temperature. For the *Rba. sphaeroides* chromatophores, the spectral cross-over corrections and molar extinction coefficients of Sturgis et al [44 149] were used to calculate the molar levels of the LH1 and LH2 complexes in the ICM undergoing remodeling during a down-shift in light intensity. Culture growth conditions: 1,100 W/cm^2 for 24 h; shifted to lower light (100 W/cm^2) and chromatophores were isolated at 0, 4 and 24 h. Note the accelerated appearance of increased LH2 levels during low light growth. The left dotted vertical line shows the Q_Y absorption of LH2 at 850 nm, while dotted vertical line to right shows to the Q_Y absorption of LH1 at 875 nm. [145] In *Rsp. rubrum,* note the redshift of the LH1 Q_Y absorption (continuous vertical line) band to 880 nm and the absence of an LH2 antenna.

3.2 - Atomic Force Microscopy of Chromatophore Preparations Adsorbed to Gold Surfaces

The coverage of chromatophores on the gold substrate surfaces was assessed by atomic force microscopy (AFM). Figure 4.5A shows the extent of coverage of the gold surface with *Rsp. rubrum* chromatophores. The diameter of chromatophores associated with the gold surfaces observed here ranged between ~68.0 and 73.6 nm, with a height of ~46 nm. In contrast, AFM topographs of LH1-enriched *Rba. sphaeroides* preparations showed a more continuous coverage (Figure 4.5B), consisting of chromatophore vesicles of similar diameter and height of ~50 nm. Thus, in both instances, our chromatophores, which represent complete photosynthetic units, have successfully adsorbed to a gold electrode surface that requires only minor conditioning and no chemical modification and have assumed heights consistent with those obtained with *Rba. sphaeroides* chromatophores when deposited onto mica surfaces. [43] These results demonstrate that contact mode AFM can be successfully applied to the characterization of ICM vesicles adsorbed to gold surfaces. Our data indicate that these preparations have apparently retained their vesicular structure rather than giving rise to single-membrane bilayers when adsorbed to gold, as observed by Magis et al. [43]

Figure 4.5 - AFM of chromatophores on gold supports

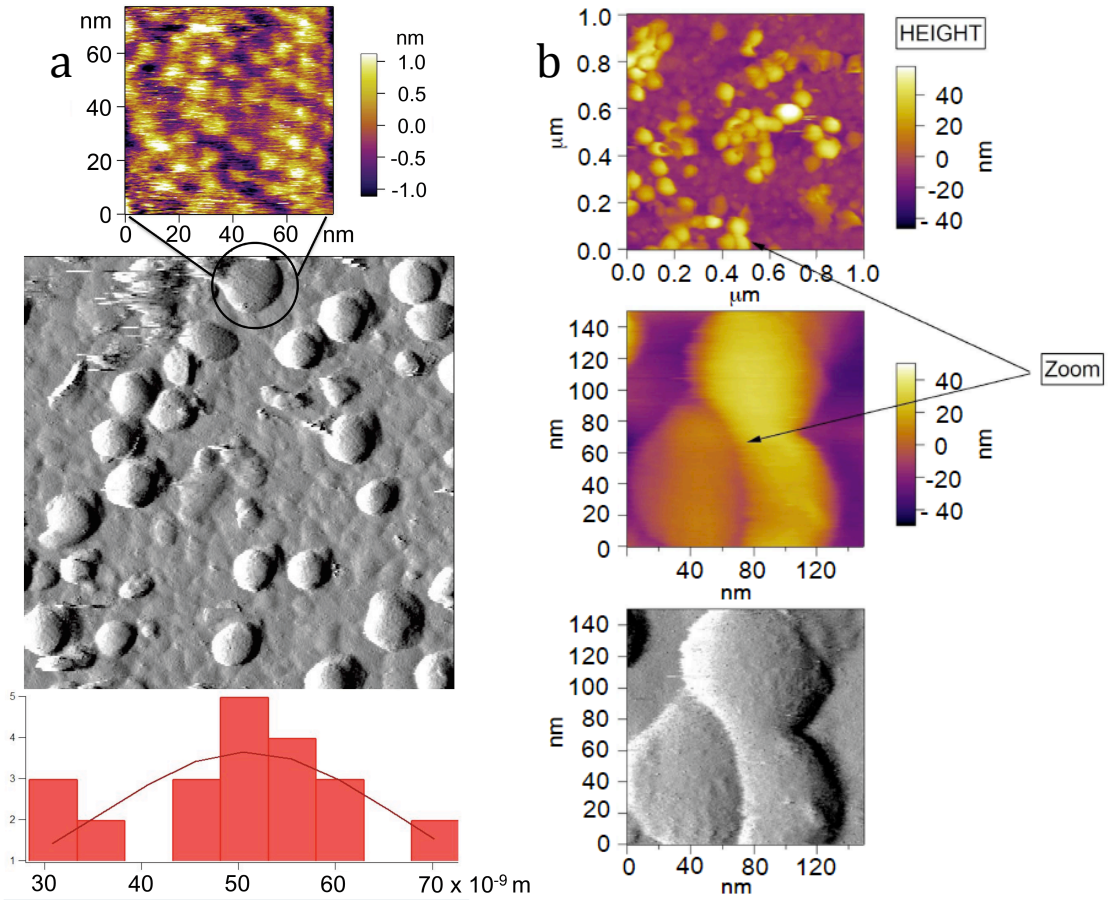

Figure 4.5 | AFM of chromatophores on gold supports. (A) Tapping mode AFM topography image of *Rsp. rubrum* chromatophores. The chromatophores were adsorbed to an Au-Si electrode surface glued to a glass slide with epoxy resin and measurements were made in a liquid medium. Chromatophores (5 μl) were injected into 100 μl of 0.02 mM sodium phosphate buffer and the surface was dried with a gentle stream of argon. The surface was rinsed with 5 mL of deionized water before applying 1 mL of phosphate buffer, followed by100μl of Tris/KCl buffer. A 1.0 x 1.0 μm scanned area is shown with panel at top representing a magnified cytoplasmic surface view showing RC-LH1 core particles with projecting globular surface of RC subunit H at center. *Rsp. rubrum* chromatophore vesicles appear as ellipsoidal structures with an average size of ~68.0-73.6 nm and a height averaging ~50 nm. Vertical false-color scale bars at the right of each panel show tapping mode AFM height and amplitude images. This signal is determined by the error in the AFM feedback loop of cantilever's amplitude and shows fine changes in the features of the topography. Bottom panel shows the results of an analysis of particle height distribution. (B) Tapping mode AFM topography image of a 1.0 x 1.0 μm scanned area containing LH1-enriched *Rba. sphaeroides* chromatophores isolated from cells grown at high light intensity (1100 W/cm^2). The chromatophores were adsorbed to an Au-Si electrode surface as described in panel (a) for imaging in a liquid medium. In middle and bottom panels, three vesicles are magnified to show a higher resolution view of scanned surface.

Because our results are consistent with the retention of a vesicular structure for both *Rsp. rubrum* and LH1-enriched *Rba. sphaeroides* chromatophores upon adsorption to gold, it is more surprising that these preparations, as shown below, have proven to be sufficient for permitting exogenous quinone and cytochrome *c* to conduct the flow of electrons from the chromatophores to and from the electrodes. While the conditions used here for chromatophore immobilization have attracted the cytoplasmic surface of the chromatophore membrane vesicles to the gold surface and are of sufficient strength to survive multiple washings, they do not appear to have disrupted vesicles into open bilayers, as observed by Magis et al. [43] These authors hypothesized that this disruption arises from strong attractive forces between the gold and the vesicular membranes, sufficient to overcome native forces holding the vesicles together. Nevertheless, such forces may result in partial membrane disruption, allowing redox carriers to function according to the scheme shown in Figure 4.3. This would ultimately favor the action of cytochrome *c* in shuttling electrons from the working electrode to the RC. In turn, Q_0 can transfer electrons from RC to the counter electrode surface, once a light-driven charge separation has taken place.

3.3 - Fluorescence Measurements

The variable fluorescence arising from the initial chromatophore suspensions and the chromatophore-modified electrodes was assessed from fluorescence kinetics studies. The results (Figures 4.6 and 4.7) showed that partially functional RCs have been retained in the adsorbed chromatophore preparations and after immobilization on gold surfaces (Tables 4.1-4.4). These measurements were conducted in the presence of horse heart cytochrome *c* alone or cytochrome *c* and Q_0. Cytochrome *c* is expected to play the role of native cytochrome c_2, while Q_0 is a surrogate for native ubiquinone Q (Figure 4.1). The fluorescence induction rates for the initial *Rba. sphaeroides* chromatophore preparations in the presence of cytochrome *c* gave

values for the quantum yield of the primary charge separation (F_v/F_m) of 0.67 for the 0 h sample and respective values of 0.35 and 0.30 for those obtained at 4 and 24 h after the light intensity downshift (Table 4.1). These values compare favorably to the value of 0.70 obtained previously for the chromatophore preparation characterized in Koblízek et. al. [151] When both cytochrome *c* and Q_0 are present the values of F_v/F_m are 0.66, 0.42, and 0.42 for the *Rba. sphaeroides* chromatophores harvested after 0, 4, and 24 h, respectively (Table 4.2). With both redox mediators present, the *Rsp. rubrum* chromatophores have an F_v/F_m value of 0.63. Under these circumstances, the chromatophores in suspension show, in most cases, a higher activity of primary charge separation.

The functional absorption cross section (σ) values were 86.2, 87.7, and 157.4 $Å^2$/q for 0, 4, and 24 h chromatophores, respectively, in the presence of cytochrome *c* only. The same samples resulted in the following values of σ: 80.9, 91.1, and 149.5 $Å^2$/q, respectively, with cytochrome *c* and Q_0. (Table 4.2). Consistent with previous observations, [151] the values of σ increase in the *Rba. sphaeroides* chromatophores with the lowest LH1/LH2 ratio, in which a higher packing density of LH2 rings results in higher values for the functional absorption cross section. *Rsp. rubrum* chromatophores exhibit σ values of 24.0 and 21.0 $Å^2$/q with cytochrome *c* only and cytochrome *c* with Q_0, respectively (Tables 4.1 and 4.2). A small cross section is consistent with the exclusive presence of the LH1 complex as the light-harvesting antenna. The higher values of the connectivity parameter *p* (0.42 and 0.11 with cytochrome *c* only and cytochrome *c* with Q_0, respectively) reflect the closer proximity of the RCs to LH1, the sole LH complex in *Rsp. Rubrum* chromatophores. In the case of *Rba. sphaeroides* chromatophores, the connectivity parameters vary in the intervals of 0.02–0.10 with cytochrome *c* and 0.04–0.05 with cytochrome *c* and Q_0, consistent with a lack of sigmoidicity in the fluorescence rise kinetics.

The fluorescence transients reported in Figure 4.6 are sufficiently resolved to allow a successful fitting of the relaxation profiles after the 300 μs STF with three exponential terms with both types of chromatophores (Figure 4.8) To the best of our knowledge, this is the first time that all three τ values for *Rba. sphaeroides* and *Rsp. rubrum* chromatophores are reported. The τ_1 time constant (1 ms) is attributed to the double reduction of mobile native ubiquinone Q_B (or the substitute Q_0) by the fixed ubiquinone Q_A. The τ_2 time constant (tens of ms) is ascribed to the reduction of ubiquinone Q_B (or Q_0) entering the pocket from the external quinone pool, while τ_3 (hundreds of ms) was attributed to inactive and damaged RC. This assignment reflects the similarity of the RC to PSII CCs.[161] Clearly, when both cytochrome *c* and Q_0 are present, the chromatophores exhibit a higher degree of functional integrity. This observation is reflected by the lower values of τ_3 when cytochrome *c* and Q_0 are available (Table 4.2) as opposed to when only cytochrome *c* is provided (Table 4.1). A smaller portion of inactive and damaged RCs is measured with cytochrome *c* and Q_0 in comparison cytochrome *c* only, as shown by lower values of α_3.

Following adsorption to the gold electrode surface, in the presence of cytochrome *c*, the F_v/F_m values decreased to 0.51, 0.26, and 0.21 for the respective *Rba. sphaeroides* 0, 4, and 24 h samples, representing a ~70% retention of photosynthetic activity (Table 4.3). The *Rsp. rubrum* chromatophore preparation gave an F_v/F_m value of 0.39, as compared the 0.74 observed in whole cells.[151] This F_v/F_m value for the *Rsp. rubrum* chromatophores on gold with cytochrome *c* represents a ~90% retention of photosynthetic activity. Respective values of 0.38, 0.17, and 0.36 were obtained for the 0, 4, and 24 h for *Rba. sphaeroides* when Q_0 was added. Thus, for chromatophores on gold surfaces, the addition of cytochrome *c* and Q_0 showed no obvious effect on the quantum yield of the primary charge separation. We attribute this apparent inconsistency with what was observed in suspension to the substantially different

behavior of the chromatophores on the surface and in suspension. While Q_0 can easily access the Q_B pockets of the RCs in the chromatophores in suspension, the same cannot be expected for the chromatophores on the gold surfaces. The adhesion characteristics of the chromatophores on the surface and the partial disruption of the vesicles caused by interaction with gold will determine their ultimate photosynthetic activity. The lack of active mixing of the film of liquid on the chromatophores is also a factor negatively affecting activity. Despite this, the value of τ_{avg} of the *Rba. sphaeroides* chromatophores on gold appears to be smaller when both cytochrome *c* and Q_0 are present, while no similar effect was observed for *Rsp. rubrum* chromatophores on gold. In the case of the *Rba. sphaeroides* chromatophores, it seems that the functional integrity is enhanced by the presence of Q_0, but this does not consistently result in a higher photosynthetic activity (as reflected by the F_v/F_m).

It is possible to conclude that some loss of photosynthetic activity of chromatophores on the gold electrode surface has arisen from limitations in the supply of accessible chromatophores following adsorption to the gold surface. In chromatophore suspensions, inactive chromatophores can be replaced with active ones by simple dispersion while the immobilized chromatophores are stationary and cannot replace lower-activity vesicles with more active ones. This ensemble effect, which is absent in the immobilized structures, favors the chromatophores that have the largest and most active antenna among those in suspension. Nevertheless, it is shown below that sufficient antenna and RC activity was maintained for production of a significant current at the chromatophore electrode surface.

Figure 4.6 - Fluorescence Kinetics Studies of Chromatophores in Suspension

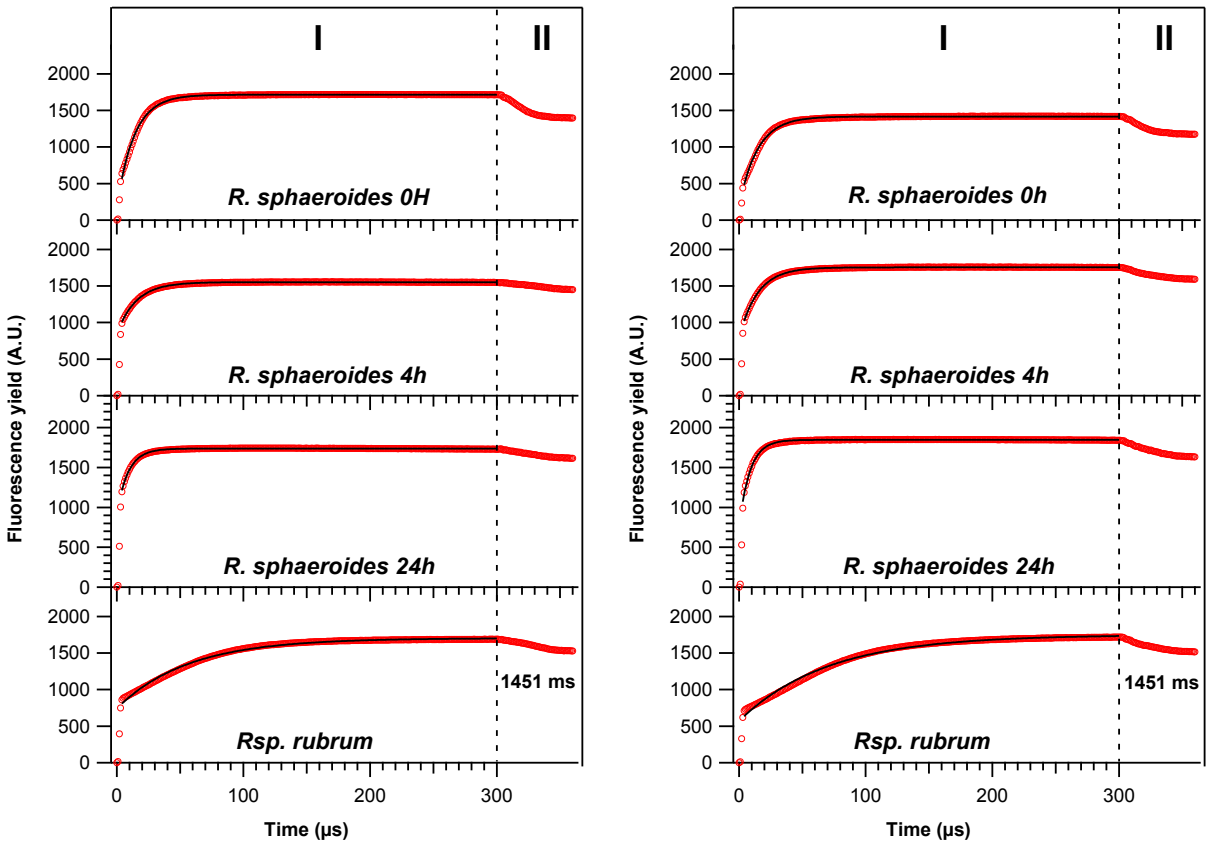

Figure 4. 6 | Fluorescence kinetics studies of *Rba. sphaeroides* and *Rsp. rubrum* chromatophores in suspension, obtained from fluorescence induction and relaxation measurements. The STF-τ transients (STF: single turnover flash, phase I; τ: fluorescence relaxation, phase II) are shown; STF (300µs), τ (1451 ms), the latter represents the width of the relaxation region. All measurements are the average of 50 iterations. (A) Performed in presence of horse heart cytochrome *c*. (B) Performed in presence of cytochrome *c* and quinone Q_0.

Figure 4.7 - Fluorescence Kinetics Studies of Chromatophores on Gold Surfaces

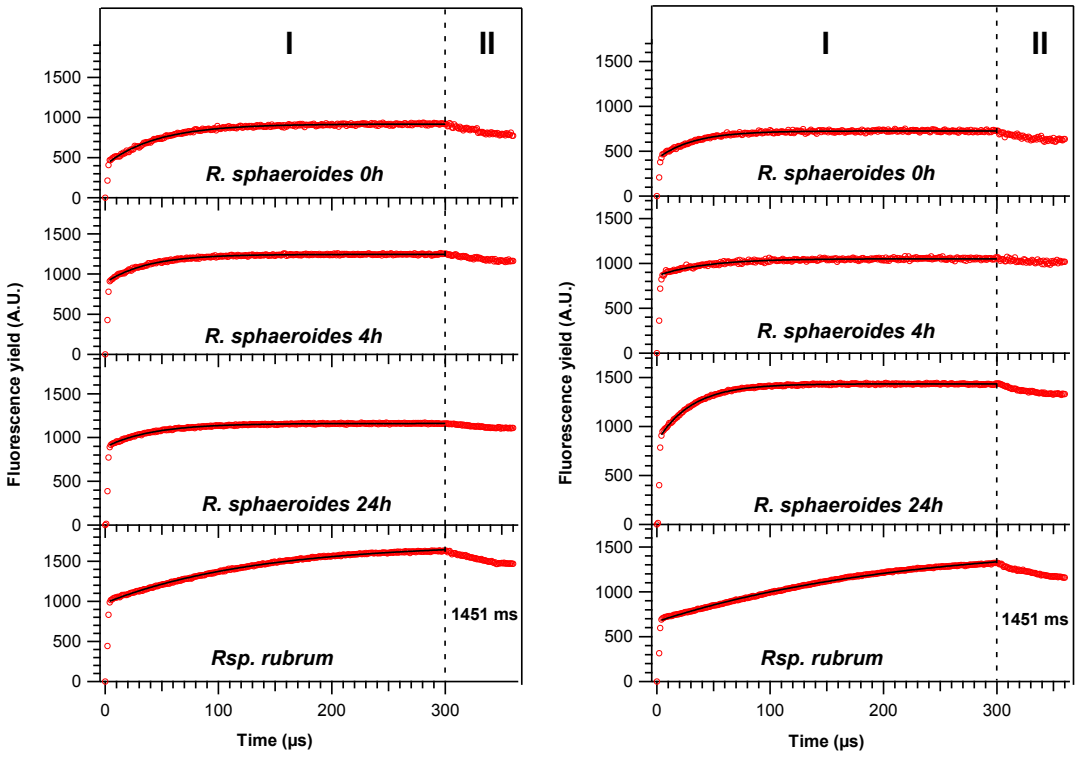

Figure 4.7 | Fluorescence kinetics studies of *Rba. sphaeroides* and *Rsp. rubrunm* chromatophores on gold-coated silicon substrates, obtained from fluorescence induction and relaxation measurements. The STF-τ transients are described in Figure 4.6 legend. All measurements are the average of 50 iterations. (A) Performed in presence of horse heart cytochrome *c*. (B) Performed in presence of cytochrome *c* and quinone Q_0..L

Figure 4.8 - Florescence Relaxation curve fitting

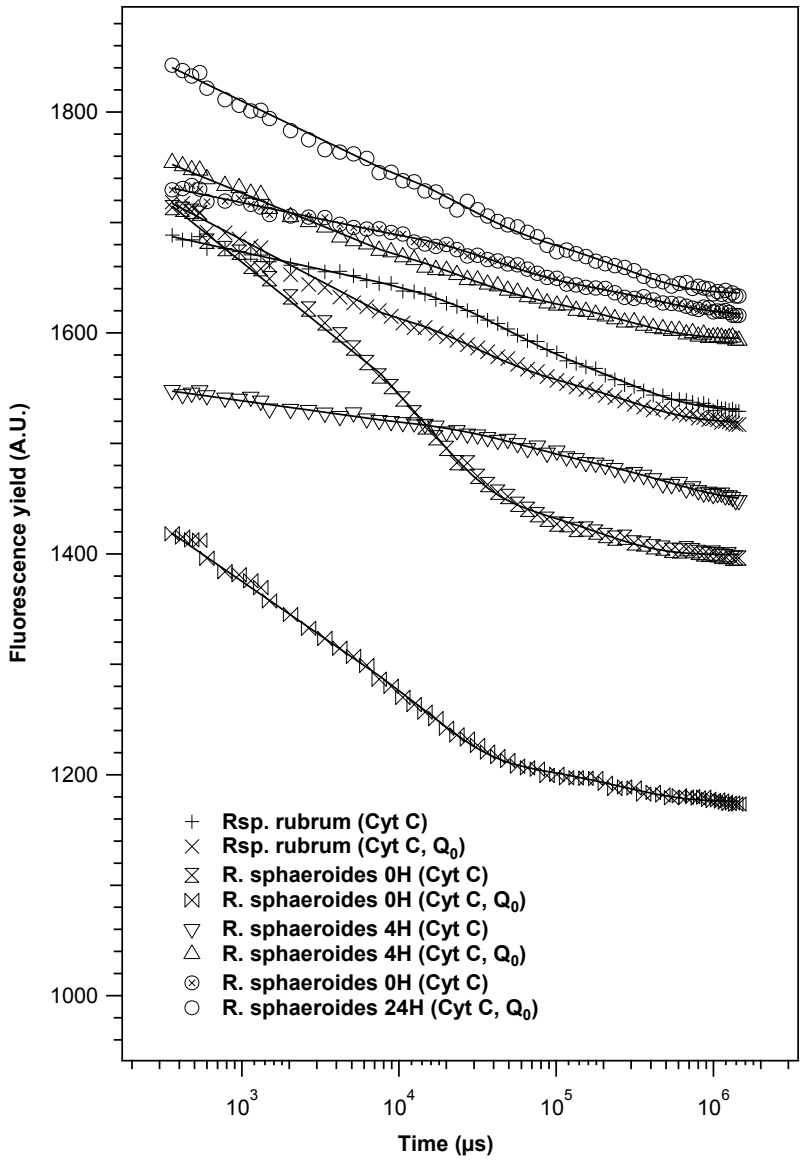

Figure 4.8 | Expansion of Region II in Figures 4.6A and B with fitting (see Table 4.1 and 4.2). The fitting requires three exponential terms corresponding to the time constants τ_1, τ_2, and τ_3. Cyt *c*, horse heart cytochrome *c.*

3.4 - Chronoamperometry

The photoinduced electron charge separation across the RCs results in a current that can be measured between the gold (working electrode) and the platinum (counter electrode) in the presence of the AgCl reference electrode (Figure 4.3). Chronoamperometry was implemented with chromatophores immobilized on commercially available gold electrodes with a radius of 1.5 mm under a full-spectrum white light source (Figure 4.9). The current reached a maximum of ~1.8 μ A/cm^2 quickly and was photostable for several hours at the maximal value under an illumination intensity of 220 mW/cm^2, while upon exposure to 19 mW/cm^2, a value of 0.5 μA/cm^2 was encountered. Thereafter, at 220 mW/cm^2, the current leveled off before being maintained at ≥0.5 μA/cm^2 for nearly 5 days.

When an 850 nm LED light source was used for illumination of the chromatophore electrodes (Figure 4.10), the *Rsp. rubrum* preparations were able to generate maximal currents of 1.5 μA at 181 mW/cm^2 and 0.8 μA at 97 mW/cm^2, whereas high-light *Rba. sphaeroides* chromatophores generated ~1.6 μA at 172 and 145 mW/cm. [136]

The LH2 antenna of *Rba. sphaeroides* has been shown to be largely inactivated when the chromatophores are absorbed to the gold surfaces. [43] While the *Rba. sphaeroides* LH1 complex was relatively stable, it is shown here that the photostability of the robust *Rsp. rubrum* LH1 was even greater, especially when illuminated under white light. This can be explained by the presence of LH2 in the *Rba. sphaeroides* chromatophores, which will not have as strong of a contribution to the current as the LH1, which *Rsp. rubrum* chromatophores utilize as the only light-harvesting antenna. The lack of LH2 would allow more surface area to be occupied by RCs that have a fixed ratio to LH1.[160]

Figure **4.9 - Electrochemical measurements of *Rsp. rubrum* chromatophores on Gold surfaces**

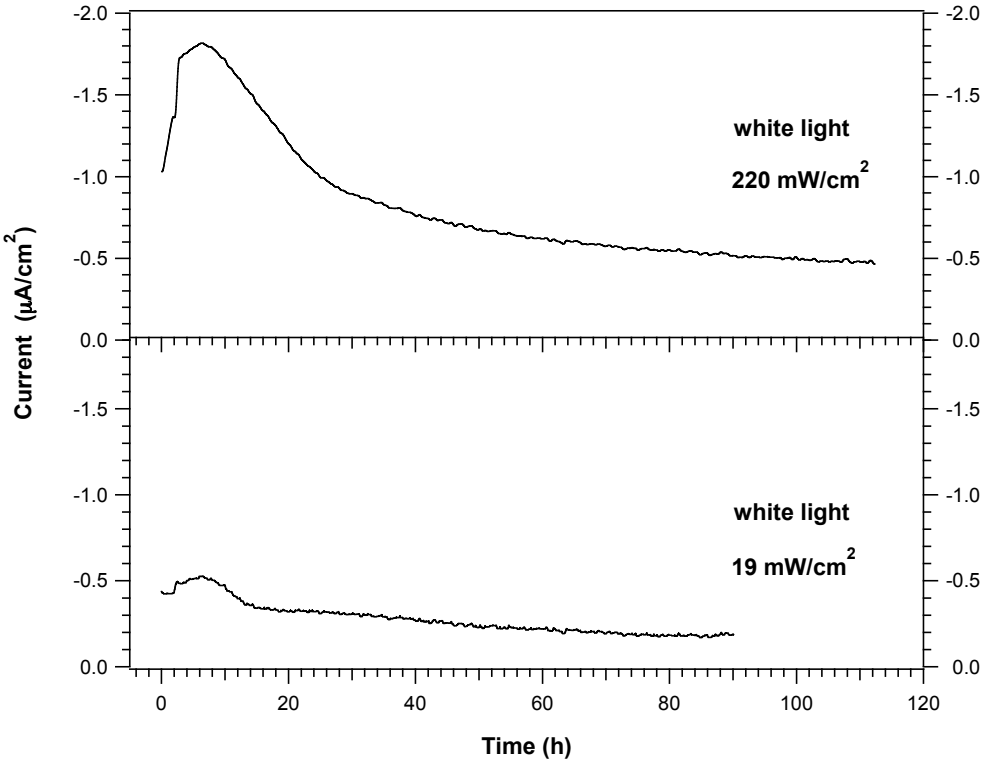

Figure 4.9 | Electrochemical measurements of *Rsp. rubrum* chromatophores adhered to Au-glass electrode surfaces under white light. The apparatus used for chronoamperometry is depicted schematically in Figure 4.3 and experimental details are presented in the text. Measurements were conducted in the presence of horse heart cytochrome *c* and quinone Q_0 as redox mediators and the system was polarized at -0.1 V *vs.* Ag/AgCl, 3 M NaCl at 25.00 ± 0.01 °C. See text for further details of these measurements.

Figure 4.10 - Electrochemical measurements of *Rsp. rubrum* and high-light *Rba. sphaeroides*

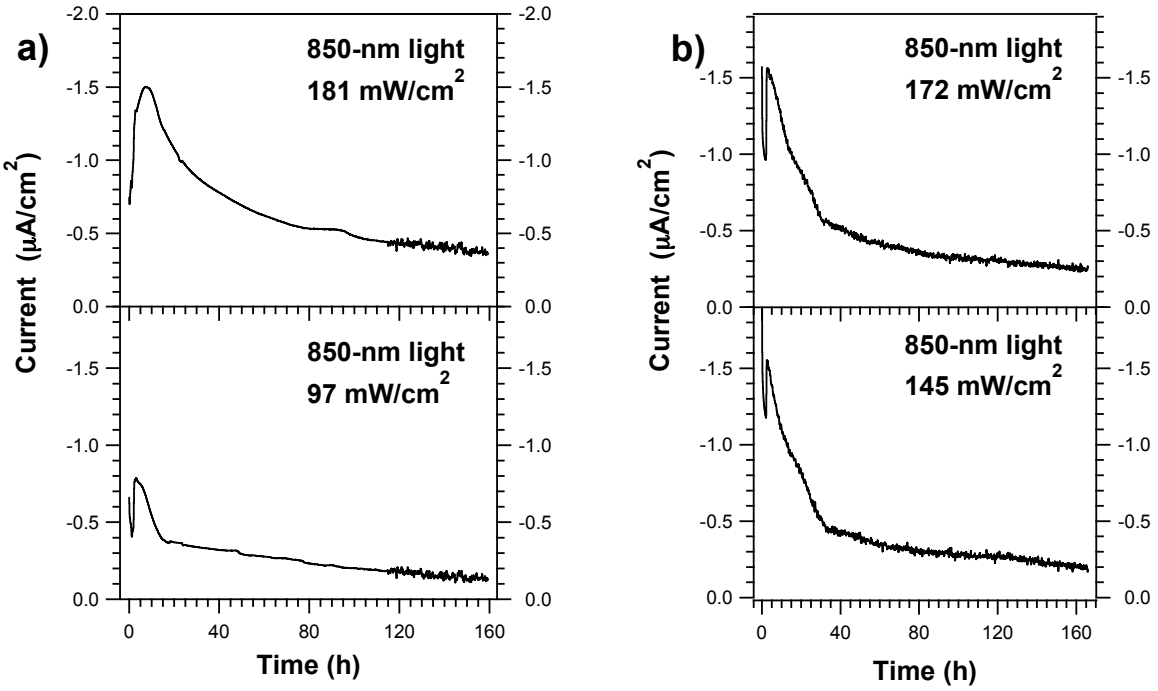

Figure 4.10 | Electrochemical measurements of (A) *Rsp. rubrum* and (B) high-light *Rba. sphaeroides* chromatophores adhered to Au-glass electrode surfaces under near-IR light (850 nm ± 10 nm bandwidth filter). The apparatus and experimental details are described in the text and in Figure 4.9 legend.

4. Conclusions

This study demonstrates that chromatophores isolated from *Rsp. rubrum* can be adsorbed onto gold surfaces. The adsorbed chromatophores were shown to generate a photodriven current when exposed to both white light and 850 nm radiation. When compared to chromatophores isolated from *Rba. sphaeroides*, these preparations showed more

robustness when exposed to high light. Under high 850 nm illumination, the total charge generated by the electrode is greater with the *Rsp. rubrum* chromatophores even though the peak current is slightly lower. This makes chromatophores isolated from *Rsp. rubrum* more suitable for incorporation into photovoltaic devices. In this connection, we have recently fabricated a biohybrid near-IR sensing dye-sensitized solar cell in which the light-harvesting dye was replaced with robust *Rsp. rubrum* chromatophores and the electrolytes with Q_0 and cytochrome *c*. [157] In the present study, we demonstrate that in the presence of residual cytochrome *c* and Q_0, it is possible to resolve three time constants in the fluorescence relaxation kinetics of both types of chromatophores in suspension. Moreover, the fluorescence studies reported here have facilitated determination of the surviving photosynthetic activity of the chromatophores when adsorbed to gold electrode surfaces.

Table 4.1 - Chromatophores in Suspension with Cytochrome c

Sample	LH1/LH2	F_0	F_m	F_v/F_m	σ_{CC} ($Å^2$/q)	*p*	τ_i (ms)
Rba. sphaeroides 0h Chromatophores	3.25:1.00	566	1720	0.67	86.2	0.10	τ_1 =1.15 ± 0.09 α_1 = 0.50 τ_2 = 15.3 ± 1.52 α_2 = 0.32 τ_3 = 242 ± 29.7 α_3 = 0.18
Rba. sphaeroides 4h Chromatophores	2.71:1.0	1007	1550	0.35	87.7	0.02	τ_1 =1.62 ± 0.26 α_1 = 0.25 τ_2 = 47.2 ± 7.4 α_2 = 0.30 τ_3 = 504 ± 69.2 α_3 = 0.45
Rba. sphaeroides 24h Chromatophores	1.00: 1.00	1214	1740	0.30	157	0.04	τ_1 =1.25 ± 0.19 α_1 = 0.32 τ_2 = 34.9 ± 4.40 α_2 = 0.39 τ_3 = 408 ± 75.2 α_3 = 0.29
Rsp. rubrum Chromatophores	NA	808	1700	0.52	24.0	0.42	τ_1 =1.11 ± 0.13 α_1 = 0.24 τ_2 = 37.2 ± 3.31 α_2 = 0.37 τ_3 = 280. ± 22.42 α_3 = 0.39

Table 4.1 | The parameters refer to the fluorescence yield profiles shown in Figure 4.6A. F_0 is the minimum of fluorescence, F_m is the maximum, $F_V = F_m - F_0$, F_V/F_m is the quantum yield of photochemistry, σ_{CC} is the functional absorption cross section. I is the irradiance. τ_i is a time constant and is obtained from the equation $f_{II}(t) = \sum_i^n A_i(\exp(-t/\tau_i)$ used in the fitting of the fluorescence in Region II; α_i corresponds to the ratio $\alpha_i = A_i / \sum_i^n A_i$

Table 4.2 - Chromatophores in with Cytochrome c and Q0

Sample	LH1/LH2	F_0	F_m	F_v/F_m	σ_{CC} ($Å^2/q$)	*p*	τ_i (ms)
Rba. sphaeroides 0h Chromatophores	3.25:1.00	482	1420	0.66	80.9	0.05	τ_1 =1.17 ± 0.09 α_1 = 0.39 τ_2 = 14.2 ± 0.8 α_2 = 0.47 τ_3 = 247 ± 30. α_3 = 0.14
Rba. sphaeroides 4h Chromatophores	2.71:1.00	1020	1750	0.42	91.1	0.04	τ_1 =1.51 ± 0.11 α_1 = 0.44 τ_2 = 20.5 ± 2.1 α_2 = 0.30 τ_3 = 268 ± 23 α_3 = 0.26
Rba. sphaeroides 24h Chromatophores	1.00: 1.00	1071	1850	0.42	149.5	0.04	τ_1 = 1.11 ± 0.12 α_1 = 0.40 τ_2 = 21.3 ± 2.5 α_2 = 0.33 τ_3 = 259 ± 29 α_3 = 0.27
Rsp. rubrum Chromatophores	NA	635	1730	0.63	21.0	0.11	τ_1 =1.31 ± 0.09 α_1 = 0.48 τ_2 = 25.9 ± 3.20 α_2 = 0.28 τ_3 = 282 ± 35.2 α_3 = 0.23

Table 4.2 | The parameters refer to the fluorescence yield profiles shown in Figure 4.6B. See Table 4.1 for definition of fluorescence parameters.

Table 4.3 - Chromatophores on Gold Surface with Cytochrome c

Sample	LH1/LH2	F_0	F_m	F_v/F_m	% (F_v/F_m)	σ_{CC} (Å^2/q)	τ_i (ms)
Rba. sphaeroides 0h Chromatophores on Au-glass	3.25:1.00	450	918	0.51	76	27.2	τ_{avg} = 47.3 ± 7.9
Rba. sphaeroides 4h Chromatophores on Au-glass	2.71:1.00	926	1250	0.26	73	38.7	τ_{avg} = 49.5 ± 89.0
Rba. sphaeroides 24h Chromatophores on Au-glass	1.00: 1.00	915	1160	0.21	70.	42.7	τ_{avg} = 39.0 ± 4.7
Rsp. rubrum Chromatophores on Au-glass	NA	1010	1640	0.39	93	16	τ_{avg} = 52.8 ± 6.3

Table 4.3 | Percentage retention of quantum yield of primary charge separation (F_v/F_m) with respect to the corresponding chromatophore suspensions in Table 4.1. The parameters refer to the fluorescence yield profiles shown in Figure 4.6A. See Table 4.1 for definition of fluorescence parameters.

Table 4.4 - Chromatophores on gold surface with Cytochrome c and Q0

Sample	LH1/LH2	F_0	F_m	F_v/F_m	% $(F_v/F_m)^a$	σ_{CC} ($Å^2/q$)	τ_i (ms)
Rba. sphaeroides 0h Chromatophores on Au-glass	3.25:1.00	449	726	0.38	58	29.5	τ_{avg} = 23.2 ± 5.6
Rba. sphaeroides 4h Chromatophores on Au-glass	2.71:1.00	877	1050	0.17	40.	37.9	τ_{avg} = 17.4 ±9.0
Rba. sphaeroides 24h Chromatophores on Au-glass	1.00: 1.00	917	1440	0.36	86.	31.9	τ_{avg} = 12.3 ±1.8
Rba. rubrum Chromatophores on Au-glass	NA	648	1330	0.51	81	12.9	τ_{avg} = 53.1 ± 7.9

Table 4.4 | Percentage retention of quantum yield of primary charge separation (F_v/F_m) with respect to the corresponding chromatophore suspensions in Table 4.2. The parameters refer to the fluorescence yield profiles shown in Figure 6B. See Table 4.1 for definition of fluorescence parameters.

Chapter VI. General Conclusions.

A grand challenge in chemistry and materials science is the design and construction of a bio-mimetic integrated system capable of light-harvesting, photo-induced charge separation and catalytic water oxidation / hydrogen formation[162]. Confidence in the possibility to build a *Supramolecular Functional Unit for Hydrogen generation (H_2-SFU)* having these characteristics is based on the advancements in two complementary research areas: 1) understanding of the molecular machinery of natural photosynthesis, and 2) the synthesis and supramolecular assembly of molecular analogs of light-harvesting antennas, photo-redox centers and redox catalysts. Progress toward an H_2-SFU would benefit enormously from a research effort in a *third bridging area*: the bottom-up reconstruction of the isolated molecular components of natural photosynthesis in a working *Photoelectrochemical System for Hydrogen Generation (H_2-PES)*.

In this study we pursued the latter goal by achieving the following objectives:

6.1- Synthesis of a GO based electroactive support

The synthesis of an electroactive support based on GO with Ni^{2+}-coordination sites (GO-NiNTA) on the model of immobilized metal affinity chromatography resins provides a scaffold that can be used as a basis for the assembly of a semi artificial photosynthetic system. GO provides an ideal chemical canvas that can be modified using known chemistry, is biocompatible, and can be used in suspension, as well as thin films on a surface. The suspension allows for a high density of bound protein per unit volume. Preparations of modified GO can be made in high concentrations with various size particles on the scale of hundreds of nanometers to the tens of micrometers and oxygen content between 8% and 35%. The GO used in this study had oxygen content of 20%. Thin films can be deposited on various supports including gold and quartz.

6.2 - Characterization of GO-NiNTA for immobilization of Histidine-tagged proteins

The Characterization of GO-NiNTA as a high-affinity surface for immobilization of Histidine-tagged proteins and its possible use in chromatographic applications shows 5 to 10 times higher protein binding capacity compared to commercial resins. This allows for more protein to be isolated with the same volume of resin. The graphene based resin utilizes inexpensive and readily available starting materials suitable for possible scale up. GO-NiNTA resin shows a greater than 50% improved specificity compared to commercial resins depending on protein target. It may be possible to use GO-NiNTA for protein purification in a single step without the need of ion exchange and size exclusion procedures.

6.3 - Vectorial orientation of photosystem II core complexes on GO-NiNTA.

PSII CCs isolated from *T. elongatus* can be immobilized onto the GO-NiNTA support. Electron flow between the core complexes and GO-NiNTA has been shown to be possible. The extent of electron transfer depends on the oxygen content, which confer electron-conducting or hole-conducting character to the basal plane of GO. Electron tunneling is possible through a single-layer of graphene oxide to a metallic support as shown by variable fluorescence experiments.

6.4 - Study of the oxygen evolution activity of PSII on GO-NiNTA.

PSII core complexes can transfer electrons directly and indirectly to GO in suspension. The rate at which the water oxidation complex can turn over is thereby increased by a factor of 2 to 3. Both transient and stationary oxygen evolution experiments provided evidence in this regard. The stationary rate of oxygen evolution at 45 °C in GO-NiNTA-PSII under continuous light in the presence of ferricyanide increases above 7900 mol O_2 / (mg Chl · h), more than twice the rate observed in the case of PSII *in vitro* (3500 mol O_2 / (mg Chl · h)).

6.5 - Vectorial orientation of PSII and PSI core complexes

Both PSII and PSI core complexes can be co-immobilized on GO-NiNTA. The electronic communication between the core complexes was verified with the help of a kinetic model necessary for the rationalization of the data. Joliot-type Spectroscopy (JTS) was used to probe PSI and PSII attached via the GO-NiNTA resin. The percentage contribution of PSII to the electron flow via the GO to the PSI was determined using the proposed kinetic model.

6.6 - Chromatophores containing bRCs bound to gold show charge separation.

Chromatophores isolated from *Rsp. rubrum* can be adsorbed to gold surfaces. These chromatophores can generate a photodriven current when they are exposed to light. When compared to chromatophores isolated from *Rba. sphaeroides* the *Rsp. rubrum* chromatophores are more robust and will last longer when exposed to high light. This is due to the lack of the LH2 antenna complex. This shows that *Rsp. rubrum* chromatophores are better suited for incorporation into biohybrid photosynthetic systems.

6.7 - Future directions

The modular system investigated in this thesis can be used to build up a biohybrid electron transport chain that can utilize natural and artificial photosynthetic components. The benefit of this system is the ability for each component to be individually added, removed, or changed to enhance the properties of the system as a whole, or simply to test new solutions to each step of the overall pathway. This bio-hybrid photosynthetic system can be used as an important tool in understanding not only the natural bioenergetics of photosynthesis, but also to help make advancements in artificial photosynthesis. The *Rsp. rubrum* chromatophores have been incorporated into photovoltaic devices to replace systemic dyes as sensitizers. These biological antennas and others show promise as biocompatible components of photovoltaic systems. The GO-NiNTA resin shows promise as a protein purification resin and is currently

under development for that purpose. This material also has potential to take advantage of the vectorial orientation of proteins as well as the electrical properties explored in this thesis.

Appendix A - Instrumentation

The study of biological molecules interfaced with conducting supports requires a large set of physical-chemical instrumentation and methods. The experimental details of individual techniques have been grouped into five categories. Microbiological techniques are used for growing single celled phototrophs used in these studies. Separation techniques are used in the isolation of proteins and chromatophores from the cellular extracts. Spectroscopic techniques provided information about the electronic and vibrational properties of the analytes. Electrochemical techniques were utilized for measuring kinetic and thermodynamic properties of protein-electrode bioconjugates and chromatophore-electrode systems. Finally, surface techniques provided information about the morphological characteristics of the biological components immobilized on conductive supports. Overall, these techniques allowed us to obtain evidences about the nature of proteins and chromatophores and their interactions with supporting materials. In this chapter brief introductions and explanations about the principles pertinent to each technique are given, a good starting point for a deeper understanding of the data presented in following chapters.

A 1. Microbiological Techniques

Phototrophic bacteria were the sources of photosynthetic CCs and membranes used in this study. Once the single celled organisms were grown to sufficient biomasses, the molecules of interest had to be extracted and purified. This section describes some fundamental aspects of cell growth and extraction processes. The protein purification protocols are covered in detail below.

A 1.1 - Cell Growth

Requirements for cellular growth can vary greatly depending on organism and the intended use of the cell culture. Growth conditions can have an effect on the expression of

target biomolecules. The bacteria utilized in this study were all grown phototropically. This type of growth condition requires optimal exposure of the microorganisms in the photosynthetically active region (PAR) usually taken to be between 400 nm and 700 nm. PAR is mostly in the visible light range (400-700 nm) in the case of cyanobacteria but it extends to 900nm in the case of the purple non-sulfur bacteria. The irradiance conditions can change the way the organism expresses the photosynthetic apparatus. In the case of *R. sphaeroides* the ratio of light harvesting antennas that are present in the chromatophore will change with the light intensity. Under high light intensity (1100 mW/cm^2) the lowest LH2/LH1 ratio is observed; when the cultures are placed in low light conditions (30 mW/cm^2) then the ratio increases. [157] This behavior is due to the organism adapting to the different light conditions. The cross section of the LH2 antenna is larger and therefore the increase numerical density of LH2 with respect to LH1 will increase the probability that the incoming light will reach the reaction center. When there is abundant light then the LH2 levels are markedly diminished and the RC-LH1 core articles are preferentially expressed.[163] The *Rsp. rubrum* bacterium can grow constantly under a wider range of light intensities despite the absence of the LH2 antenna complex. A commonly use precaution for keeping the cells from contamination is the use of antibiotics. Antibiotics are molecules that will keep bacteria from growing. This was used when generating the PSI and PSII CCs. Kanamycin antibiotic resistance was encoded in the vector along with the polyhistidine tags at chose protein termini.[95] Antibiotic resistance will allow only the cultures that have the added vector to grow, and thus selecting for the polyhistidine tag. Relatively low concentration of antibiotics (40 µg/L in *T. elongatus*) inhibits growth of other bacteria in the media.

A 1.2 - Cell Lysis

In order to use the biomolecules in this study the cells needed to be broken to release the cytoplasm. French Press is the preferred method to lyse the cells. In this method the cells

are placed into a reinforced cylinder. A piston applies pressure to the cell suspension. This pressure can range from 700 psi (4,826 kPa) to 3000 psi (20,648 kPa) in the case of *T. elongatus* and *Rsp. rubrum*, respectively. The cell suspension is released drop by drop from the cylinder. The sudden expansion of gases results in explosive decompression that ruptures the cells, releasing the cytoplasm and fragmenting the cellular membranes. [164]

A 2. Separation techniques

Biochemical studies often require the isolation of proteins of interest. There are many techniques that are used toward this goal, independently or in combination with each other. These methods rely on the different physical and chemical interactions toward a stationary phase of the biomolecule of interest as opposed to other components of a crude mixture. Chromatography is a particular type of separation technique, which is used to separate a mixture of different compounds in solution into its constituent components. There are many different types of chromatography techniques.

A 2.1 - Affinity Chromatography

Affinity Chromatography relies on highly specific interactions between a molecule and the stationary phase. These interactions involve an immobilized ligand with high affinity toward an epitope-tag, a particular antigenic determinant or peptide sequence. For instance, a poly-Histidine tag can interact with a Ni^{2+}, Co^{2+}, or Zn^{2+} coordination sites in what is known as immobilized metal affinity chromatography (IMAC). [165] IMAC purification offers high protein loading capacities with mild elution conditions, relative stability of the ligand, and moderate costs.[166] The metal is immobilized by a polydentated ligand such as nitroloacetic acid (NTA) linked to the support. The support is typically a polysaccharide such as agarose or sepharose. Metal ions show affinity for many residues like Glutamine, Tyrosine, Arginine, Methionine, and

Lysine. These interactions can contribute to binding but the prevailing interaction of the protein to the stationary phase is due to the available histidine residues. Aromatic side chains (Phenylalanine, Tryptophan, Tyrosine) can contribute to the binding if they are in proximity of the Histidine tag. In rare cases cysteines can play such a role if they are freely available and in the reduced state.[166, 167] Proteins with several native histidines can be purified without modification. This was the original use for the technology. Nowadays, this technique is mostly used to isolate proteins that have been specifically altered to contain the polyhistidine tag (generally 6 residues). [165, 168, 169]

The protein of interest is adsorbed to the resin at a pH at which histidyl residues are in a non-protonated form. These conditions are generally neutral or slightly basic. High ionic strength buffers are used to reduce nonspecific interactions. Bound proteins can be eluted from the stationary phase by using a buffer with a lower pH or by introducing a chelating agent that will have a higher degree of affinity to the metal than the protein. In the case of our study a gradient of imidazole was used to elute the sample. EDTA may be present in some cases as a scavenger for metal contaminants. In this study, the mobile phase had low concentrations of these chelating agents even during the adsorption stage in order to balance the pH and limit nonspecific binding of naturally occurring histidines.[170] The use of an eluting agent that is excessively strong would result in complete elimination of the metal ion from the stationary phase. In this situation the resin must be recharged with the metal ion of interest. Stripping the ions from the resin is used purposely for cleaning and recharging the stationary phase after several purifications.

Poly-histidine tags have been successfully and routinely expressed in both prokaryotic and eukaryotic organisms.[165, 171] The His-tag may be removed from the protein. This is generally

required in the case of biologics of pharmaceutical interest. N-terminal tagging is most common due to the availability of efficient endoproteases that can cleave the recombinant extension after purification. In some cases, it may not be possible to remove the tag without causing damage to the target protein. Affinity chromatographic techniques must be used for these molecules. However, in many cases the Histidine-tag will not interfere with the biological function. There are many examples of clinical and preclinical trials for biologic therapeutics in which the His_6-tag is not cleaved off. [165, 172-175] Often analyses of the target proteins require a very high degree of purity for applications such as crystallography. For these applications multiple steps after the IMAC purification process are required. There is the need to cope with many other proteins other than the protein of interest.[165] Nonspecific binding can accounts for 20-50% of the bound protein. [176] After this phase many proteins must undergo further purification.

A 2.2 - Gel electrophoresis

Gel electrophoresis can be used to separate mixtures of proteins from a cell lysate, partially isolated mixture, or a few proteins. The proteins are loaded onto a polyacrylamide gel that has pores that protein can travel though. The samples are loaded onto the gels into small wells that are formed during the casting of the gel. The proteins are denatured before being loaded onto the SDS PAGE gel (Sodium Dodecyl Sulfide PolyAcrylamide Gel Electrophoresis) for separation. The SDS is a detergent that will solubilize the protein. This type of gel reduces the effects of secondary, tertiary, and quaternary structure. Leaving all samples are in monomeric form, and the mixture is separated exclusively on the basis of size. In native gel electrophoresis the proteins are not denatured but kept in the natural state. In this type of gel the proteins keep

their quaternary structure and therefore will show the size of dimer, trimer, or other biological aggregates. An electrical current is passed through both types of gel and their surrounding buffer. The proteins will travel down the gel for a distance that is inversely proportional to the log of the mass of the protein. The gel can be imaged via intrinsic fluorescence or staining with dyes such as Coomassie Blue or silver stain.

A 2.3 Separation by differential centrifugation

Centrifugation is used extensively in protein separation protocols. Two main types were used during this study. For differential centrifugation, the speed of the centrifuge was chosen on the basis of inspection of the samples or their known behavior. In the case of the whole cells the speed was relatively low, 5000 x g, resulting in the formation of a cell pellet. After the cells were broken, the lysate containing the thylakoid membranes would stay in suspension during the centrifugation. When membranes are solubilized in a detergent such as β−Dodecyl Maltoside (β−DM) the photosystem RCs are extracted and remain in the supernatant, while the membranes form a pellet.

Rate-zonal centrifugation is the other main way in which centrifugation was utilized in this study for the purpose of isolating proteins. This method uses a centrifuge tube that is filled with increasingly high concentrations of sucrose in buffer that from a sucrose gradient. In this study, these concentrations have span ranges of 5-15% up to 5-40%. The density of the sucrose gradually increased as the sample travels down the centrifuge tube. The protein containing membranes will travel down the gradient and separate based on the size of the particle; leaving a band of membranes containing the bRCs. The membranes used in this study were pigmented and was removed by pasture pipette after chromatic identification.

A 2.4 Flow Cytometry

Flow cytometry is a uniquely different type of separation technique. This technique was developed in order to isolate a large number of viable cells destined for biochemical experiments. [177, 178] On a very fundamental level flow cytometry sorts much the same as with macroscopic objects. The instrument isolates the cells or particles individually. Flow Cytometers are comprised of three main systems. These are the fluidics, optics, and electronics. The sample is first filtered into a reservoir to eliminate particles outside of the scope of the instrument form interfering. The cells are removed from reservoir via a capillary. The capillary is surrounded by a sheath, which carries a fluid. This sheath fluid dilutes the sample exiting the capillary in such a way that individual cells can be observed. (Figure A 1) Felix Savart first described this phenomenon of uniform droplets forming while fluid is passed through a circular opening in 1833, and later analytically described by Rayleigh in 1879. [179-181] Once these cells are separated from one another in the outgoing stream they are passed through a laser light source. The flow cytometer measures particle size in terms of scattering and fluorescence intensity. In our case it provides also information about the bioconjugates and the aspect ratio of the particles going through the cell. The probing light is passed through semi-reflective filters that will transmit some light but reflect other wavelengths to a photodetector. In this way the incident light can be separated into several frequencies for fluorescence and scattering detection. The detection system identifies events via fluorescence, forward, and side scattering. The basic schematic shown in Figure A 2, which depicts how the forward and side scattering information is collected simultaneously. The instrument is capable of sorting cells automatically, in the so-called gates. The cells traveling in a narrow stream are deflected by a perpendicular electric field. Flow cytometry is used in this study for the sorting of graphene oxide derivatives and GO-based bioconjugates rather than in the separation of cells

Figure A 1 – Flow Cytometry Sorting

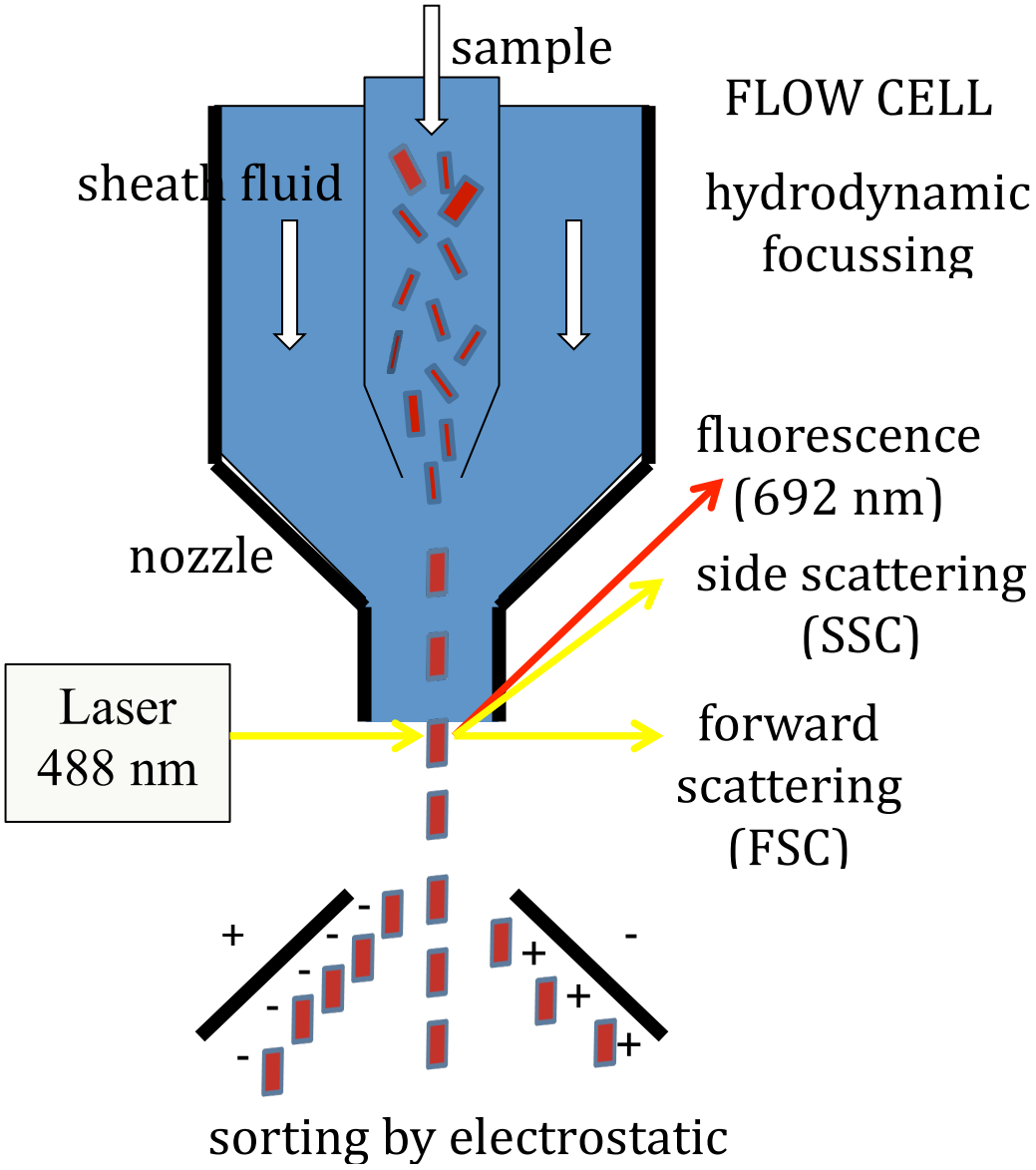

Fig A 1 | This diagram shows the way in which the sample is passed through a capillary with a sheath fluid moving out of an orifice surrounding the opening of the capillary. This dilution can separate individual cells. The individual droplets are sampled by the laser and with an automated system the droplets can be sorted by changing the charge to direct the droplet into a particular tube.

Figure A2 - Forward and Side Scatter Detection for Flow Cytometry

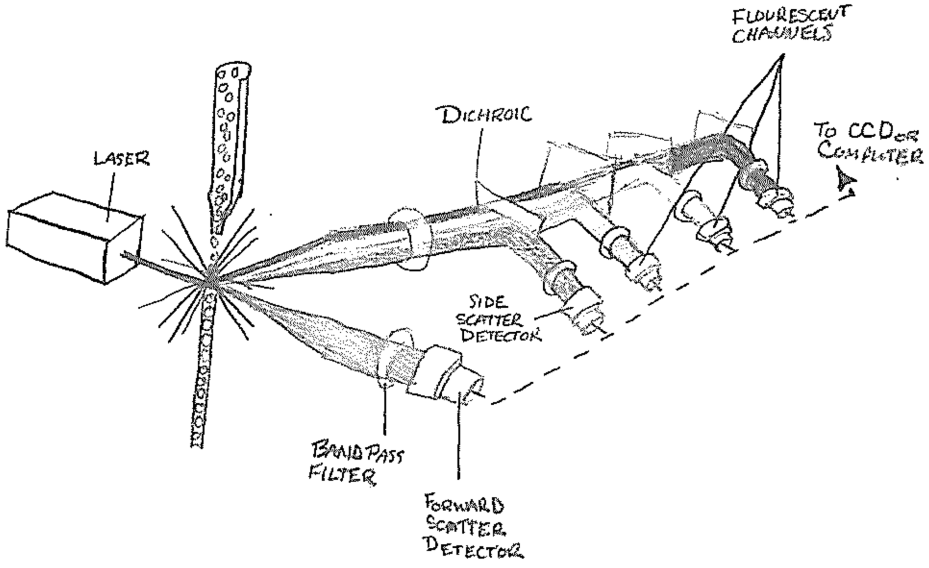

Figure A 2 | The probing light is passed through dichroic semi-reflective filters. Each filter will pass some light and reflect some to a particular photodetector. This coupled with the forward scatter detector will give the sample's forward, side, and photoluminescence. The instrument uses this to identify events. This basic schematic shows how the light is sent to the photodetectors.

A 3. Spectroscopic measurements

Spectroscopy is the study of electromagnetic radiation emitted or absorbed by a given chemical species.[182] (Figure A 3) When matter is exposed to electromagnetic radiation in the visible, infrared, or ultraviolet region the light can be absorbed, transmitted, reflected, scattered or undergo photoluminescence. The wavelength of the electromagnetic radiation determines the way in which the light energy, proportional to the frequency of the radiation, will interact with the sample. This energy can be absorbed, transmitted, or dependent on an electronic transition. (Figure A 4a) Many pigments involved in the photophysics and photochemistry of photosynthetic organisms will absorb in the visible and near IR regions. The covalent bonds of organic molecules each absorb in the IR region, which corresponds to vibrational degrees of freedom. Some molecules will absorb frequencies of light and undergo nonradiative relaxation that will result in a photoluminescence event characteristic of the analyte.

Figure A 3 – Electromagnetic Spectrum

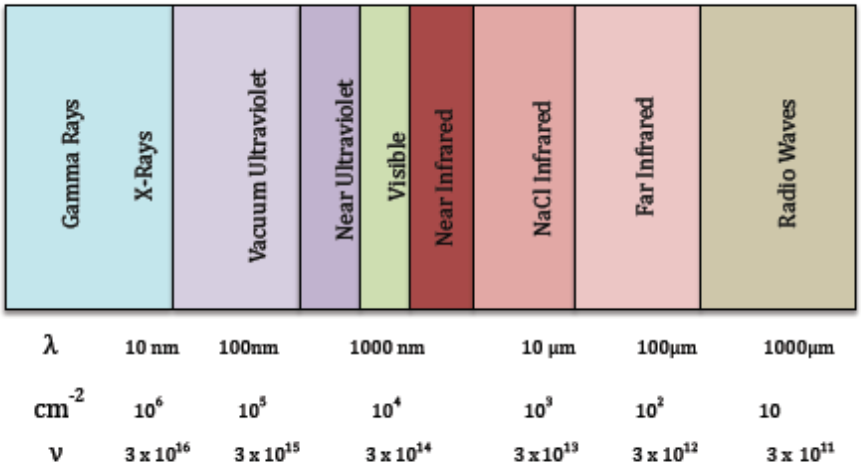

Figure A 3 | The electromagnetic spectrum. Each region of light has a different interaction with matter.

Figure A 4 – Light Interacting with Matter

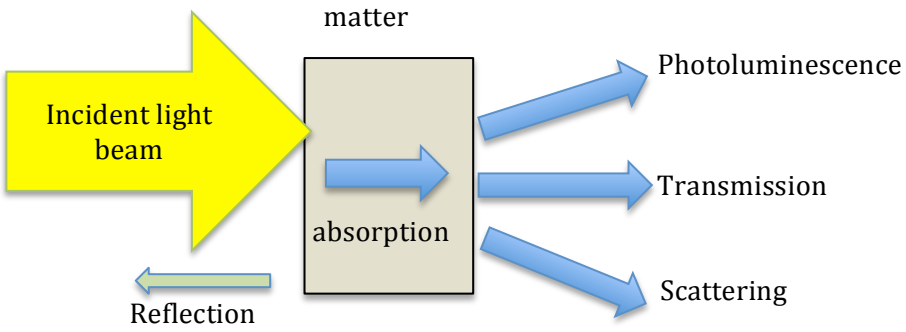

Figure A 4a | This figure shows the way light interacts with matter. When a beam of light interacts with a sample the light can be reflected, absorbed, transmitted, scattered or cause photoluminescence.

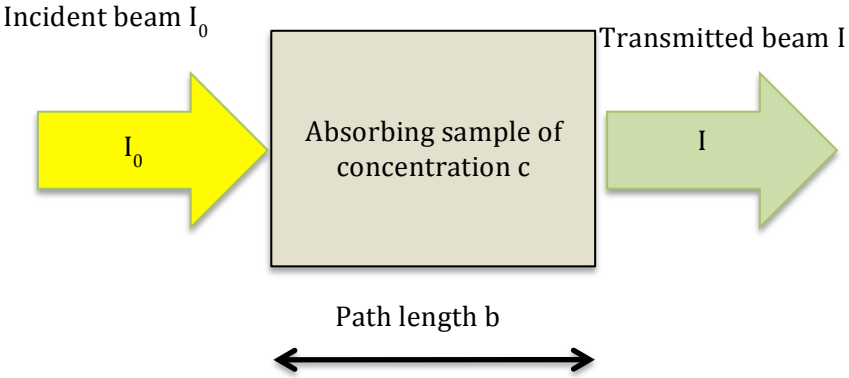

Figure A 4b | The Beer lambert law (equations A 1) describe the ratio of incident light to transmitted light for a particular path length.

A 3. 1 - Absorption spectroscopy: Ultraviolet and Visible (UV-Vis)

Ultraviolet and visible absorbance spectroscopy is one of the basic tools used in biochemistry research. Liquids are colored as a consequence of partial absorption and reflection of incident light. This phenomenon extends to wavelengths of light that are not visible to the human eye. In photosynthesis many of the pigments are visibly colored. Typically conjugated chemical bonds in each sample will absorb incoming light and the complement light will be transmitted. The energy of the light (wavelength) can cause electronic transitions. These transitions provide information about events on a short time scale. These features allow meaningful spectroscopic measurements on the pigments involved in electron transport. The absorption spectrum is a fingerprint that can be used to identify the pigments present, their concentrations, and the interaction between them and their environment. The absorbance is given by the well-known Lambert-Beer law (equations A 1).

$$A = -\log T = \log \frac{I_0}{I} = \varepsilon bc \qquad \text{(Eq. A 1)}$$

A is the absorbance, a dimensionless variable (a.u.). T is transmittance, I_0 is the incident light intensity, and I is the transmitted light intensity, ε is the molar extinction coefficient. These values are represented in Figure A 4b. The value of this parameter depends on the wavelength measured and the particular sample being analyzed. The term b is the path length or distance travelled by the light inside a sample. The value of this parameter is often measured in cm. c is the concentration in mol/L. The absorbance value is proportional to the concentration of sample at a particular given wavelength. Therefore the concentrations of samples that absorb within the spectral window of the measurement can be quantified and stoichiometric ratios between species can be obtained. [182,183] Most of the spectrophotometers in use have a range from about 190 nm to 1100 nm. For absorbance measurements below 400 nm it is not possible to use the

disposable poly-methyl methacrylate (PMMA) cuvettes. Quartz cuvettes must be used instead because they are transparent to UV frequencies.

A 3.2 - Fourier-Transform Infrared Spectroscopy (FTIR)

The FTIR spectroscopy is a spectroscopic technique that measures the absorbance or transmittance by a sample in the Infrared region of electromagnetic radiation. Infrared light absorbed causes change in the rotational and vibrational states of molecules. [184] The frequencies at which a molecule absorbs corresponds to its normal modes. Normal modes are synchronous motions of the entire molecule. The dipole moment of a molecule may change as a result of a molecular vibration and is correlated to the intensity of the infrared absorption by the molecule. Only molecules whose absorption cause change in dipole moment will absorb infrared light. This produces a characteristic spectrum for each molecule. The spectrum allows the identification of the material, as it is unique to a specific structure. [185] Molecules that have no dipole moment such as oxygen, nitrogen and carbon tetra-chloride cannot be measured with this technique. Molecules such as water and carbon dioxide will show a signal, and in fact they are common contaminants in measurements that must be dealt with.

FTIR spectroscopy is the method often selected over the dispersive or filter analysis methods by giving a better signal to noise ratio than dispersive techniques. A broad range of frequencies can be measured over a short period of time, and this allows multiple scans of the sample to yield more precise results. The FTIR spectrophotometer consists of a few basic parts. The light source consists of a filament emitting in the IR range. Two common filaments are the Nernst and glowbar filaments. The optical path must consist of materials that are transparent to the IR frequency interval that is used for the measurements. Common materials used are NaCl or KBr crystals. The latter is the material of which the windows are made in our FTIR instrument.

The windows must be present in an environment that has low humidity in order to avoid damage to the salt optics. The two most common detectors normally used rely on either the heating effect of the radiation or photoconductivity.[186] The signal is passed through an optical system comprised of half and full mirrors known as a Michelson interferometer (Figure A 5). The incoming beam is split in two by a beam splitter. The two beams recombine after they have traveled different distances. This produces interference between the two electromagnetic waves. The interference between the two beams can be monitored as a result of this path length difference by use of the detector. [184]

Figure A 5 – Michelson Interferometer

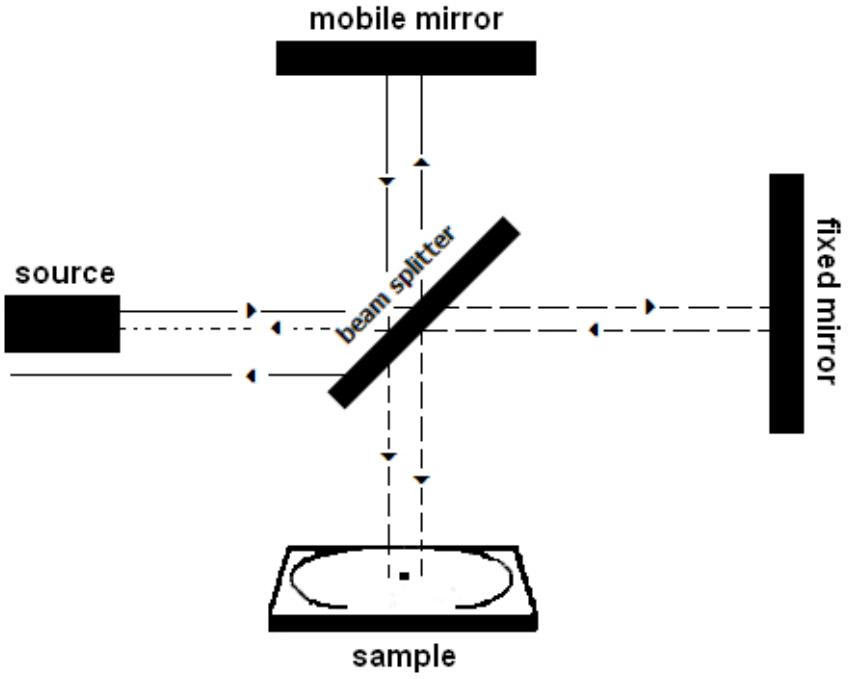

Figure A 5 | A schematic representation of the Michelson Interferometer. The light beams split and returns to the sample after traveling different distances.

Different types of cells can be used in the sample compartment. Many samples are simply sandwiched between transparent disks of KBr in hermetically sealed cells. A liquid cell requires the suspension or dissolution of the sample in IR transparent fluids (e.g. carbon tetrachloride). The liquid cell is still based on the IR transparent salts with a hole in one window giving access to insert a sample. Analytes can be ground and mixed with salt using a mortar and pestle and then pressed into a crystal. An attenuated total reflectance (ATR) cell was also used. The sample was placed on a crystal of ZnSe, which has a higher refractive index than the sample. [187] The signal is mostly reflected off the surface of crystal with some emerging on the other side and interacting with the sample. The light that is reflected off the mirror on the other side of the sample is transmitted to the detector. This signal has been attenuated or reduced by the absorbance of the sample. The resulting signal contains vibrational information about the sample itself. [186] The mathematical operation called Fourier transform is used to change the signal from the time domain to the frequency domain. The frequency spectrum describes the time-domain signal in terms of complex amplitudes. The instrument software uses a numerical approximation known as a fast Fourier transform (FFT) that allows quick solutions within the accuracy required for the measurement. [184] In this study FTIR was used to investigate the chemical modification of the GO to the resin material with and without protein attached.

A 3.3 - Pump-Probe Spectroscopy (JTS)

We measured the activity of PSI using Joliot-type spectroscopy with a JTS-10 from Bio-logic USA. The instrument is a pump-probe spectrophotometer. It is a high-resolution spectrophotometer that is specifically designed for electron-transfer studies in photosynthetic organisms via fluorescence and absorbance changes. JTS is a technique that utilizes two sample

locations with their own monochromatic illumination sources, tandem photodetectors, and the ability to compare these signals. The samples are at right angles of each other with a light source split by a diffraction grating. [188]

The Joliot-type spectroscopy measurements were taken in absorbance change mode in the case of PSI CCs. The JTS measurement was set up with a polychromatic probing light from 700 to 740 nm passing through a 705 nm filter. The green actinic light at 532 nm has a low irradiance of 50 $\mu E/m^2$ s and the orange saturating light at 639 nm has an irradiance of 3000 $\mu E/m^2$ s. At time zero P_{700} within PSI is completely reduced, due to the excess of ascorbate and diclorophenol indophenol (DCPIP) in the sample. This dark-adapted sample is illuminated with the green actinic light at 532 nm low irradiance light. This will oxidize the P_{700} to P_{700}^+ to a point where the oxidation and re-reduction is equal. The system is in a steady states condition. After that is achieved the 639 nm saturating flash of about 200 ms completely oxidizes the P_{700}. The system is then allowed to re-reduce back to the fully reduced state. From this absorbance change the rate of P_{700} oxidation; the P_{700}^+ saturation and the P_{700} steady state contribution can be determined. During the "dark phase" after the saturating flash the rate of re-reduction of the P_{700} can be measured. This study used the JTS to measure the change in absorbance of P700 in PSI to obtain information about the electronic communication between bound photosynthetic CCs facilitated by GO.

Figure A 6 – Joliot-Type Spectroscopy setup

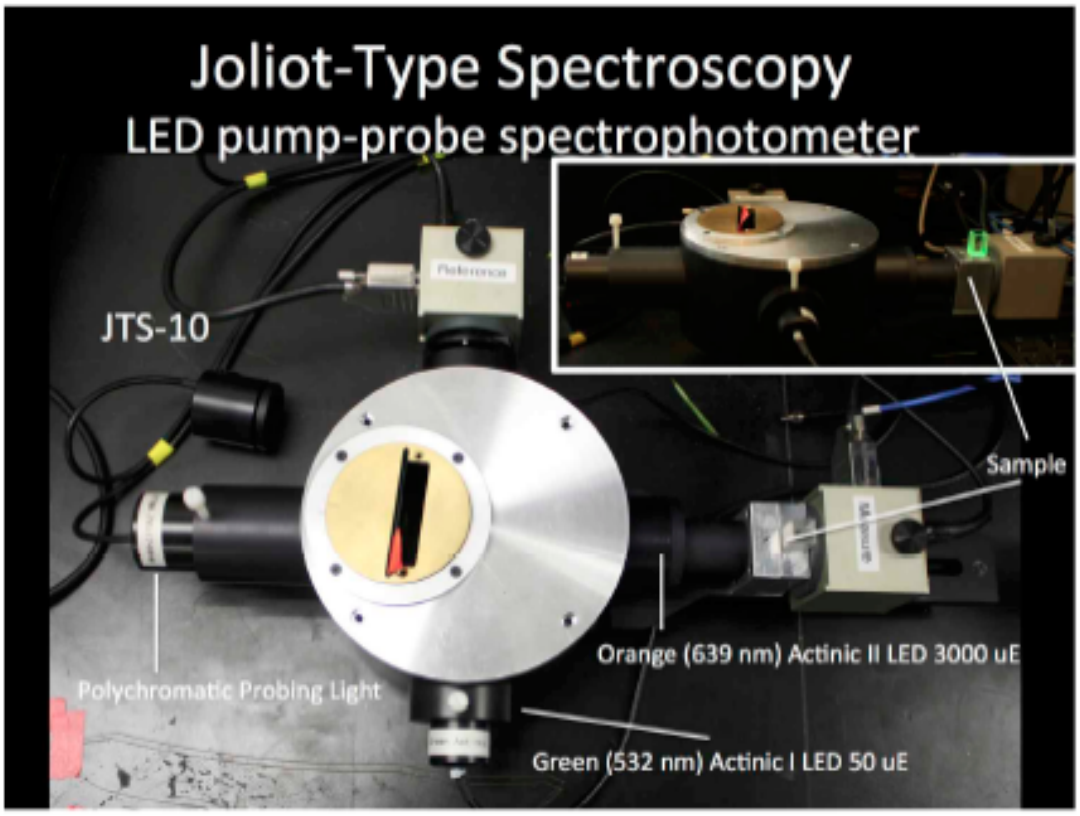

Figure A 6 | The activity of PSI was measured using a JTS-10 from Bio-logic USA. The instrument is a pump-probe spectrophotometer that has a polychromatic probing light from 700 to 740 nm passing through a 705 nm filter. The green actinic light at 532 nm has a low irradiance of 50 µE/m^2s and the orange saturating light at 639 nm has an irradiance of 3000 µE/m^2s.

A 3.4 - Fluorescence / Variable Fluorescence

Fluorescence Induction and Relaxation (FIRe) is a non-destructive measurement technique to measure the maximum fluorescence (F_m), quantum yield of photosynthesis (F_v/F_m), the energetic connectivity (p) among PSII RCs, the functional absorption cross section (σ) and the relaxation parameters (τ_1, τ_2, τ_3) that give the rate of electron transfer from PSII RCs. The sample is exposed to short saturating pulses known as "flashlets". The timescale for the flashlets is set to saturate the reaction center and yield a single turnover referred to as the single turnover flash (STF). The single turnover flash is modeled by a cumulative Poisson distribution (approximately a single exponential rise), and the single turnover relaxation period is simulated by a triple exponential decay.

The decay coefficients are assigned to particular physiological events in PSII, namely τ_1 describes the transfer of 2 electrons form Q_A to Q_B, τ_2 represents the transfer of the Q_B out of the pocket, and τ_3 provides information about the electron transfer of damaged reaction centers. This can give information about the activity of PSII in the live cells and *in vitro*.

Figure A 7 – Typical FIRe output

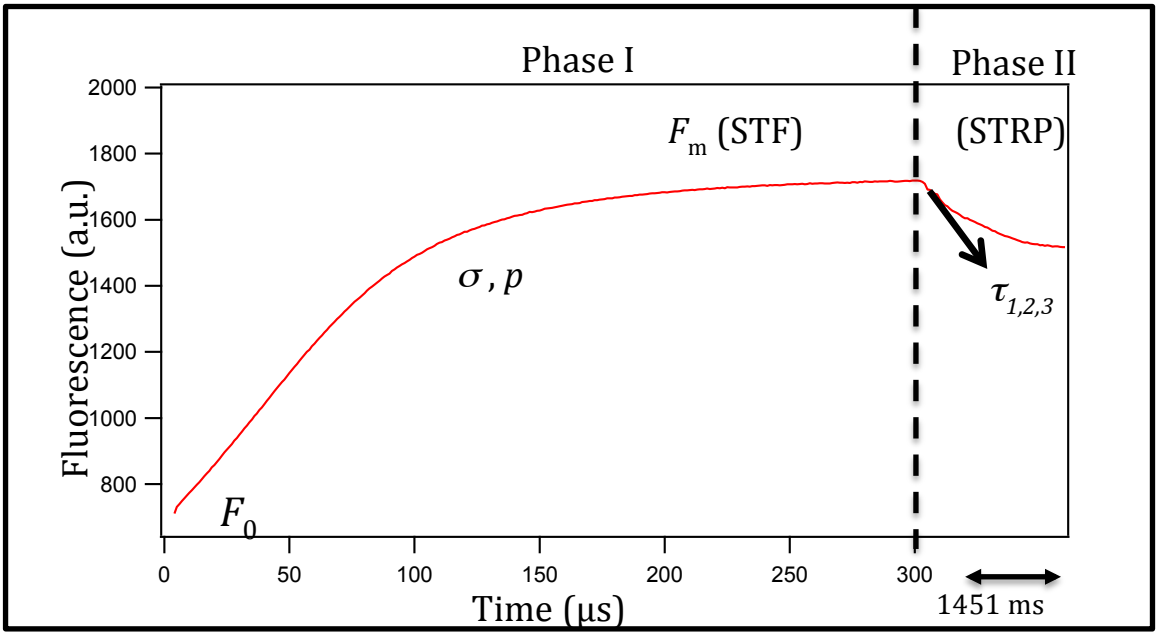

F_0 = Minimum fluorescence yield
F_m = Maximum fluorescence yield
F_v = Variable fluoresence yield (= $F_m - F_0$)
σ = Functional absorption cross-section

STF = Single turnover flash
STRP = Single turnover relaxation period
$t_{1,2,3}$ =Relaxation time constants
p = Connectivity

Figure A 7 | Typical FIRe output. The first phase is the variable fluorescence rise over 300 µs that will yield a single turnover of the reaction centers. The components are listed below the figure. Taking the Fv/Fm gives the quantum yield of photosynthesis.

A 3.5 - Electron Paramagnetic Resonance (EPR)

Paired electrons hold most of the atoms in biomolecules together. These molecules would have no net spin and thus no detectable interaction between electron spin and applied magnetic fields. Unpaired electrons occur much less frequently, and can be measured by Electron Paramagnetic Resonance (EPR). The physics behind this technique relates to the changes in electronic spin state populations caused by absorption of magnetic energy. [186]

In this study radical signals from Mn and singlet oxygen that are characteristic of water oxidation complex of PSII were investigated. The Boltzman distribution implies that at room temperature the populations of unpaired electron spins do not show measurable differences (+½ – ½). The EPR spectrum is related to the amount of energy that is required to separate the randomly distributed electron spins with an increasing magnetic field. The intensity of the EPR signal is proportional to the concentration of the paramagnetic species present in the sample. The width of the EPR signal is correlated to the relaxation time for the paramagnetic species to return to a randomized the spin state.

A 4. Electrochemical Techniques

Electrochemistry is the study of intercorrelating electrical and chemical effects. Many processes deal with electrical current needed or provided by a chemical process. The same basic instrumental setup can be used for measuring different electrochemical phenomena. These measurements look at processes and factors that are involved with the transport of charge across the interface between chemical phases. These phases are provided by an ionic conductor (e.g. electrolyte) and an electronic conductor (e.g. electrode). [9]

The instrument that is generally utilized for taking these types of measurements is known as a potentiostat-galvanostat or, more simply, potentiostat. The normal operation for the potentiostat involves a 3-electrode setup. The working electrode (WE), counter electrode (CE) and the reference electrode (RE). The potentiostat measures the current between the working and counter electrode while measuring the voltage between the working electrode and the reference electrode. Faraday's convention defines the electrodes so that oxidation occurs at the anode and reduction occurs at the cathode. Either electrode can work as the anode, or the cathode depending on the magnitude and the sign of the voltage applied to the system. [189] This study focused on some of the more common techniques including cyclic voltammetry (CV) a chronoamperometry (CA) as well as a special case of chronoamperometry for oxygen measurements.

A 4.1 - Chronoamperometry (CA)

Chronoamperometry (CA) allows for a direct measurement of the current that is generated by an electrochemical system. This is accomplished by observing the current on the WE as a function of time. The potentiostat will set the WE at a fixed polarization with respect to the RE, while the current is measured. In this study photo-chronoamperometry (pCA) was utilized to measure light-induced current generation. A light source illuminates the analyte coated on the surface of the WE and a photodriven current is observed. This is shown by turning on and off the light source and observing that the current signal output is directly photogenerated. Capacitive buildup in the system may be associates with a large current spike when light is turned on. This current signal does not reflect the true faradic signal from the sample. In summary, pCA measurements allow a direct observation of the generation of photodriven current.

A 4.2 - Cyclic Voltammetry (CV)

Cyclic voltammetry (CV) is a type of potential sweep electrochemical measurement where the electrical potential between WE and RE is varied independently between two fixed values and the corresponding current is observed. Cyclic voltammetry is a popular technique which can provide a wealth of kinetic and thermodynamic information about complex systems.[9] The standard CV experiment utilizes the 3-electrode setup. In this study the proteins under investigation were immobilized and oriented onto the WE. The potentiostat measures the current between the WE and the CE during the potential sweep. The CE is grounded. The potential is measured against the RE. The electrochemical cell used for the measurements as conducted generally require the use of an electrolyte solution in which WE, CE and RE are immersed CV is performed by sweeping potential between set values at a known sweep rate. (Fig A 8a) The initial potential (E_i) is set at a voltage where no reaction will occur. The potential is swept past a voltage where a redox reaction occurs (E_1). (Fig A 8b) Then the reverse sweep occurs, generally with a

symmetrical sweep speed, to observe the reverse reaction (E_1).

Figure A 8 - Electrochemical Measurements

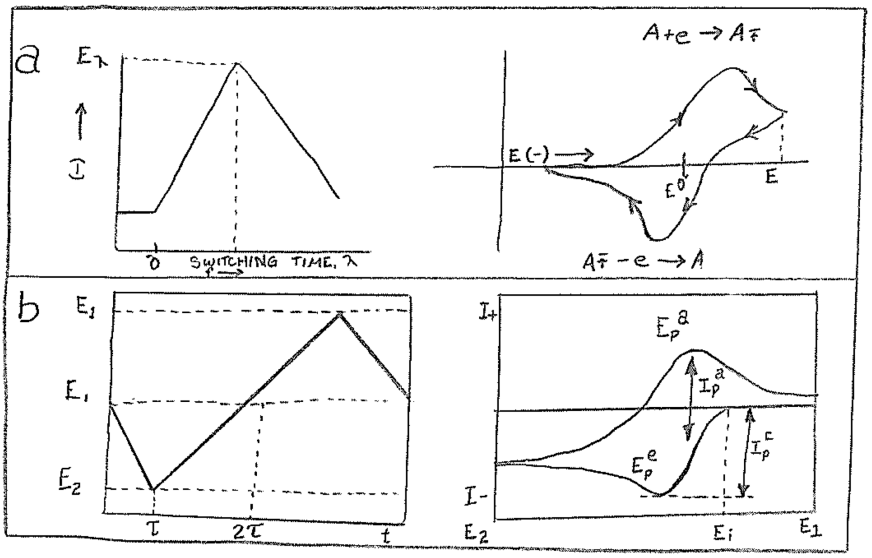

Figure A 8 | (a) shows the sweep rate for the voltage during the CV measurement with the corresponding CV trace. (b) Shows the voltage vs. time during the CV measurement with the corresponding typical CV trace.

The formal potential of a half reaction can be measured directly in CV. The parameters that are assigned to the characteristic shape of cyclic voltammograms is the (E_{pc}) cahodic and (E_{pa}) anodic peak potentials, (I_{pc}) cathodic and (I_{pa}) anodic peak currents ($E_{p/2}$) half peak potentials, and ($E_{½}$) half wave potential can be determined by $E_{½}$ (E_{pc}-E_{pa})/Ax. $E_{½}$ Is defined by Eq A 2.

$$E_{½} = E^{0\prime} + \frac{RT}{nF}\ln\left(\frac{D_R}{D_0}\right)^{½} \qquad \text{(Eq. A 2)}$$

Where $E^{0'}$ is defined as the formal for the ionic strength of the solution, D_0 and D_R are diffusion coefficients of the oxidized and reduced forms, the n is the number of exchanged electrons involved in the half reactions.[190] One of the useful features of CV is that redox reactions can be directly observed. The electron transfer is directly responsible for the change in the signal.

A 4.3 - Oxygen Evolution (Clark type electrode)

The oxygen was measured using an electrographic technique. The Clark-type electrode was introduced by the homonymous scientist in 1956. The Clark-type polarographic electrode is comprised of a Pt WE immersed in a KCl electrolyte solution to transport oxygen across a permeable membrane to an Ag cathode. [189] More in detail, the WE consists of a Pt cathode in the center of an epoxy resin disk. Surrounding that cathode is a well that has an Ag anode recessed into it. An electrolyte saturated paper wick is inserted to connect the cathode and anode. The electrolyte is a 50% saturated solution of KCl. The cell is capped with a polytetrafluoroethylene (PTFE) membrane held down by an O-ring. The electrolyte solution is trapped in a thin layer between the membrane and the electrode. This is the compartment where the electroreduction of the oxygen diffusing into the electrolyte occurs. The cathode is held at 600 mV and depolarized by the oxygen. In this system neither the cathode nor the anode is in direct contact with the solution being measured. [191] The Ag anode effectively acts an Ag/AgCl electrode, because AgCl is generated *in situ*. Freshly polishing electrodes will yield better results but will reduce the life of the platinum electrode. The reactions occurring are described in equations A 3a, A 3b, and A 3c.

Cathodic reaction: $O_2 + 2H_2O + 2e^- \rightarrow H_2O_2 + 2OH^-$: $2H_2O_2 + 2e^- \rightarrow 2OH^-$ (Eq. A 3a)

Anodic reaction: $Ag + Cl^- \rightarrow AgCl + e^-$ (Eq. A 3b)

Overall reaction: $4Ag + O_2 + 2H_2O + 4Cl^- \rightarrow 4AgCl + 4OH^-$ (Eq. A 3c)

The Clark-type electrode exhibits a linear response between current and oxygen content in the sample. The temperature will vary the measurement so it must be accurately controlled or accounted for. [191] The calibration of the system must be done at the temperature at which the measurement will occur. The oxygen reductions can follow 2 pathways.

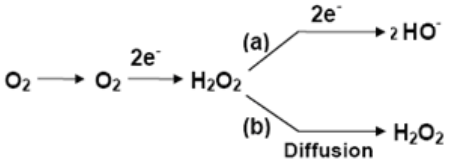

(Eq. A 4)

There is a 4-electron path and a 2-electron path (Eq. A 4). In the 4 electron path the oxygen diffuses to the surface cathode and is converted to hydroxyl by way of hydrogen peroxide. In the 2 electron pathway the intermediate peroxide diffuses directly out of the surface to the bulk solution. The oxygen path is dependent on the condition of the platinum electrode.

A 5. Surface techniques

Interfacing biological molecules to conducting supports can result in direct and indirect electron transfer. The resulting bioconjugate systems are amenable to surface probing techniques for studying the interface itself and the properties the attached molecules. The way that matter behaves at the interface of two phases can be different than in bulk. In the following description the biological molecules under investigation and their environment are identified.

A 5.1 - Atomic Force Microscopy (AFM)

Atomic Force Microscopy (AFM) is a scanning probe technique. Its application allows measurements of the morphology of the surface of a sample in a range from 0.1 nm to 50 nm in height, and from 10 nm to 30 μm horizontal size. The crucial part of the instrument consists of a cantilever that holds a tip in proximity of the sample. The cantilever can be electrically driven into constant oscillations above the sample. The incident light of a laser is reflects off the top of the cantilever to a photodetector. The photodetector is sensitive to the movement of the laser spot refection. As the tip approaches the sample surface the repulsive and attractive forces between the atoms on the surface of the sample and those of the tip dampen the oscillation of the cantilever. The cantilever is attached to a stack of piezoelectric panels in order to finely adjust the tip to react to the topographical features on the surface of the sample. In this way the tip remains in close proximity to the surface. The forces that are acting on the tip can be modeled by the Lennard-Jones force curve (V_{LJ}). The repulsive force term (r^{-12}) increases in response to the Pauli repulsion, while the attractive force term (r^{-6}) takes over at long ranges due to van der Walls forces. (Equation A 5 & figure A 9) ε is the depth of the potential well, σ is the finite distance where interparticle potential is zero, and r is the actual distance between particles.

$$V_{LJ} = 4\varepsilon \left[\left(\frac{\sigma}{r}\right)^{12} - \left(\frac{\sigma}{r}\right)^{6}\right] = \varepsilon \left[\left(\frac{r_m}{r}\right)^{12} - \left(\frac{r_m}{r}\right)^{6}\right] \quad \text{(Eq. A 5)}$$

Figure A 9 - Force curve of AFM tip with proximity to the surface

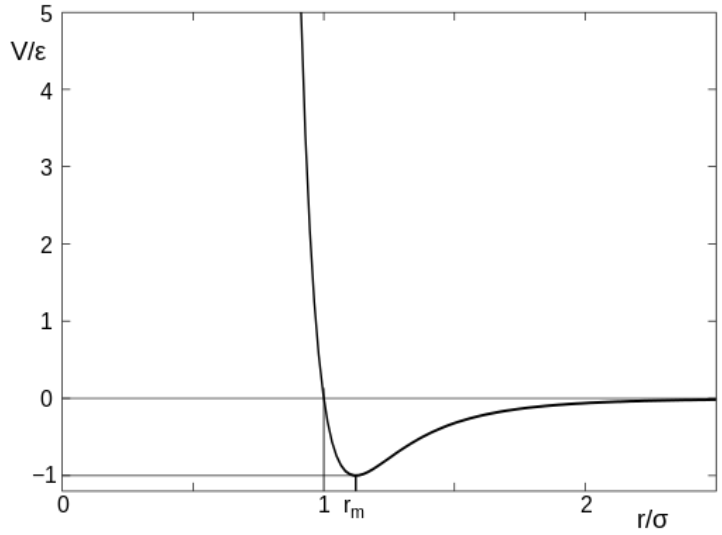

Figure A 9 | Force curve that is described in equation A 5 that shows the forces the AFM tip will experience as it comes in close proximity to the surface of the sample.

Figure A 10 – Diagram of AFM cantilever setup

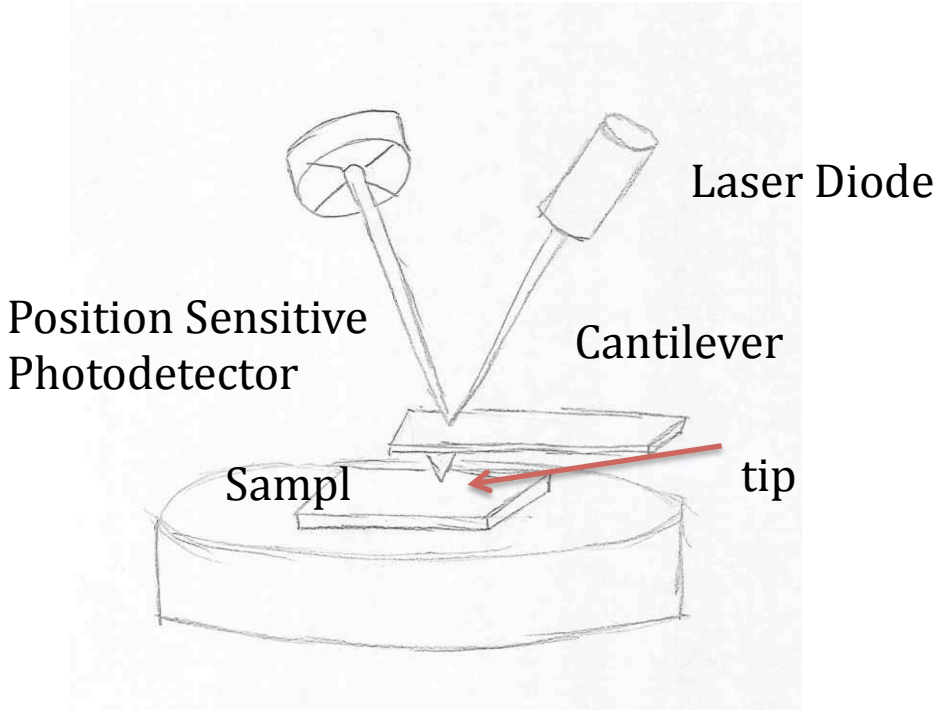

Figure A 10 | The AFM tip will move in response to the surface, the laser reflects off the cantilever to the photo detector to generate the topography of the sample.

A 5.2 - Quartz Crystal Microbalance (QCM)

Sauerbrey first described the quartz crystal microbalance in 1959. [192] Weighing monoatomic or thin layers as a function of area is possible by using quartz crystals. The fundamental principle behind the microbalance is the inverse proportion between oscillation frequency and mass. The microbalance utilizes the harmonic oscillation and natural frequency with respect to the mass.

$$f = \frac{V_{ir}}{2d} = \frac{N}{d} \qquad \text{(Eq. A 6)}$$

Where f is the natural frequency of the crystal, d is the plate thickness, v_{ir} is the propagation

velocity of elastic shear wave in the plate thickness direction, and N can be considered the frequency constant. As the mass changes on the surface of the quartz crystal the frequency will change. This change can be related to the mass by equation A 7.

$$\frac{\Delta f}{f} = -\frac{\Delta d}{d} = -\frac{\Delta m_Q}{\rho_Q \bullet F \bullet d} = -\frac{\Delta m}{\rho_Q \bullet F \bullet d} \qquad \text{(Eq. A 7)}$$

As in equation Ax.6 the factor *f* is the natural frequency of the quartz plate and d is the thickness of the quartz plate. The factor ρ_Q is the density of the quartz plate, F is the surface area of the quartz plate, and Δm_Q is the mass of a plane layer of thickness. The density, surface area, and thickness of the quartz crystal are intrinsic values. These are constant for any experiment preformed on that surface. And can be defined as C_f, which yields equation A 8.

$$\Delta f = -C_f \bullet \Delta m \qquad \text{(Eq. A 8)}$$

Where, Δ*f* is the frequency change observed (in Hz), Δm is the mass change per unit area (in g/cm^2), and C_f is the sensitivity factor for the crystal used (i.e. 56.6 Hz g^{-1} cm^2 for a 5MHz cut quartz crystal at room temperature.) The manufacturer provides this fundamental value of the substrate.

A 5.3 - X-ray Photoelectron Spectroscopy (XPS)

X-ray photoelectric spectroscopy is a widely used technique that interrogates the properties of atoms and molecules on surfaces. The fundamental principal behind this technique is the photoelectric effect. [193, 194] While there are other techniques that utilize this effect, XPS stands out as to the fact that when the energy of the x-ray is absorbed by the molecule or atom

an electron form the core will be ejected. The energy that is holding each electron in its position is the binding energy, which can also be referred to in this context as ionization potential. If the X-ray photon overcomes a threshold energy ($h\nu$), and does not collide with another atom in the sample, then the core electron will be ejected and leave the surface. Electrons that are excited from deeper levels to the surface may be impacted by inelastic collisions. This phenomenon is the source of background noise and must be subtracted from controls. The electron will have a kinetic energy of E_k and referred to as the photoelectron.

The Einstein relationship provides the binding energy of the core electron and is given by equations A 9a and A 9b

$$h\nu = E_b + E_k + \Phi \qquad \text{(Eq A 9a)}$$

$$E_b = h\nu - E_k - \Phi \qquad \text{(Eq A 9b)}$$

where $h\nu$ is the X-ray photon energy and E_k is the kinetic energy of photoelectron, which can be measured by the energy analyzer, and Φ is the work function of the atom induced by the analyzer. The work function (Φ) can be eliminated by compensating for it with the instrument. The resulting formula for binding energy is:

$$E_b = h\nu - E_k \qquad \text{(Eq A 10)}$$

Figure A 11 – An incoming photon causes the ejection of the photoelectron

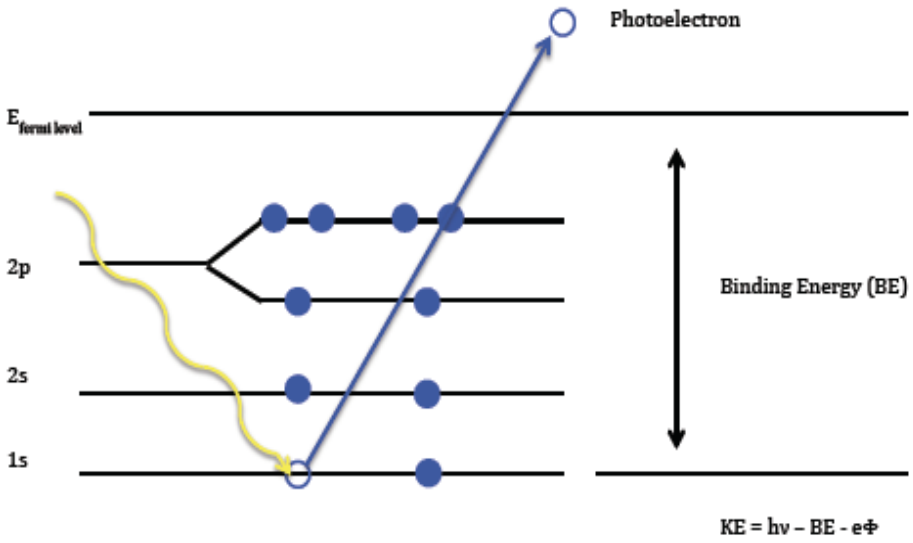

Each atom will have a characteristic binding energy level, which is used to identify the type of atoms the measured electrons were emitted from. The molecular bonds in the valence levels will slightly shift the binding energy of the core electrons in a predictable manner. Therefore, information about the molecular structure can be obtained. [186, 195]

Appendix B - Methods

B 1. Photosystem II core complex purification

The purification protocol was modified from Sugiura and Inoue. [95] The buffers are listed in table A.1 *T. elongatus* containing a His6 tag on the CP_{47} subunit was grown to an optical density of 1.0 A.U at 800 nm with 80µE/m^2 of light at 45˚C with 1% CO_2. The typical volume of culture was 16L. These cells were pelleted by centrifugation at 7300 x g in a GS3 rotor and the supernatant was discarded. The pellets were resuspended in TP2 and centrifuged in a SS-34 rotor at 6700 x g for 10 min. The supernatant was discarded, and the rest of the protocol must be conducted in the dark and on ice or in a 4˚C environmental chamber. The cells were broken by using a French press. The cells were resuspended in 50-100 mL of TP2 containing a 1mM final concentrations of Aminocaproic acid, Benzamidine, a 0.2%, Bovine Serum Albumin (BSA), and a spatula tip of DNAse. This mixture was gently shaken and the cells were broken at pressure of 700 psi. The resulting crude mixture was centrifuged at 1450 x g in SS-34 rotor and 4˚C for 5 minutes to remove unbroken cells. The supernatant was collected and spun for 30 min at 4˚C at a speed of 50,000 RPM in a 70Ti rotor. The supernatant was discarded and the pellet was resuspended in TP2, and centrifuge again at 50,000 RPM in a 70Ti rotor at 4˚C. The supernatant was discarded and the pelleted thylakoids were resuspended in TP2.

To the resuspended thylakoids, sufficient 10% (w/v) DDM in TP2 (prepared at least one hour before use) was added to bring the DDM concentration to 1% followed by the addition of 4 M NaCl to a final concentration of 100 mM. The detergent solubilization was performed for ~1 min on a vortex mixer, avoiding excessive mixing which results in loss of PSII activity. After centrifugation for at 256,000 x g in a 70Ti rotor, the supernatant was mixed with Invitrogen ProBond NiNTA resin in TP3, adjusting to 1 mg of protein per mL of resin. The charged resin was

introduced into a chromatography column and the phases were allowed to separate before opening the outflow. The column was checked every 10 min to assure that it did not run dry. After collection of the initial flow through, the Chl *a* concentration was checked to monitor PSII binding and elution was performed with TP4 overnight to remove material not binding to the column, consisting mainly of PSI and the b_6f complex. Care was taken in calculating the time and flow volume. The bound PSII was removed by washing the column with TP5 at a rate of 4 mL/min. The PSII should eluted at this high imidazole concentration , allowing collection of the His-tagged complex. This can be confirmed by the Chl *a* concentration assay. The fractions were pooled and concentrated using Amicon 100 kDa centrifugation filters at 4˚C. The concentrated samples were brought to an ideal concentration of about 1mg protein/mL, quickly aliquoted and stored under liquid nitrogen.

Table B.1 Buffers for Photosystem II purification

PSII Purification Buffers

TP2:
40 mM MES pH 6.5
15 mM $MgCl_2$
15 mM $CaCl_2$
10% (w/v) glycerol
1M Betaine

TP3:
40 mM MES pH 6.5
15 mM $MgCl_2$
15 mM $CaCl_2$
100 mM NaCl
10% (w/v) glycerol
1M Betaine

TP4:
50 mM MES pH 6.5
15 mM $MgCl_2$
15 mM $CaCl_2$
100 mM NaCl
15 mM Imidazole
10% (w/v) glycerol
1M Betaine

TP5:
150 mM MES pH 6.5
15 mM $MgCl_2$
15 mM $CaCl_2$
200 mM NaCl
0.1% (w/v) Dodecyl Maltoside
300 mM Imidazole
10% (w/v) glycerol
1M Betaine

TP6:
40 mM MES pH 6.5
15 mM $MgCl_2$
15 mM $CaCl_2$
20% glycerol
1M Betaine

B 2. Graphene Oxide and Affinity Chromatography.

Affinity Chromatography relies in specific interaction between protein molecules in the mobile phase with the stationary phase. These specific interactions include immunoglobulin (IgG) interacting with immobilized protein A or protein G, protein domain such as streptavidin interacting with immobilized biotin, maltose binding protein (MBP) interacting with immobilized sugar, and peptide or peptide sequence often a poly Histidine tag that interacts with an immobilized metal ion (including Ni^{2+}, Cu^{2+}, Zn^{2+}, Ag^{+}, Fe^{3+}, Ga^{3+}, Zr^{3+}, and Co^{2+}) commonly often referred to as immobilized metal affinity chromatography (IMAC).[165] IMAC purification offers

high protein-loading capacities with mild elution conditions, stability of the ligand, and relatively low cost. [165] [166] The metal is immobilized by a tri-dentate nitrilotriacetic acid (NTA) that is attached to the support. Although the metal ion has affinity for many amino acid residues including glutamine, tyrosine, arginine, methionine, and lysine, but it is the histidine that correlates with the binding of protein to the stationary phase the most. Aromatic side chains (phenylalanine, tryptophan, tyrosine) can contribute to the binding if they are in proximity of the contributing histidine. In rare cases cysteines can contribute to binding of the protein if they are freely available and in the reduced state. [166, 170] Proteins with several native histidines can be purified without additional modification and utilized for analysis and medicine without further modification. This was the original use for the technology.[165] This technique is often used to isolate a particular protein that has been specifically altered to contain the poly histidine tag, generally 6, that will interact with stationary phase. [168, 169] IMAC resins are typically comprised of polymeric matrixes based on polysaccharides such as agarose and sepharose.

Bound proteins can be eluted from the stationary phase by using a high imidazole concentration that mimics the side chain of histidine, low pH, or a chelating agent such as EDTA. In this study initially the mobile phase had low concentrations of imidazole to reduce nonspecific binding of naturally occurring histidines. [170, 196] High imidazole concentration necessary to elute bound proteins often results in the metal ion being washed away from the stationary phase. Therefore resin must be recharged with the metal ions prior to reuse of the resin. Often analysis of these proteins requires a very high degree of purity for applications such as crystallography. For these techniques multiple steps after the IMAC purification process are required. Many more proteins are often co-eluted with the protein of interest in this technique.[165] Nonspecific binding interferes with the purity of the recovered protein. Typically the IMAC purification step yields a 20-50% pure sample of protein. [166] This leads to further

purification of the protein utilizing techniques such as ion exchange or size exclusion.

A side task of this study has been to develop and standardize a new IMAC resin based on graphene[54] to be used in isolation of affinity proteins. Most resins are based on a polysaccharide matrix such as agarose or spepharose. This study introduces a Ni-NTA made by modifying graphene oxide (GO). This scaffold provides a better separation at a lower cost, higher affinity to be used in separations of target proteins.

Graphene is a thin sheet of SP^2 hybridized carbon. This elemental form of carbon starts out as a 3-dimensional lattice called graphite where these graphene sheets are stacked on top of one another. [51, 52, 54, 55, 197, 198] When the graphite is separated from the lattice it is thought of as 2- dimensional due to the large aspect ratio of 10,000 – 200,000 (0.5 to 10 μm width/depth to the monoatomic 0.5 Å height). The nature of graphene leads the current interest in its being incorporated into many new applications. The high degree of biocompatibility will continue to be integrated into biotechnology applications well into the future. [199-209]

B 2.1 GO Resin Synthesis

Graphene oxide was obtained from Prof. Chhowalla in Rutgers Material Science Department. The GO was synthesized by a modified Hummers method of graphene exfoliation.[197] The graphene was then modified to contain a NiNTA linker.

Figure B 1 – GO-NiNTA sythesis

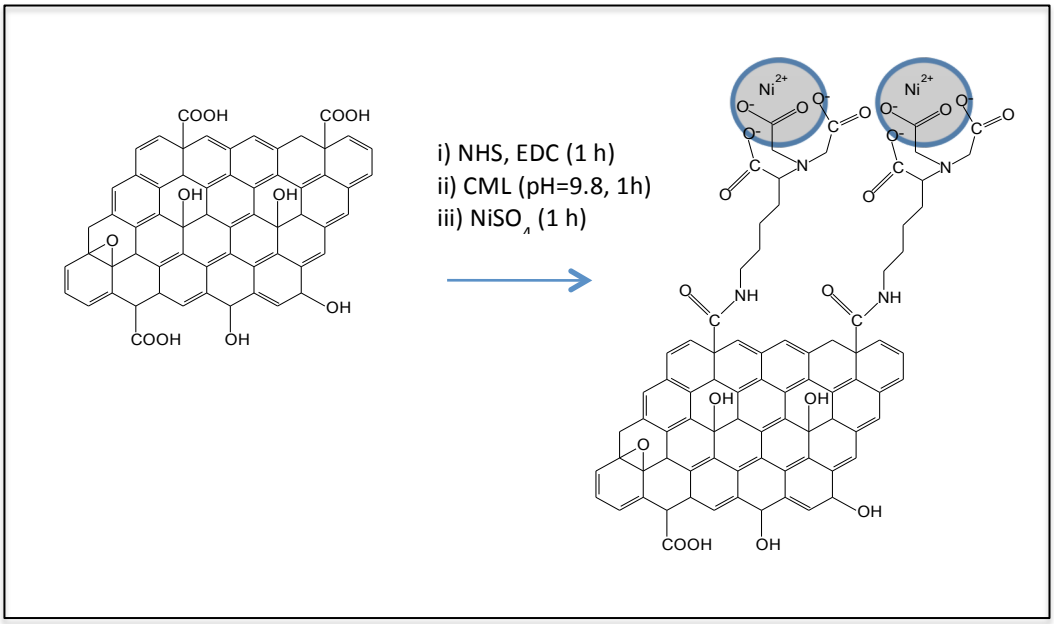

Figure B 1 | A schematic representation of the modification of graphene oxide to contain a nickel containing Nitrilotriacetic acid functional group that can bind to histidine residues of proteins.

The initial aqueous GO suspension was precipitated by taking 5 mL of GO suspension and spinning at 100,000 x g for 9 min. The sample was resuspended in an eppendorf tube with 1 mL of ultrapure water. Then 130uL of 100mM N-ethyl-N'-(3-dimethylaminopropyl)carbodiimide (EDC) (Sigma-Aldrich #39391), 100mM N-hydroxysuccinimide (NHS) (Sigma-Aldrich #130672) (10X) was added to the reaction mixture. The sample was incubated in the dark for 1 hour while shaking on a low vortex setting. To wash, the sample was spun at 10,000 x g for 5 min in eppendorf tube bench top centrifuge. The supernatant was removed, and using a bath sonicator, sonicated for 5 min. This washing procedure was repeated 3 times in ultra-pure water. Then 130 µL of the resulting GO-NHS ester was added to 1 mL of N_{α},N_{α}-

Bis(carboxmethyl)-L-lysine hydrate (Sigma-Aldrich #14580) pH buffered to 9.8 in 0.5M K_2CO_3 (CML) solution. The sample was incubated in the dark for 1 hour while shaking on a low vortex setting. To wash, the sample was spun at 10,000 x g for 5 min in bench top centrifuge (Eppendorf). The supernatant was removed, and sonicated for 5 min. Three washes were performed with ultra-pure water. The final washed pellet was resuspended in in 1 mL of 150 mM $NiSO_4$ solution. The sample was incubated the dark for 1 hour while shaking on a low vortex setting. Three washes followed, as described above. Final pellet was resuspended in 1 ml of milliQ water. This material we refer to as 1X resin that provided 25% slurry of solids in the suspension.

This resin was kept at 4C˚ in the dark. After about 6 months clumping was noticed to form in the suspension in water when charged with nickel. The material was discontinued after these clumps were found. This helped with consistency of the results.

B 2.2 - Protein Loading

Protein loading was determined by UV absorbance and flow cytometry techniques. (PSII) CCs containing a polyhistidine tag were used to determine the protein loading. The PSII was added to a 1.5 mL eppendorf tube containing GO resin at a 1X concentration (volume of settled resin). The sample was diluted to 1 mL with a detergent-containing buffer (DCB). The DCB buffer contained 20 mM MES, 10 mM $MgCl_2$, 10 mM $CaCl_2$ and 0.03 % (w/v) ß-dodecylmaltoside. The sample was then mixed in the dark at 4˚C for 1 hour on a low vortex setting, and washed at room temperature by spinning down in a bench top centrifuge at 10,000 x g for 5 min. The supernatant was the removed and the chlorophyll a content was examined by absorbance spectroscopy. The GO-PSII pellet was resuspended in 1 mL of DCB and washed 3 more times. The final washed GO-PSII pellet was resuspended to 1 mL and analyzed.

B 2.3 – Spectroscopic Chlorophyll Quantification

A spectroscopic absorbance method was used to determined PSII concentration and thus the capacity of the GO resin. A 5µL sample of the PSII-GO was removed from the mixture and added to 995 µL of a 1:1 mixture of acetone and methanol. This mixture will extract the chlorophyll from the PSII CCs. The absorbance is measured against a blank at 665 nm. The concentration is determined in mg/mL of chlorophyll a (Chl a) by using Equation 3.1.

$$\frac{OD_{665} \bullet Dil.}{\varepsilon} = Chl.a.mg/mL \qquad \text{(Eq. B 1)}$$

Where OD_{665} is the optical density of absorbance at 665 nm and Dil. is the dilution factor. (200 for 5/995) The factor ε is the extinction coefficient 79.5. [210]

Works Cited

1. Donohue, T. J., and Cogdell, R. J. (2006) Microorganisms and clean energy, *Nature Reviews. Microbiology 4*, 800.
2. Falkowski, P. G., and Raven, J. A. (2013) *Aquatic photosynthesis*, Princeton University Press.
3. Collings, A. F., and Critchley, C. (2005) *Artificial Photosynthesis: From Basic Biology to Industrial Application*, WILEY-VCH Verlag GmbH & Co. KGaA, Weinheim.
4. McKendry, P. (2002) Energy production from biomass (part 1): overview of biomass, *Bioresource technology 83*, 37-46.
5. McKendry, P. (2002) Energy production from biomass (part 2): conversion technologies, *Bioresource technology 83*, 47-54.
6. Woronowicz, K., Ahmed, S., Biradar, A. A., Biradar, A. V., Birnie, D. P., Asefa, T., and Niederman, R. A. (2012) Near-IR Absorbing Solar Cell Sensitized With Bacterial Photosynthetic Membranes, *Photochemistry and Photobiology 88*, 1467-1472.
7. Walter, M. G., Warren, E. L., McKone, J. R., Boettcher, S. W., Mi, Q., Santori, E. A., and Lewis, N. S. (2010) Solar Water Splitting Cells, *Chemical Reviews 110*, 6446-6473.
8. Rajeshwar, K., McConnell, R. D., and Licht, S. (2008) *Solar hydrogen generation*, Springer.
9. Bard, A. J., and Faulkner, L. R. (2001) Electrochemical methods: fundamentals and applications, 2nd, *Hoboken: Wiley and Sons*.
10. Bolton, J. R., and HALL, D. O. (1991) The maximum efficiency of photosynthesis*, *Photochemistry and Photobiology 53*, 545-548.
11. Badura, A., Esper, B., Ataka, K., Grunwald, C., Wöll, C., Kuhlmann, J., Heberle, J., and Rögner, M. (2006) Light-Driven Water Splitting for (Bio-)Hydrogen Production: Photosystem 2 as the Central Part of a Bioelectrochemical Device, *Photochemistry and Photobiology 82*, 1385-1390.
12. Barber, J., and Tran, P. D. (2013) From natural to artificial photosynthesis, *Interface 10*, 20120984.
13. Ferreira, K. N., Iverson, T. M., Maghlaoui, K., Barber, J., and Iwata, S. (2004) Architecture of the photosynthetic oxygen-evolving center, *Science 303*, 1831-1838.
14. Boichenko, V. A., Hou, J.-M., and Mauzerall, D. (2001) Thermodynamics of Electron Transfer in Oxygenic Photosynthetic Reaction Centers: Volume Change, Enthalpy, and Entropy of Electron-Transfer Reactions in the Intact Cells of the Cyanobacterium Synechocystis PCC 6803, *Biochemistry 40*, 7126-7132.
15. Guskov, A., Kern, J., Gabdulkhakov, A., Broser, M., Zouni, A., and Saenger, W. (2009) Cyanobacterial photosystem II at 2.9-Å resolution and the role of quinones, lipids, channels and chloride, *Nature structural & molecular biology 16*, 334-342.
16. Ido, K., Gross, C. M., Guerrero, F., Sedoud, A., Lai, T.-L., Ifuku, K., William Rutherford, A., and Krieger-Liszkay, A. (2011) High and low potential forms of the Q< sub> A</sub> quinone electron acceptor in Photosystem II of< i> Thermosynechococcus elongatus</i> and spinach, *Journal of Photochemistry and Photobiology B: Biology 104*, 154-157.
17. Renger, T., and Schlodder, E. (2011) Optical properties, excitation energy and primary charge transfer in photosystem II: Theory meets experiment, *Journal of Photochemistry and Photobiology B: Biology 104*, 126-141.
18. Zech, S. G., Kurreck, J., Renger, G., Lubitz, W., and Bittl, R. (1999) Determination of the distance between Y (Z) ox* and QA-* in photosystem II by pulsed EPR spectroscopy on light-induced radical pairs, *FEBS letters 442*, 79-82.
19. Chen, G. X., Blubaugh, D. J., Homann, P. H., Golbeck, J. H., and Cheniae, G. M. (1995) Superoxide contributes to the rapid inactivation of specific secondary donors of the

photosystem II reaction center during photodamage of manganese-depleted photosystem II membranes, *Biochemistry 34*, 2317-2332.
20. Faller, P., Debus, R. J., Brettel, K., Sugiura, M., Rutherford, A. W., and Boussac, A. (2001) Rapid formation of the stable tyrosyl radical in photosystem II, *Proceedings of the National Academy of Sciences of the United States of America 98*, 14368-14373.
21. Barber, J. (2007) Biological solar energy, *Philosophical transactions. Series A, Mathematical, physical, and engineering sciences 365*, 1007-1023.
22. Mamedov, F., Nowaczyk, M. M., Thapper, A., Rögner, M., and Styring, S. (2007) Functional characterization of monomeric photosystem II core preparations from Thermosynechococcus elongatus with or without the Psb27 protein, *Biochemistry 46*, 5542-5551.
23. Busch, A., and Hippler, M. (2011) The structure and function of eukaryotic photosystem I, *Biochim. Biophys. Acta-Bioenerg. 1807*, 864-877.
24. Jordan, P., Fromme, P., Witt, H. T., Klukas, O., Saenger, W., and Krauss, N. (2001) Three-dimensional structure of cyanobacterial photosystem I at 2.5 angstrom resolution, *Nature 411*, 909-917.
25. Remy, A., Niklas, J., Kuhl, H., Kellers, P., Schott, T., Rogner, M., and Gerwert, K. (2004) FTIR spectroscopy shows structural similarities between photosystems II from cyanobacteria and spinach, *Eur. J. Biochem. 271*, 563-567.
26. Klauss, A., Krivanek, R., Dau, H., and Haumann, M. (2009) Energetics and kinetics of photosynthetic water oxidation studied by photothermal beam deflection (PBD) experiments, *Photosynthesis research 102*, 499-509.
27. Klukas, O., Schubert, W. D., Jordan, P., Krauss, N., Fromme, P., Witt, H. T., and Saenger, W. (1999) Photosystem I, an improved model of the stromal subunits PsaC, PsaD, and PsaE, *J. Biol. Chem. 274*, 7351-7360.
28. El-Mohsnawy, E., Kopczak, M. J., Schlodder, E., Nowaczyk, M., Meyer, H. E., Warscheid, B., Karapetyan, N. V., and Rogner, M. (2010) Structure and Function of Intact Photosystem 1 Monomers from the Cyanobacterium Thermosynechococcus elongatus, *Biochemistry 49*, 4740-4751.
29. Falzone, C. J., Kao, Y. H., Zhao, J. D., Bryant, D. A., and Lecomte, J. T. J. (1994) 3-Dimensional Solution Structure of Psae from the Cyanobacterium Synechococcus Sp Strain Pcc-7002, a Photosystem-I Protein That Shows Structural Homology with Sh3 Domains, *Biochemistry 33*, 6052-6062.
30. Carmeli, I., Mangold, M., Frolov, L., Zebli, B., Carmeli, C., Richter, S., and Holleitner, A. W. (2007) A Photosynthetic Reaction Center Covalently Bound to Carbon Nanotubes, *Adv. Mater. 19*, 3901.
31. Das, R., Kiley, P. J., Segal, M., Norville, J., Yu, A. A., Wang, L., Trammell, S. A., Reddick, L. E., Kumar, R., Stellacci, F., Lebedev, N., Schnur, J., Bruce, B. D., Zhang, S., and Baldo, M. (2004) Integration of Photosynthetic Protein Molecular Complexes in Solid-State Electronic Devices, *Nano Lett 4*, 1079-1083.
32. Sepunaru, L., Tsimberov, I., Forolov, L., Carmeli, C., Carmeli, I., and Rosenwaks, Y. (2009) Picosecond Electron Transfer from Photosynthetic Reaction Center Protein to GaAs, *Nano Lett 9*, 2751-2755.
33. Utschig, L. M., Dimitrijevic, N. M., Poluektov, O. G., Chemerisov, S. D., Mulfort, K. L., and Tiede, D. M. (2011) Photocatalytic Hydrogen Production from Noncovalent Biohybrid Photosystem I/Pt Nanoparticle Complexes, *J. Phys. Chem. Lett. 2*, 236-241.
34. Greenbaum, E. (1985) Platinized chloroplasts: a novel photocatalytic material, *Science 230*, 1373-1375.

35. Grimme, R. A., and Golbeck, J. H. (2010) A Biologically-Inspired Electrochemical Half-Cell for Light-Driven Generation of Hydrogen, *Material Matters 3*, 78-81.
36. Grimme, R. A., Lubner, C. E., Bryant, D. A., and Golbeck, J. H. (2008) Photosystem I/molecular wire/metal nanoparticle bioconjugates for the photocatalytic production of H2, *Journal of the American Chemical Society 130*, 6308-6309.
37. Grimme, R. A., Lubner, C. E., and Golbeck, J. H. (2009) Maximizing H2 production in Photosystem I/dithiol molecular wire/platinum nanoparticle bioconjugates, *Dalton Transactions*, 10106-10113.
38. Lubner, C. E., Heinnickel, M., Bryant, D. A., and Golbeck, J. H. (2011) Wiring photosystem I for electron transfer to a tethered redox dye, *Energy Environ. Sci. 4*, 2428-2434.
39. Lubner, C. E., Knorzer, P., Silva, P. J. N., Vincent, K. A., Happe, T., Bryant, D. A., and Golbeck, J. H. (2010) Wiring an FeFe -Hydrogenase with Photosystem I for Light-Induced Hydrogen Production, *Biochemistry 49*, 10264-10266.
40. Ohad, I., Berg, A., Berkowicz, S. M., Kaplan, A., and Keren, N. (2011) Photoinactivation of photosystem II: is there more than one way to skin a cat?,, *Physiologia Plantarum 142*, 79-86.
41. Takahashi, S., and Badger, M. R. (2011) Photoprotection in plants: a new light on photosystem II damage, *Trends in Plant Science 16*, 53-60.
42. Vass, I. (2011) Role of charge recombination processes in photodamage and photoprotection of the photosystem II complex, *Physiologia Plantarum 142*, 6-16.
43. Magis, G. J., den Hollander, M. J., Onderwaater, W. G., Olsen, J. D., Hunter, C. N., Aartsma, T. J., and Frese, R. N. (2010) Light harvesting, energy transfer and electron cycling of a native photosynthetic membrane adsorbed onto a gold surface, *Biochim. Biophys. Acta-Biomembr. 1798*, 637-645.
44. Sturgis, J. N., Hunter, C. N., and Niederman, R. A. (1988) Spectra and Extinction coefficents of Near-infrared Absorbance-bands in Membrance of Rhodobacter-sphaeroides Mutants Lacking Light-harvesting and Reaction Center Complexes, *Photochemistry and Photobiology 48*, 243-247.
45. Hu, X. C., Ritz, T., Damjanovic, A., Autenrieth, F., and Schulten, K. (2002) Photosynthetic apparatus of purple bacteria, *Q. Rev. Biophys. 35*, 1-62.
46. Bosshard, H. R., Wynn, R. M., and Knaff, D. B. (1987) Binding-Site on Rhodospirillum-Rubrum Cytochrome-C2 for the Rhodospirillum-Rubrum Cytochrome-Bc1 Complex, *Biochemistry 26*, 7688-7693.
47. Agostiano, A., Ceglie, A., and Della Monica, M. (1984) Water photoelectrolysis through the use of electrodes covered by photosystems I and II, *Bioelectrochemistry and Bioenergetics 12*, 499-507.
48. Lee, J. W., Lee, I., and Greenbaum, E. (1996) Platinization: a novel technique to anchor photosystem I reaction centres onto a metal surface at biological temperature and pH, *Biosensors and Bioelectronics 11*, 375-387.
49. Lubner, C. E., Grimme, R., Bryant, D. A., and Golbeck, J. H. (2009) Wiring Photosystem I for Direct Solar Hydrogen Production, *Biochemistry 49*, 404-414.
50. Chilkoti, A., and Hubbell, J. A. (2005) Biointerface science, *Mrs Bull 30*, 175-179.
51. Stankovich, S., Dikin, D. A., Dommett, G. H., Kohlhaas, K. M., Zimney, E. J., Stach, E. A., Piner, R. D., Nguyen, S. T., and Ruoff, R. S. (2006) Graphene-based composite materials, *Nature 442*, 282-286.
52. Novoselov, K. S., Geim, A. K., Morozov, S., Jiang, D., Zhang, Y., Dubonos, S., Grigorieva, I., and Firsov, A. (2004) Electric field effect in atomically thin carbon films, *Science 306*, 666-669.

53. Eda, G., Fanchini, G., and Chhowalla, M. (2008) Large-area ultrathin films of reduced graphene oxide as a transparent and flexible electronic material, *Nature nanotechnology 3*, 270-274.
54. Eda, G., and Chhowalla, M. (2009) Graphene-based composite thin films for electronics, *Nano Lett 9*, 814-818.
55. Eda, G., Mattevi, C., Yamaguchi, H., Kim, H., and Chhowalla, M. (2009) Insulator to semimetal transition in graphene oxide, *The Journal of Physical Chemistry C 113*, 15768-15771.
56. Pham, T. A., Choi, B. C., Lim, K. T., and Jeong, Y. T. (2011) A simple approach for immobilization of gold nanoparticles on graphene oxide sheets by covalent bonding, *Applied Surface Science 257*, 3350-3357.
57. Goncalves, G., Marques, P. A. A. P., Granadeiro, C. M., Nogueira, H. I. S., Singh, M. K., and Grácio, J. (2009) Surface Modification of Graphene Nanosheets with Gold Nanoparticles: The Role of Oxygen Moieties at Graphene Surface on Gold Nucleation and Growth, *Chemistry of Materials 21*, 4796-4802.
58. Yamaguchi, H., Murakami, K., Eda, G., Fujita, T., Guan, P., Wang, W., Gong, C., Boisse, J., Miller, S., Acik, M., Cho, K., Chabal, Y. J., Chen, M., Wakaya, F., Takai, M., and Chhowalla, M. (2011) Field Emission from Atomically Thin Edges of Reduced Graphene Oxide, *ACS Nano 5*, 4945-4952.
59. Gorbunov, M. Y., and Falkowski, P. G. (2005) Fluorescence Induction and Relaxation (FIRe) Technique and Instrumentation for Monitoring Photosynthetic Processes and Primary Production in Aquatic Ecosystems., In *Photosynthesis: Fundamental Aspects to Global Perspectives* (van der Est, A. B., D., Ed.), pp 1029-1031, Allen Press, Lawrence KS USA.
60. Biczo, R., and Hirsh, D. J. (2009) Structure and Dynamics of a DNA-based Model System for the Study of Electron Spin-Spin Interactions, *Journal of Inorganic Biochemistry 103*, 362-372.
61. Ananyev, G. M., and Dismukes, G. C. (1996) High-resolution kinetic studies of the reassembly of the tetra-manganese cluster of photosynthetic water oxidation: proton equilibrium, cations, and electrostatics, *Biochemistry 35*, 4102-4109.
62. Bagri, A., Mattevi, C., Acik, M., Chabal, Y. J., Chhowalla, M., and Shenoy, V. B. (2010) Structural evolution during the reduction of chemically derived graphene oxide, *Nature Chemistry 2*, 581-587.
63. Vittadello, M., Gorbunov, M. Y., Mastrogiovanni, D. T., Wielunski, L. S., Garfunkel, E. L., Guerrero, F., Kirilovsky, D., Sugiura, M., Rutherford, A. W., Safari, A., and Falkowski, P. G. (2010) Photoelectron Generation by Photosystem II Core Complexes Tethered to Gold Surfaces, *ChemSusChem 3*, 471-475.
64. Nelson, N. (2011) Photosystems and global effects of oxygenic photosynthesis, *Biochim. Biophys. Acta-Bioenerg. 1807*, 856-863.
65. McEvoy, J. P., Gascon, J. A., Batista, V. S., and Brudvig, G. W. (2005) The mechanism of photosynthetic water splitting, *Photochemical & Photobiological Sciences 4*, 940-949.
66. Renger, G., and Renger, T. (2008) Photosystem II: The machinery of photosynthetic water splitting, *Photosynth. Res. 98*, 53-80.
67. Esper, B., Badura, A., and Rogner, M. (2006) Photosynthesis as a power supply for (bio-)hydrogen production, *Trends in Plant Science 11*, 543-549.
68. Trammell, S. A., Griva, I., Spano, A., Tsoi, S., Tender, L. M., Schnur, J., and Lebedev, N. (2007) Effects of Distance and Driving Force on Photoinduced Electron Transfer between Photosynthetic Reaction Centers and Gold Electrodes, *The Journal of Physical Chemistry C 111*, 17122-17130.

69. Trammell, S. A., Spano, A., Price, R., and Lebedev, N. (2006) Effect of protein orientation on electron transfer between photosynthetic reaction centers and carbon electrodes, *Biosensors and Bioelectronics 21*, 1023-1028.
70. Trammell, S. A., Wang, L., Zullo, J. M., Shashidhar, R., and Lebedev, N. (2004) Orientated binding of photosynthetic reaction centers on gold using Ni-NTA self-assembled monolayers, *Biosensors and Bioelectronics 19*, 1649-1655.
71. Mukherjee, D., May, M., and Khomami, B. (2011) Detergent-protein interactions in aqueous buffer suspensions of Photosystem I (PS I), *Journal of Colloid and Interface Science 358*, 477-484.
72. Carmeli, I., Frolov, L., Carmeli, C., and Richter, S. (2007) Photovoltaic activity of photosystem I-based self-assembled monolayer, *Journal of the American Chemical Society 129*, 12352-12353.
73. Carmeli, I., Lieberman, I., Kraversky, L., Fan, Z. Y., Govorov, A. O., Markovich, G., and Richter, S. (2010) Broad Band Enhancement of Light Absorption in Photosystem I by Metal Nanoparticle Antennas, *Nano Lett 10*, 2069-2074.
74. Carmeli, I., Mangold, M., Frolov, L., Zebli, B., Carmeli, C., Richter, S., and Holleitner, A. W. (2007) A Photosynthetic Reaction Center Covalently Bound to Carbon Nanotubes, *Adv. Mater. 19*, 3901–3905.
75. Ciesielski, P. N., Cliffel, D. E., and Jennings, G. K. (2011) Kinetic Model of the Photocatalytic Effect of a Photosystem I Monolayer on a Planar Electrode Surface, *The Journal of Physical Chemistry A 115*, 3326-3334.
76. Ciesielski, P. N., Faulkner, C. J., Irwin, M. T., Gregory, J. M., Tolk, N. H., Cliffel, D. E., and Jennings, G. K. (2010) Enhanced Photocurrent Production by Photosystem I Multilayer Assemblies, *Advanced Functional Materials 20*, 4048-4054.
77. Ciesielski, P. N., Hijazi, F. M., Scott, A. M., Faulkner, C. J., Beard, L., Emmett, K., Rosenthal, S. J., Cliffel, D., and Jennings, G. K. (2010) Photosystem I - Based biohybrid photoelectrochemical cells, *Bioresource Technology 101*, 3047-3053.
78. Ciesielski, P. N., Scott, A. M., Faulkner, C. J., Berron, B. J., Cliffel, D. E., and Jennings, G. K. (2008) Functionalized Nanoporous Gold Leaf Electrode Films for the Immobilization of Photosystem I, *Acs Nano 2*, 2465-2472.
79. Ciobanu, M., Kincaid, H. A., Jennings, G. K., and Cliffel, D. E. (2005) Photosystem I patterning imaged by scanning electrochemical microscopy, *Langmuir 21*, 692-698.
80. Ciobanu, M., Kincaid, H. A., Lo, V., Dukes, A. D., Jennings, G. K., and Cliffel, D. E. (2007) Electrochemistry and photoelectrochemistry of photosystem I adsorbed on hydroxyl-terminated monolayers, *Journal of Electroanalytical Chemistry 599*, 72-78.
81. Frolov, L., Rosenwaks, Y., Carmeli, C., and Carmeli, I. (2005) Fabrication of a photoelectronic device by direct chemical binding of the photosynthetic reaction center protein to metal surfaces, *Advanced Materials 17*, 2434-2437.
82. Frolov, L., Rosenwaks, Y., Richter, S., Carmeli, C., and Carmeli, I. (2008) Photoelectric junctions between GaAs and photosynthetic reaction center protein, *Journal of Physical Chemistry C 112*, 13426-13430.
83. Frolov, L., Rosenwaks, Y., Richter, S., Carmeli, C., and Carmeli, I. (2008) Photoelectric Junctions Between GaAs and Photosynthetic Reaction Center Protein, *J. Phys. Chem. C 112*, 13426-13430.
84. Frolov, L., Wilner, O., Carmeli, C., and Carmeli, I. (2008) Fabrication of oriented multilayers of photosystem I proteins on solid surfaces by auto-metallization, *Advanced Materials 20*, 263-266.

85. Govorov, A. O., and Carmeli, I. (2007) Hybrid Structures Composed of Photosynthetic System and Metal Nanoparticles: Plasmon Enhancement Effect, *Nano Lett 7*, 620-625.
86. Faulkner, C. J., Lees, S., Ciesielski, P. N., Cliffel, D. E., and Jennings, G. K. (2008) Rapid assembly of photosystem I monolayers on gold electrodes, *Langmuir 24*, 8409-8412.
87. Kaniber, S. M., Brandstetter, M., Simmel, F. C., Carmeli, I., and Holleitner, A. W. (2010) On-Chip Functionalization of Carbon Nanotubes with Photosystem I, *Journal of the American Chemical Society 132*, 2872-2873.
88. Kaniber, S. M., Simmel, F. C., Holleitner, A. W., and Carmeli, I. (2009) The optoelectronic properties of a photosystem I-carbon nanotube hybrid system, *Nanotechnology 20*, 345701.
89. Kim, I., Bender, S. L., Hranisavljevic, J., Utschig, L. M., Huang, L., Wiederrecht, G. P., and Tiede, D. M. (2011) Metal Nanoparticle Plasmon-Enhanced Light-Harvesting in a Photosystem I Thin Film, *Nano Lett*, in press.
90. Kincaid, H. A., Niedringhaus, T., Ciobanu, M., Cliffel, D. E., and Jennings, G. K. (2006) Entrapment of photosystem I within self-assembled films, *Langmuir 22*, 8114-8120.
91. Maly, J., Di Meo, C., De Francesco, M., Masci, A., Masojidek, J., Sugiura, M., Volpe, A., and Pilloton, R. (2004) Reversible immobilization of engineered molecules by Ni-NTA chelators, *Bioelectrochemistry 63*, 271-275.
92. Maly, J., Krejci, J., Ilie, M., Jakubka, L., Masojídek, J., Pilloton, R., Sameh, K., Steffan, P., Stryhal, Z., and Sugiura, M. (2005) Monolayers of photosystem II on gold electrodes with enhanced sensor response—effect of porosity and protein layer arrangement, *Analytical and Bioanalytical Chemistry 381*, 1558-1567.
93. Maly, J., Masci, A., Masojidek, J., Sugiura, M., and Pilloton, R. (2004) Monolayers of Natural and Recombinant Photosystem II on Gold Electrodes - Potentials for Use as Biosensors for Detection of Herbicides, *Analytical Letters 37*, 1645 - 1656.
94. Maly, J., Masojidek, J., Masci, A., Ilie, M., Cianci, E., Foglietti, V., Vastarella, W., and Pilloton, R. (2005) Direct mediatorless electron transport between the monolayer of photosystem II and poly(mercapto-p-benzoquinone) modified gold electrode--new design of biosensor for herbicide detection, *Biosensors and Bioelectronics 21*, 923-932.
95. Sugiura, M., and Inoue, Y. (1999) Highly Purified Thermo-Stable Oxygen-Evolving Photosystem II Core Complex from the Thermophilic Cyanobacterium Synechococcus elongatus Having His-Tagged CP43, *Plant Cell Physiol. 40*, 1219-1231.
96. Bhalla, V., Zhao, X., and Zazubovich, V. (2011) Detection of explosive compounds using Photosystem II-based biosensor, *Journal of Electroanalytical Chemistry 657*, 84-90.
97. Badura, A., Guschin, D., Esper, B., Kothe, T., Neugebauer, S., Schuhmann, W., and Rogner, M. (2008) Photo-induced electron transfer between photosystem 2 via cross-linked redox hydrogels, *Electroanalysis 20*, 1043-1047.
98. Badura, A., Guschin, D., Kothe, T., Kopczak, M. J., Schuhmann, W., and Rogner, M. (2011) Photocurrent generation by photosystem 1 integrated in crosslinked redox hydrogels, *Energy Environ. Sci. 4*, 2435-2440.
99. LaVan, D. A., and Cha, J. N. (2006) Approaches for biological and biomimetic energy conversion, *103*, 5251-5255.
100. Cardoso, M. B., Smolensky, D., Heller, W. T., Hong, K., and O'Neill, H. (2011) Supramolecular assembly of biohybrid photoconversion systems, *Energy Environ. Sci. 4*, 181-188.
101. Haehnel, W., and Hochheimer, H. J. (1979) On the current generated by a galvanic cell driven by photosynthetic electron transport, *Journal of Electroanalytical Chemistry 104*, 563-574.

102. Prince, R. C., and Kheshgi, H. S. (2005) The Photobiological Production of Hydrogen: Potential Efficiency and Effectiveness as a Renewable Fuel, *Critical Reviews in Microbiology 31*, 19-31.
103. Eda, G., and Chhowalla, M. (2009) Graphene-based Composite Thin Films for Electronics, *Nanoletters 9*, 814-818.
104. Eda, G., Lin, Y.-Y., Mattevi, C., Yamaguchi, H., Chen, H.-A., Chen, I.-S., Chen, C.-W., and Chhowalla, M. (2009) Blue Photoluminescence from Chemically Derived Graphene Oxide, *Advanced Materials 21*, 1-5.
105. Eda, G., Mattevi, C., Yamaguchi, H., Kim, H., and Chhowalla, M. (2009) Insulator to Semimetal Transition in Graphene Oxide, *Journal of Physical Chemistry C 113*, 15768–15771.
106. Novoselov, K. S., Geim, A. K., Morozov, S. V., Jiang, D., Zhang, Y., Dubonos, S. V., Crigorieva, I. V., and Firsov, A. A. (2004) Electric Field Effect in Atomically Thin Carbon Films, *Science 306*, 666-669.
107. Park, S., and Ruoff, R. S. (2009) Chemical methods for the production of graphenes *Nature Nanotechnology*, 217-224.
108. Stankovich, S., Dikin, D. A., Dommett, G. H. B., Kohlhaas, K. M., Zimney, E. J., Stach, E. A., Piner, R. D., Nguyen, S. T., and Ruoff, R. S. (2006) Graphene-based composite materials, *Nature 442*, 282-286.
109. Mkhoyan, K. A., Contryman, A. W., Silcox, J., Stewart, D. A., Eda, G., Mattevi, C., Miller, S., and Chhowalla, M. (2009) Atomic and Electronic Structure of Graphene-Oxide, *Nano Lett 9*, 1058-1063.
110. Eda, G., Lin, Y.-Y., Miller, S., Chen, C.-W., Su, W.-F., and Chhowalla, M. (2008) Transparent and conducting electrodes for organic electronics from reduced graphene oxide, *Applied Physics Letters 92*, 233305-233308.
111. Eda, G., Fanchini, G., and Chhowalla, M. (2008) Large-area ultrathin films of reduced graphene oxide as a transparent and flexible electronic material, *Nature Nanotechnology 3*, 270-274.
112. Kou, L., He, H., and Gao, C. (2010) Click chemistry approach to functionalize two-dimensional macromolecules of graphene oxide nanosheets, *2*, 177-183.
113. Kim, J., Cote, L. J., Kim, F., Yuan, W., Shull, K. R., and Huang, J. (2010) Graphene oxide sheets at interfaces, *Journal of American Chemical Society 132*, 8180-8186.
114. Du, D., Wang, L., Shao, Y., Wang, J., Engelhard, M. H., and Lin, Y. (2011) Functionalized Graphene Oxide as a Nanocarrier in a Multienzyme Labeling Amplification Strategy for Ultrasensitive Electrochemical Immunoassay of Phosphorylated p53 (S392), *Anal. Chem. 83*, 746-752.
115. Hu, W., Peng, C., Lv, M., Li, X., Zhang, Y., Chen, N., Fan, C., and Huang, Q. (2011) Protein Corona-Mediated Mitigation of Cytotoxicity of Graphene Oxide, *ACS Nano 5*, 3693-3700.
116. Jung, J. H., Cheon, D. S., Liu, F., Lee, K. B., and Seo, T. S. (2010) A Graphene Oxide Based Immuno-biosensor for Pathogen Detection, *Angew. Chem. 122*, 5844-5847.
117. Liu, J.-W., Zhang, Q., Chen, X.-W., and Wang, J.-H. (2011) Surface Assembly of Graphene Oxide Nanosheets on SiO_2 Particles for the Selective Isolation of Hemoglobin, *Chem. Eur. J. 17*, 4864-4870.
118. Liu, Z., Jiang, L., Galli, F., Nederlof, I., Olsthoorn, R. C. L., Lamers, G. E. M., Oosterkamp, T. H., and Abrahams, J. P. (2010) A graphene oxide·streptavidin complex for biorecognition - towards affinity purification, *Adv. Funct. Mater. 20*, 2857-2865.

119. Mao, S., Lu, G., Yu, K., Bo, Z., and Chen, J. (2010) Specific protein detection using thermally reduced graphene oxide sheet decorated with gold nanoparticle-antibody conjugates, *Adv. Mater. 22*, 3521-3526.
120. Mohanty, N., and Berry, V. (2008) Graphene-Based Single-Bacterium Resolution Biodevice and DNA Transistor: Interfacing Graphene Derivatives with Nanoscale and Microscale Biocomponents, *Nano Lett. 8*, 4469-4476.
121. Wang, Y., Li, Z., Hu, D., Lin, C.-T., Li, J., and Lin, Y. (2010) Aptamer/Graphene Oxide Nanocomplex for in Situ Molecular Probing in Living Cells, *J. Am. Chem. Soc. 132*, 9274-9276.
122. Xu, D., Zhou, N.-L., and Shen, J. (2010) Hemocompatibility of carboxylic graphene oxide, *Chemical Journal of Chinese Universities 31*, 2354-2359.
123. Shen, J., Shi, M., Yan, B., Ma, H., Li, N., Hu, Y., and Ye, M. (2010) Covalent attaching protein to graphene oxide via diimide-activated amidation, *Colloids Surf., B 81*, 434-438.
124. Zuo, X., He, S., Li, D., Peng, C., Huang, Q., Song, S., and Fan, C. (2010) Graphene Oxide-Facilitated Electron Transfer of Metalloproteins at Electrode Surfaces, *Langmuir 26*, 1936-1939.
125. Beal, D., and Joliot, A. P. (1987) Spectrophotometer with statistically balanced light for very high resolution, US 4696570 A, C.N.R.S.
126. Joliot, A. P., Beal, D., and Frilley, B. (1980) Une nouvelle methode spectrophotometrique destinee a l'etude des reactions photosythentiques, *Journal de Chemie Physique 3*, 77.
127. Jensen, P. E., Rosgaard, L., Knoetzel, J., and Scheller, H. V. (2002) Photosystem I activity is increased in the absence of the PSI-G subunit, *The Journal of biological chemistry 277*, 2798-2803.
128. Tjus, S. E., Møller, B. L., and Scheller, H. V. (1998) Photosystem I is an early target of photoinhibition in barley illuminated at chilling temperatures, *Plant physiology 116*, 755-764.
129. Joliot, P., and Joliot, A. (1984) Electron-transfer between the 2 photosysthems.1. Flash excitation under oxidizing conditions, *Biochimica Et Biophysica Acta 765*, 210-218.
130. Petroutsos, D., Terauchi, A. M., Busch, A., Hirschmann, I., Merchant, S. S., Finazzi, G., and Hippler, M. (2009) PGRL1 participates in iron-induced remodeling of the photosynthetic apparatus and in energy metabolism in Chlamydomonas reinhardtii, *The Journal of biological chemistry 284*, 32770-32781.
131. Witt, H. (1979) Energy conversion in the functional membrane of photosynthesis. Analysis by light pulse and electric pulse methods: The central role of the electric field, *Biochimica et Biophysica Acta (BBA)-Reviews on Bioenergetics 505*, 355-427.
132. Vittadello, M., Woronowicz, K., and Chhowalla, M. (2012) Chemically Modified Graphene, PCT/US2012/038626, CUNY and Rutgers University.
133. Grimme, R. A., Lubner, C. E., Bryant, D. A., and Golbeck, J. H. (2008) Photosystem I/Molecular Wire/Metal Nanoparticle Bioconjugates for the Photocatalytic Production of H2, *Journal of the American Chemical Society 130*, 6308-6309.
134. Blankenship, R. E. (2008) Photosynthetic Pigments: Structure and Spectroscopy, In *Molecular Mechanisms of Photosynthesis*, pp 42-60, Blackwell Science Ltd.
135. Karrasch, S., Bullough, P. A., and Ghosh, R. (1995) The 8.5 A projection map of the light-harvesting complex I from Rhodospirillum rubrum reveals a ring composed of 16 subunits, *The EMBO journal 14*, 631.
136. Parson, W., and Warshel, A. (2009) Mechanism of Charge Separation in Purple Bacterial Reaction Centers, In *The Purple Phototrophic Bacteria* (Hunter, C. N., Daldal, F., Thurnauer, M., and Beatty, J. T., Eds.), pp 355-377, Springer Netherlands.

137. Fotiadis, D., Qian, P., Philippsen, A., Bullough, P. A., Engel, A., and Hunter, C. N. (2004) Structural Analysis of the Reaction Center Light-harvesting Complex I Photosynthetic Core Complex of Rhodospirillum rubrum Using Atomic Force Microscopy, *J. Biol. Chem. 279*, 2063-2068.
138. Janzen, A. F., and Seibert, M. (1980) Photoelectrochemical conversion using reaction-centre electrodes, *Nature 286*, 584-585.
139. Katz, E. (1994) Application of bifunctional reagents for immobilization of proteins on a carbon electrode surface: Oriented immobilization of photosynthetic reaction centers, *Journal of Electroanalytical Chemistry 365*, 157-164.
140. Katz, E. Y., Shkuropatov, A. Y., Vagabova, O. I., and Shuvalov, V. A. (1989) Coupling of photoinduced charge separation in reaction centers of photosynthetic bacteria with electron transfer to a chemically modified electrode, *Biochimica et Biophysica Acta (BBA)-Bioenergetics 976*, 121-128.
141. Lu, Y., Xu, J., Liu, B., and Kong, J. (2007) Photosynthetic reaction center functionalized nano-composite films: Effective strategies for probing and exploiting the photo-induced electron transfer of photosensitive membrane protein, *Biosensors and Bioelectronics 22*, 1173-1185.
142. Lebedev, N., Trammell, S. A., Spano, A., Lukashev, E., Griva, I., and Schnur, J. (2006) Conductive Wiring of Immobilized Photosynthetic Reaction Center to Electrode by Cytochrome c, *Journal of the American Chemical Society 128*, 12044-12045.
143. Lebedev, N., Trammell, S. A., Tsoi, S., Spano, A., Kim, J. H., Xu, J., Twigg, M. E., and Schnur, J. M. (2008) Increasing efficiency of photoelectronic conversion by encapsulation of photosynthetic reaction center proteins in arrayed carbon nanotube electrode, *Langmuir 24*, 8871-8876.
144. Dorogi, M., Bálint, Z., Mikó, C., Vileno, B., Milas, M., Hernádi, K., Forró, L., Váró, G., and Nagy, L. (2006) Stabilization Effect of Single-Walled Carbon Nanotubes on the Functioning of Photosynthetic Reaction Centers, *The Journal of Physical Chemistry B 110*, 21473-21479.
145. Oda, I., Iwaki, M., Fujita, D., Tsutsui, Y., Ishizaka, S., Dewa, M., Nango, M., Kajino, T., Fukushima, Y., and Itoh, S. (2010) Photosynthetic Electron Transfer from Reaction Center Pigment− Protein Complex in Silica Nanopores, *Langmuir 26*, 13399-13406.
146. Kondo, M., Nakamura, Y., Fujii, K., Nagata, M., Suemori, Y., Dewa, T., Iida, K., Gardiner, A. T., Cogdell, R. J., and Nango, M. (2007) Self-Assembled Monolayer of Light-Harvesting Core Complexes from Photosynthetic Bacteria on a Gold Electrode Modified with Alkanethiols, *Biomacromolecules 8*, 2457-2463.
147. Suemori, Y., Nagata, M., Nakamura, Y., Nakagawa, K., Okuda, A., Inagaki, J.-i., Shinohara, K., Ogawa, M., Iida, K., and Dewa, T. (2006) Self-assembled monolayer of light-harvesting core complexes of photosynthetic bacteria on an amino-terminated ITO electrode, *Photosynthesis research 90*, 17-21.
148. Kondo, M., Iida, K., Dewa, T., Tanaka, H., Ogawa, T., Nagashima, S., Nagashima, K. V., Shimada, K., Hashimoto, H., and Gardiner, A. T. (2012) Photocurrent and electronic activities of oriented-his-tagged photosynthetic light-harvesting/reaction center core complexes assembled onto a gold electrode, *Biomacromolecules 13*, 432-438.
149. Magis, G. J., Olsen, J. D., Reynolds, N. P., Leggett, G. J., Hunter, C. N., Aartsma, T. J., and Frese, R. N. (2011) Use of engineered unique cysteine residues to facilitate oriented coupling of proteins directly to a gold substrate, *Photochemistry and photobiology 87*, 1050-1057.

150. den Hollander, M.-J., Magis, J. G., Fuchsenberger, P., Aartsma, T. J., Jones, M. R., and Frese, R. N. (2011) Enhanced photocurrent generation by photosynthetic bacterial reaction centers through molecular relays, light-harvesting complexes, and direct protein–gold interactions, *Langmuir 27*, 10282-10294.
151. Koblízek, M., Shih, J. D., Breitbart, S. I., Ratcliffe, E. C., Kolber, Z. S., Hunter, C. N., and Niederman, R. A. (2005) Sequential assembly of photosynthetic units in *Rhodobacter sphaeroides* as revealed by fast repetition rate analysis of variable bacteriochlorophyll *a* fluorescence, *Biochimica et Biophysica Acta (BBA)-Bioenergetics 1706*, 220-231.
152. Woronowicz, K., Sha, D., Frese, R. N., Sturgis, J. N., Nanda, V., and Niederman, R. A. (2011) The effects of protein crowding in bacterial photosynthetic membranes on the flow of quinone redox species between the photochemical reaction center and the ubiquinol-cytochrome c2 oxidoreductase, *Metallomics 3*, 765-774.
153. Cohen-Bazire, G., Sistrom, W., and Stanier, R. (1957) Kinetic studies of pigment synthesis by non-sulfur purple bacteria, *Journal of Cellular and Comparative Physiology 49*, 25-68.
154. AAGAARD, J., and Sistrom, W. (1972) Control of synthesis of reaction center bacteriochlorophyll in photosynthetic bacteria, *Photochemistry and photobiology 15*, 209-225.
155. Inamine, G., and Niederman, R. (1982) Development and growth of photosynthetic membranes of Rhodospirillum rubrum, *Journal of bacteriology 150*, 1145-1153.
156. Ormerod, J. G., Ormerod, K. S., and Gest, H. (1961) Light-dependent utilization of organic compounds and photoproduction of molecular hydrogen by photosynthetic bacteria; relationships with nitrogen metabolism, *Archives of biochemistry and biophysics 94*, 449-463.
157. Woronowicz, K., Sha, D., Frese, R. N., and Niederman, R. A. (2011) The accumulation of the light-harvesting 2 complex during remodeling of the Rhodobacter sphaeroides intracytoplasmic membrane results in a slowing of the electron transfer turnover rate of photochemical reaction centers, *Biochemistry 50*, 4819-4829.
158. Westerhuis, W. H., Sturgis, J. N., Ratcliffe, E. C., Hunter, C. N., and Niederman, R. A. (2002) Isolation, size estimates, and spectral heterogeneity of an oligomeric series of light-harvesting 1 complexes from Rhodobacter sphaeroides, *Biochemistry 41*, 8698-8707.
159. Bahatyrova, S., Frese, R. N., Siebert, C. A., Olsen, J. D., van der Werf, K. O., van Grondelle, R., Niederman, R. A., Bullough, P. A., Otto, C., and Hunter, C. N. (2004) The native architecture of a photosynthetic membrane, *Nature 430*, 1058-1062.
160. Jamieson, S. J., Wang, P., Qian, P., Kirkland, J. Y., Conroy, M. J., Hunter, C. N., and Bullough, P. A. (2002) Projection structure of the photosynthetic reaction centre–antenna complex of Rhodospirillum rubrum at 8.5 Å resolution, *The EMBO journal 21*, 3927-3935.
161. Vittadello , M., Gorbunov, M. Y., Mastrogiovanni, D. T., Wielunski, L. S., Garfunkel , E. L., Guerrero, F., Kirilovsky, D., Sugiura, M., Rutherford, A. W., Safari, A., and Falkowski , P. G. (2010) Photoelectron Generation by Photosystem II Core Complexes Tethered to Gold Surfaces, *ChemSusChem 3*, 471-475.
162. Lewis, N. S., and Nocera, D. G. (2006) Powering the planet: Chemical challenges in solar energy utilization, *Proceedings of the National Academy of Sciences 103*, 15729-15735.
163. Woronowicz, K., and Niederman, R. A. (2010) Proteomic Analysis of the Developing Intracytoplasmic Membrane in <i>Rhodobacter sphaeroides</i> During Adaptation to Low Light Intensity, In *Recent Advances in Phototrophic Prokaryotes* (Hallenbeck, P. C. C., Ed.), pp 161-178, Springer New York.

164. French, C., and Milner, H. (1955) Disintegration of bacteria and small particles by high-pressure extrusion, *Methods in enzymology 1*, 64-67.
165. Gaberc-Porekar, V., and Menart, V. (2001) Perspectives of immobilized-metal affinity chromatography, *Journal of biochemical and biophysical methods 49*, 335-360.
166. Arnold, F. H. (1991) Metal-affinity separations: a new dimension in protein processing, *Nature biotechnology 9*, 151-156.
167. Sulkowski, E. (1989) The saga of IMAC and MIT, *Bioessays 10*, 170-175.
168. Hochuli, E., Bannwarth, W., Döbeli, H., Gentz, R., and Stüber, D. (1988) Genetic approach to facilitate purification of recombinant proteins with a novel metal chelate adsorbent, *Nature Biotechnology 6*, 1321-1325.
169. Hochuli, E., Döbeli, H., and Schacher, A. (1987) New metal chelate adsorbent selective for proteins and peptides containing neighbouring histidine residues, *Journal of Chromatography A 411*, 177-184.
170. Sulkowski, E. (1996) Immobilized metal-ion affinity chromatography: Imidazole proton pump and chromatographic sequelae. I. Proton pump, *Journal of Molecular Recognition 9*, 389-393.
171. Seidler, A. (1994) Introduction of a histidine tail at the N-terminus of a secretory protein expressed in Escherichia coli, *Protein engineering 7*, 1277-1280.
172. Takacs, B. J., and Girard, M.-F. (1991) Preparation of clinical grade proteins produced by recombinant DNA technologies, *Journal of immunological methods 143*, 231-240.
173. Novaković, S., Menart, V., Gaberc-Porekar, V., Štalc, A., Serša, G., Čemažar, M., and Jezeršek, B. (1997) NEW TNF-A ANALOGUES: A POWERFUL BUT LESS TOXIC BIOLOGICAL TOOL AGAINST TUMOURS, *Cytokine 9*, 597-604.
174. Casey, J., Keep, P., Chester, K. A., Robson, L., Hawkins, R., and Begent, R. (1995) Purification of bacterially expressed single chain Fv antibodies for clinical applications using metal chelate chromatography, *Journal of immunological methods 179*, 105-116.
175. Kaslow, D. C., and Shiloach, J. (1994) Production, purification and immunogenicity of a malaria transmission-blocking vaccine candidate: TBV25H expressed in yeast and purified using nickel-NTA agarose, *Nature Biotechnology 12*, 494-499.
176. Johnson, D. L., and Martin, L. L. (2005) Controlling Protein Orientation at Interfaces Using Histidine Tags: An Alternative to Ni/NTA, *Journal of the American Chemical Society 127*, 2018-2019.
177. Herzenberg, L. A., Parks, D., Sahaf, B., Perez, O., Roederer, M., and Herzenberg, L. A. (2002) The history and future of the fluorescence activated cell sorter and flow cytometry: a view from Stanford, *Clinical chemistry 48*, 1819-1827.
178. Herzenberg, L. A., Sweet, R. G., and Herzenberg, L. A. (1976) Fluorescence-activated cell sorting, *Sci Am 234*, 108-117.
179. Rayleigh, L. (1879) On the capillary phenomena of jets, *Proceedings of the Royal Society of London 29*, 71-97.
180. Savart, F. (1833) Mémoire sur la Constitution des Veines Liquides lancées par des orifices circularires en mince paroi [Memory on the Constitution Vein Liquids launched by circularires holes in thin wall], *Annales de chimie et de physique. 53*, 337-386.
181. Bagué Anne, Stéphane, Z., and Christophe, J. (2007) Droplet formation at the edge of a liquid sheet, In *6 International Conference on Multiphase Flow*, Leipzig, Germany.
182. Zumdahl, S., and Zhmdahl, S. (2007) *Chemistry*, 7th ed., Houghton Mifflin Company.
183. Schlodder, E. (2009) Introduction to optical methods in photosynthesis, *Photosynthesis research 101*, 93-104.

184. Amand, L., and Tullin, C. (1999) The Theory Behind FTIR analysis–Application Examples From Measurement at the 12 MW Circulating Fluidized Bed Boiler at Chalmers, *CECOST, Lund University, Sweden*.
185. Kong, J., and Yu, S. (2007) Fourier transform infrared spectroscopic analysis of protein secondary structures, *Acta Biochimica et Biophysica Sinica 39*, 549-559.
186. Banwell, C., and McCash, E. M. Fundamentals of molecular spectroscopy, 1994, McGraw Hill, England, ISBN 0-07-707976-0.
187. Jaggi, N., and Vij, D. (2006) Fourier transform infrared spectroscopy, In *Handbook of Applied Solid State Spectroscopy*, pp 411-450, Springer.
188. Beal, D., and Joliot, A. P. (1987) Spectrophotometer with statistically balanced light for very high resolution, Google Patents.
189. Manole, A., Neacsu, I., Apostu, M., and Melnig, V. (2006) Membrane covered polarographic oxygen sensor manufacturing. Theoretical considerations, Analele Stiinţifice ale Universităţii "Al. I. Cuza" Iasi, Tomul II, s. Biofizică, Fizică medicală şi Fizica mediului.
190. Evans, D. H., O'Connell, K. M., Petersen, R. A., and Kelly, M. J. (1983) Cyclic voltammetry, *Journal of Chemical Education 60*, 290.
191. Clark Jr, L. (1956) Monitor and control of blood and tissue oxygen tensions, *ASAIO Journal 2*, 41-48.
192. Sauerbrey, G. (1959) Verwendung von Schwingquarzen zur Wägung dünner Schichten und zur Mikrowägung, *Zeitschrift für Physik 155*, 206-222.
193. Einstein, A. (1905) Über einen die Erzeugung und Verwandlung des Lichtes betreffenden heuristischen Gesichtspunkt, *Annalen der Physik 322*, 132-148.
194. Pais, A. (1979) Einstein and the quantum theory, *Reviews of Modern Physics 51*, 863.
195. Brundle, C., Baker, A., and Thomas, T. D. (2008) Electron Spectroscopy: Theory, Techniques, and Applications, Volume 2, *Physics Today 32*, 62-66.
196. Sulkowski, E. (1996) Immobilized metal-ion affinity chromatography: Imidazole proton pump and chromatographic sequelae. II. Chromatographic sequelae, *Journal of Molecular Recognition 9*, 494-498.
197. Eda, G., Lin, Y. Y., Mattevi, C., Yamaguchi, H., Chen, H. A., Chen, I., Chen, C. W., and Chhowalla, M. (2010) Blue photoluminescence from chemically derived graphene oxide, *Advanced Materials 22*, 505-509.
198. Park, S., and Ruoff, R. S. (2009) Chemical methods for the production of graphenes, *Nature nanotechnology 4*, 217-224.
199. Dong, X., Ning-Lin, Z., and Jian, S. (2010) Hemocompatibility of carboxylic graphene oxide, *Chemical Journal Of Chinese Universities-Chinese 31*, 2354-2359.
200. Du, D., Wang, L., Shao, Y., Wang, J., Engelhard, M. H., and Lin, Y. (2011) Functionalized graphene oxide as a nanocarrier in a multienzyme labeling amplification strategy for ultrasensitive electrochemical immunoassay of phosphorylated p53 (S392), *Analytical chemistry 83*, 746-752.
201. Hu, W., Peng, C., Lv, M., Li, X., Zhang, Y., Chen, N., Fan, C., and Huang, Q. (2011) Protein corona-mediated mitigation of cytotoxicity of graphene oxide, *Acs Nano 5*, 3693-3700.
202. Jung, J. H., Cheon, D. S., Liu, F., Lee, K. B., and Seo, T. S. (2010) A Graphene Oxide Based Immuno-biosensor for Pathogen Detection, *Angewandte Chemie International Edition 49*, 5708-5711.
203. Kim, J., Cote, L. J., Kim, F., Yuan, W., Shull, K. R., and Huang, J. (2010) Graphene oxide sheets at interfaces, *Journal of the American Chemical Society 132*, 8180-8186.

204. Liu, J. W., Zhang, Q., Chen, X. W., and Wang, J. H. (2011) Surface assembly of graphene oxide nanosheets on SiO2 particles for the selective isolation of hemoglobin, *Chemistry-A European Journal 17*, 4864-4870.
205. Liu, Z., Jiang, L., Galli, F., Nederlof, I., Olsthoorn, R. C., Lamers, G. E., Oosterkamp, T., and Abrahams, J. P. (2010) A graphene oxide streptavidin complex for biorecognition–towards affinity purification, *Advanced Functional Materials 20*, 2857-2865.
206. Mao, S., Lu, G., Yu, K., Bo, Z., and Chen, J. (2010) Specific Protein Detection Using Thermally Reduced Graphene Oxide Sheet Decorated with Gold Nanoparticle-Antibody Conjugates, *Advanced materials 22*, 3521-3526.
207. Mohanty, N., and Berry, V. (2008) Graphene-based single-bacterium resolution biodevice and DNA transistor: interfacing graphene derivatives with nanoscale and microscale biocomponents, *Nano Lett 8*, 4469-4476.
208. Wang, Y., Li, Z., Hu, D., Lin, C.-T., Li, J., and Lin, Y. (2010) Aptamer/graphene oxide nanocomplex for in situ molecular probing in living cells, *Journal of the American Chemical Society 132*, 9274-9276.
209. Wang, K., Ruan, J., Song, H., Zhang, J., Wo, Y., Guo, S., and Cui, D. (2011) Biocompatibility of graphene oxide, *Nanoscale Res Lett 6*.
210. Müh, F., and Zouni, A. (2005) Extinction coefficients and critical solubilisation concentrations of photosystems I and II from Thermosynechococcus elongatus, *Biochimica et Biophysica Acta (BBA) - Bioenergetics 1708*, 219-228.